Sensorless position estimation of PMSMs using state observation and a novel iterative algorithm

Dissertation
zur Erlangung des Grades
des Doktors der Ingenieurwissenschaften
der Naturwissenschaftlich-Technischen Fakultät
der Universität des Saarlandes

von
Stefano Fabbri

Saarbrücken
2022

Tag des Kolloquiums:	10. März 2023
Dekan:	Prof. Dr. Ludger Santen
Berichterstatter:	Prof. Dr.-Ing. Matthias Nienhaus
	Jun.-Prof. Dr. Gianluca Rizzello
Akad. Mitglied:	Dr. Michael Roland
Vorsitz:	Prof. Dr.-Ing. Michael Vielhaber

Acknowledgement

I am extremely grateful to my professor Matthias Nienhaus for the opportunity he gave to me to work at his chair during the past years. His support and guidance helped me on many occasions and allowed me to make considerable progress in my working life.

I would also like to extend my deepest gratitude to my mentor Emanuele Grasso for his unwavering support and patience that cannot be underestimated. He provided constructive criticism and helpful advice for writing this work as well as all my other publications. I owe him a lot.

I cannot begin to express my thanks to my colleague and friend Niklas König, who was always ready to give clever recommendations and stood by me during tough times.

I'm deeply indebted to Riccardo Mandriota for the time we spent together in the office and during the weekends. The recreational time passed together was fundamental against the periods of stress.

I would like to extend my sincere thanks to the rest of my colleagues, starting from Klaus Schuhmacher, who shared his knowledge and competencies with me. I would also like to extend my gratitude to Chris May for his support and cooperation during the Praktikum class and our exciting discussion about the U.S.A. and living abroad. Special thanks to Stephan Kleen and Robert Schwartz for our interesting german conversations and for their patience. I also wish to thank Elke Zarbock for the harmony she brought every day to the chair and for the fantastic job she did. Many thanks also to my ex-colleagues Daniel Merl and Martin Becker.

Eventually, I would like to thank the entire team at L.A.T. for providing most of the material, software, and instruments that I could use to complete my doctoral work. Many thanks also to the students that gravitated around the chair during the past years for the help and support provided: Dario, Marcello, Giorgia, Julian, Niccolò, Davide and Sabino.

Completing my studies would not have been possible without the support and nurturing of my girlfriend Luise and her family. They provided me with encouragement throughout the duration of this project and happily continue to do so. A special thanks also to every member of my family in Italy for their moral support and the vicinity they provided me although the physical distance.

I cannot forget to mention all my friends in Germany and my old friends in Italy. Firstly, many thanks to my circle of friends *ANDER DE PALAS*. Thanks should also go to the scout group *A.G.E.S.C.I.* of Vaiano and to my university mates Edoardo and Leonardo. I also wish to thank the people of the *Missione Cattolica Italiana*, especially Alessandro and Elisabetta, for our splendid walks together, as well as my flatmates Saskia and Francesco. I will not forget the friends that I've encountered in Saarbrücken, especially I would like to thank Patrizio, Libero, Marius, Anika, Simone and Luisa. At last, very special thanks to Professor Luca Pugi of the University of Florence, who opened the way for my studies abroad.

"The triangle tingles and the trumpet plays slow, Farewell..." (F. Guccini).

Clarification about personal contribution of the doctoral dissertation of Stefano Fabbri

The work presented in the dissertation written by Stefano Fabbri and entitled “Sensorless Position Estimation of PMSMs using State Observation and a Novel Iterative Algorithm” is the result of a scientific activity conducted at the LAT department of the Saarland University in the period from July 1st 2018 until June 30th 2021.
During this time, one of the main research focuses of the LAT department lied in the analysis and development of the sensorless technique referred to as “Direct Flux Control (DFC)” for application to Permanent Magnet Synchronous Machines, that was firstly proposed under this label by Dr. R. Strothmann in [34]. This technique has been mathematically described and investigated in different ways from different scientists. Mr. Fabbri has based his scientific activity on the mathematical formulation of the DFC technique proposed by Dr-Ing. E. Grasso and published through his research papers and habilitation thesis entitled “Direct Flux Control – A sensorless technique for star-connected synchronous machines. An analytic approach”.
The significant and personal contribution of Mr. Fabbri focuses on the improvement of the sensorless driving algorithm that can be developed based on the DFC measurements. In particular, two main results have been achieved. The first is the introduction of the so-called “Iterative Vector Decoupling (IVD)” technique, that allows the reduction of the remaining harmonics on the reconstructed DFC position angle, a well-known problem of machine anisotropy-based sensorless techniques. The second result, instead, regards the possibility of combining the IVD technique to state observers to further improve the performance of the DFC technique at middle and high speed ranges.
With the intent of providing a comprehensive and understandable text, the doctoral dissertation of Mr. Fabbri presents, in Chapter 2, a recall of the DFC technique that is the result of the scientific activity of Dr.-Ing. E. Grasso. With his permission, some figures and part of the text has been ported to the thesis of Mr. Fabbri. The presentation is, nevertheless, not as thorough as the one presented by Dr.-Ing. Grasso since the scope is to provide to the reader the fundamental concepts for the understanding of the further Chapters. Similarly, Dr. E. Grasso has presented the IVD technique within his habilitation thesis in Chapter 3 without providing mathematical aspects, such as the parameter sensitivity analysis, that are, instead, further investigated and discussed in the work of Mr. Fabbri. This also applies in particular to the pictures, which are mostly taken from cited joint publications from Mr. S. Fabbri and Dr. E. Grasso [54].
This has also resulted due to the strict scientific collaboration between Dr.-Ing. E. Grasso and Mr. Fabbri during their work at the LAT department and the continuous exchanges that allowed the scientific advancement and development of the DFC sensorless technique. This joint activity results also in a discrete number of co-authored scientific publications on the matter.

List of Abbreviations

DFC	Direct Flux Control
IVD	Iterative Vector Decoupling
FOC	Field Oriented Control
AVO	Absolute Value Optimum
SO	Symmetric Optimum
PMSM	Permanent Magnet Synchronous Motor
PWM	Pulse Width Modulation
SVM	Space Vector Modulation
EKF	Extended Kalman Filter
PLL	Phase Locked Loop
PI	Proportional Integrative
EMF	Electro-Motive Force

Abstract

In the field of synchronous machines, Permanent Magnet Synchronous Machines, PMSMs, are broadly used for many applications thanks to their higher power density and simpler construction. For those motors, the knowledge of the rotor angular position is an important information that is used in order to perform the control strategy. Moreover, the request of miniaturized and higher power density solutions at relative low prices supports the concept of self-sensing systems, in which no sensors are employed for the measurement of the angular position. In particular, for those motors with an accessible star-point, the so-called Direct Flux Control (DFC) sensorless technique represents a valid choice thanks to its compact hardware implementation and high Signal-to-Noise ratio. Nevertheless, the provided estimated position is affected by systematic errors related to the machine phase inductances. This work exactly addresses this issue. A static iterative algorithm is proposed in order to reduce the systematic error of the DFC technique. This algorithm, called Iterative Vector Decoupling (IVD), is based on the execution in real-time of an iteration sequence that converges to the real position. Moreover, a state observation method, namely a Kalman filter, is combined with the IVD algorithm in order to compensate the effect of potential disturbances and, at the same time, to provide the estimation of the external load torque applied at the motor shaft. This novel approach, after proper implementation and adjustments, leads to a reasonable improvement compared to the form state of the technique.

Kurzzusammenfassung

Permanentmagneterregte Synchronmaschinen (PMSM) sind im Bereich der synchronen Maschinen dank ihrer hohen Leistungsdichte und ihrer einfachen Konstruktion in vielen Anwendungen weit verbreitet. Dabei ist die Kenntnis der Rotorlage eine wichtige Voraussetzung, um Regelungsstrategien an dieser Art von Motoren umzusetzen. Insbesondere die Nachfrage nach miniaturisierten und leistungsstarken Antriebslösungen bei gleichzeitig niedrigen Kosten führt zur Konzeptionierung geberloser Systeme, die meist auch als sensorlose oder selbstmessende Systeme bezeichnet werden. Solche Systeme erfordern keine weiteren mechanischen Sensoren zur Rotorlageerfassung. Besonders für Motoren mit zugänglichem Sternpunkt erlaubt die als Direct Flux Control (DFC) bekannte Technik eine geeignete Realisierung einer geberlosen Regelung dank ihrer kompakten Hardwareimplementierung und ihrem hohen Signal-Rausch-Verhältnis. Dennoch wird die geschätzte Winkelposition von einem systematischen Fehler, hervorgerufen durch die Phaseninduktivität der Maschine, beeinflusst. Um dieses Problem zu adressieren, schlägt die vorliegende Arbeit ein statisch iteratives Verfahren vor. Der entworfene Algorithmus namens Iterative Vector Decoupling (IVD) erfordert die Kenntnis eines in Theorieteil dieser Arbeit bestimmten Parameters und basiert auf der Ausführung einer iterativen Abfolge, um zu der gewünschten Rotorlage zu konvergieren. Im Anschluss wird ein Kalman Filter als Beobachter in Zusammenhang mit dem IVD-Algorithmus eingesetzt, um potenzielle Störgrößen zu kompensieren und gleichzeitig das an der Motorwelle anliegende Lastmoment zu schätzen. Es wird gezeigt, dass diese nueartige Ansatz bei korrekten Implementierung und Ausgleich zu einer significant Verbesserung im Vergleich zum vorherigen Stand der Technik fuhrt.

Contents

1 Introduction

Nowadays, electrical machines are considered the most common solution for the drive and control of dynamical systems within several application areas, including: industry, automotive, public and domestic life, transportation, medical and healthcare equipment, power generation, ecc. [1]. The reason of the increasing popularity of electrical machines can be addressed to two main factors: the portability of the electric power and the new advancement on material technology. Plainly, the example that well explains this trend is the e-mobility revolution. Governments are pushing forward for more ecological and sustainable transportation methods, such as electrical bikes, scooters, cars and public transports in order to potentially increase the life quality of the citizens and decrease the carbon dioxide emission.

Indeed, the start of the technological evolution process that brought the electrical machines to be today so popular can be located at the beginning of the 17th century, i.e. during the first industrial revolution, when various scientists in Europe and United States investigated the relation between magnetic and electrical fields [2]. In 1828, the Hungarian physicist Ányos Jedlik invented the first commutator and realized the first DC motor prototype, introducing also the concept of stator and rotor as main machine components. Within the following years numerous improvements had been made and the DC machines started to be applied for a wider range of applications, also thanks to the discovery of the reversibility of the electric machine in 1867 which stated that the DC motor could be used as generator [3]. Despite its increasing popularity, at the end of the 18th century the DC motors started to be substituted for some applications by induction machines, firstly invented by the Italian physicist Galileo Ferraris and then enhanced by Nikola Tesla between 1887 and 1891. The main reasons of their success were the commutatorless technology that avoided the high maintenance due to the constant service and replace of the mechanical brushes and the increasing interest given to AC machines for the production and distribution of electricity thanks to the invention of the transformer [4]. Nevertheless, the induction machines never replaced completely the DC motors for various reasons, among them the notorious low starting torque, the difficulty of the speed control and the power factor drop at low loads resulting in higher copper losses. Thus, for many applications, the issues related to the commutator remained for long time unresolved. After almost a century from the Ferraris-Tesla invention, the availability of more efficient magnetic materials combined with the forward steps made in the field of electronic power devices allowed the development of the Permanent Magnet Synchronous Motor (PMSM) concept, whereas synchronous machines as generator were at the time already employed for the production of electricity. Permanent magnets are applied to the rotor instead of electromagnets and the commutation of the stator windings excitation for the generation of the external magnetic field is performed by an external power electronic device, generally an inverter. PMSMs combine the advantage of DC motors, such as efficiency and miniaturization, to the advantages of the commutatorless induction motor. Thus, the absence of the commutator and the continuous advancements in electronics miniaturization and integration for more efficient embedded driving solutions allow the PMSMs to

be considered as a valid choice for those applications that require lightweight, space-saving and mechanically robust solutions as well as longer lifetime and less noise generation. Additionally, avoiding mechanical brushes enables higher peak currents with a positive impact on the dynamic response and power density. The PMSMs are usually divided into bruschless DC (BLDC) and bruschless AC (BLAC) depending on the winding distribution of the stator coils and the driving strategies. The BLDC, as the name suggests, is similar to the DC motor concept since the commutation of its stator windings is performed by means of a block excitation strategy that simulates the classical mechanical commutation of the brushed motor. Instead, the BLAC provides a sinusoidal external magnetic flux by a sinusoidal commutation of the stator windings. In particular, driving BLAC motors require sensing the rotor position with good accuracy for proper operation [5]. Thus, position sensors are typically installed for operating a PMSM, such as resolvers or encoders, which lead to an increase in cost, space requirements and system complexity, especially in case of small sized drives.

1.1 State of the art

Certainly, the need of overcoming those issues pushed the research to focus on new position estimation solutions in order to substitute the mechatronic sensors. It is normal practice to refer to these solutions with the term ”sensorless techniques”. Within the last few decades, several scientific contributions concerning new sensorless techniques or improvements to the already existing ones were proposed. A list of the principal techniques is given in Table 1.1. As shown, the proposed techniques are normally sorted depending on the technology used and the exploited physical quantities. A first clear separation can be made between model and anisotropy based techniques. The model based techniques make use of observers like Luenberger, Kalman Filter, Sliding Mode, etc. for the estimation of the angular speed and position of the machine. There are two main possible implementations of the observers. The first approach uses them for the estimation of the Back-EMF or the magnetic flux generated by the permanent magnets. The obtained estimated values are then fed into an additional system, typically a PLL filter, for the tracking of the angular speed and position. Alternatively, a unique observer provided with both electrical and mechanical dynamical equations of the machine can be implemented. The possibilities given by the combination of different observers with different tracking strategies make the model based sensorless approach to have practically infinite solutions. A thorough review of those techniques have been presented in [6] and [7].

The main drawback of the model based sensorless techniques is their inadequacy to estimate the position at standstill and at small speed range operation. In fact, a noticeable movement of the rotor, i.e. its angular speed, is needed in order to generate appreciable effects on the electrical quantities due to the Back-EMF. In order to allow the position estimation at standstill operation, the anisotropy based sensorless techniques can be employed. These methods are based on the exploitation of the modulated values of the machine phase inductances through the varying angular position of the permanent magnets. It has been proven that this modulation effect is directly dependent on the machine anisotropy characteristic. Since this work introduces an algorithm for the improvement of an anisotropy based technique, a detailed history of the major contributions within this field of research will be provided.

<table>
<tr><th colspan="3">Sensorless Techniques</th></tr>
<tr><th colspan="2">Anisotropy Based</th><th>Model Based</th></tr>
<tr><td rowspan="2">Fundamental
PWM Excitation
Based (FPE Based)</td><td colspan="2">Injection Based</td><td rowspan="2">BEMF/Flux
and/or
Position/Speed
Estimation Based</td></tr>
<tr><td>Pulsating
Signal
Injection</td><td>Rotating
Signal
Injection</td></tr>
<tr><td>INFORM</td><td>Sinusoidal
Injection</td><td>Negative
Sequence
Current</td><td>Luenberger Observer</td></tr>
<tr><td>Zero Voltage
Vector Injection (ZVVI)</td><td>Square-wave</td><td>Zero
Sequence
Voltage</td><td>Kalman Filter (EKF)</td></tr>
<tr><td>Zero Sequence
Current Derivative (ZSCD)</td><td rowspan="4"></td><td rowspan="4"></td><td>Sliding Mode Observer</td></tr>
<tr><td>Arbitrary Injection</td><td>Phase Locked Loop (PLL)</td></tr>
<tr><td>Induced Voltage
caused by
Magnetic Saturation
(IVMS)</td><td>Model Reference
Adaptive System
(MRAS)</td></tr>
<tr><td>Direct Flux
Control (DFC)</td><td>I&I Observer</td></tr>
</table>

Table 1.1: List of the principal sensorless techniques for PMSMs. The methods (highlighted in yellow) are sorted vertically depending on their technology.

1.1.1 Machine anisotropy based sensorless techniques

The first approach to estimate the rotor position by exploiting the presence of machine anisotropies was proposed by Schrödel in 1988 [8] and 1992 [9]. He named this technique INFORM (INdirect Flux-detection by Online Reactance Measurement) and it was firstly adopted for the angular position estimation of induction motors. The INFORM is based on the application of test pulses generated by a modified PWM (Pulse Width Modulation) driving signal that, through the measurement of current derivatives, allows the online estimation of the machine reactances and consequently the rotor angular position. INFORM technique has been then improved and extended over the years also to PMSMs [10–12]. Right after the work of Schrödel, a scientific contribution about the sensorless position estimation by means of a high-frequency excitation of the machine was published by Lorentz and Jansen [13]. The authors showed that the phase current vector response due to the injection of an high-frequency rotational carrier takes the form of a rotating vector whose phase

is related to the rotor position. The current signals are first demodulated and then fed to an observer for the extraction of the position. The use of an observer let this technique to be dependent on machine parameters. In [14], the same authors proved that the phase inductance variations are not only dependent on the machine anisotropy but also on the soft magnetic stator material. A modification of this technique was proposed by Corley [15]. Instead of the injection of a rotational carrier within the stator frame, a pulsating signal along the q-axis of the estimated reference frame was applied. This method has the direct advantage to require less computational effort than the rotational injection. Moreover, it proved to provide more robustness and precision in terms of position estimation result. However, the pulsating method also required an observer dependent on the machine parameters. Due to the promising results, many contributions focused on the improvement of this technique. Among them the works [16, 17], where the authors introduced a modification to the injection methodology. The high-frequency signal is injected along the d-axis allowing the elimination of the observer and at the same time the reduction of the torque ripple (typical of rotating carrier injection).

Within the following years, numerous contributions followed aiming at improving the sensorless injection based technique. Remarkable is the work presented by Nussbaumer [18] where the oversampling of the current first derivative was proposed in order to retrieve information about the machine phase inductances. In [19], an alternating high-frequency injection method was applied were, instead of performing one measurement per period, 100 samples per PWM period where acquired and arithmetically averaged. The effects of eddy currents and inverter dead-time were considered in [20]. In 2011, Yoon proposed the application of a square-wave injection instead of a sinusoidal one [21]. The new technique increases the injected frequency range, thus allowing a more precise estimation, and at the same it is able of reducing the acoustic noise generated by the PWM pattern. This strategy was also applied for motors with accessible star-point in [22] combining the advantages of a zero-sequence method, thus increased accuracy and stability, with the square-wave injection. Up to this point, except for the INFORM technique, only the HFI (high-frequency injection) techniques had been presented. It is clear that from the injection of an external pulsating or rotating carrier an acoustic noise signal is always generated. Moreover, the injection frequency must be chosen higher than the rotational frequency of the rotor but lower than the PWM frequency. This choice is not straightforward, for example, for small low-power high speed PMSMs. For that reason, techniques based on the direct modification of the PWM excitation pattern are sometimes preferable. Numerous contributions can be mentioned within this field of research.

Chronologically, after the presentation of the INFORM technique, a new method was proposed by Staines in [23]. Whereas the Schrödel technique is based on the injection of test pulses on the PWM signal, Staines considered the six non-zero switching states of the voltage source inverter (VSI) for the application of test vectors. This method can be referred to as Zero Sequence Current Derivative (ZSCD) technique. More precisely, the technique is based on the application of a pair of test vectors with the same amplitude and opposite directions for a short period between the normal PWM signal. The induced transient currents are measured by a Rogowski coil and the rotor position information can be then derived. As before, this technique has been developed for induction motors and then applied to generic AC machines [24]. The ZSCD method is more efficient in terms of estimation performance than the INFORM technique but it requires additional hardware in order to be implemented.

Afterwards, a new sensorless technique based on the calculation of current derivatives during the Zero Voltage Vector Injection (ZVVI) was proposed [25]. The presented method relies on the effect of both back-EMF and saliency characteristic of AC machines. No additional test signals are injected into the machine, thus no acoustic noise is generated, and the difficulties in sensing the machine terminal voltage at low speed is eased. In 2011, the Arbitrary Injection (AI) scheme for the sensorless field oriented control of PMSMs was presented [26]. This proposal for sensorless control method does not rely on a particular form of injection, thus the name arbitrary. The supporting idea is that the saliency angle information can be obtained by comparing the isotropic machine model with the real machine behavior. The difference between the calculated model currents and the measured currents provides the information about the angular position of the rotor. In [27], the same technique is investigated taking into account multiple saliencies of the machine.

Excluding the HFI technique based on the zero sequence voltage measurement, no other sensorless techniques presented to this point exploit the information carried by the measurement of the star-point voltage of the machine. The main reason is that for most applications, such as the torque control of the motor, current sensors cannot be avoided and it is practical to utilize them also for sensorless purposes. On the other hand, for those applications which do not require current sensors, their elimination would bring the drive system to diminish its size and cost. This is particularly relevant in embedded drive systems applications, where miniaturization of the electronics plays a very important role. Moreover, voltage measurements are characterized by an higher signal-to-noise ratio and larger bandwidth compared to current measurements. The first attempt to exploit the zero sequence voltage measurement for sensorless operation was made by Consoli in [28]. The research was firstly conducted on induction machines. The works presented by Holtz also introduced new strategies and improvements in this direction still considering induction motors [29–31]. In the field of BLDC motors, an interesting approach was proposed for sensorless operation by means of zero-sequence voltage measurements [32]. This method utilizes the Induced Voltage caused by Magnetic Saturation (IVMS) of the machine. The authors claim that this technique can operate also with magnetically saturated machines. In 2000, the strategy of Consoli was transposed to the PMSM operation [33].

Starting from the last contribution, another technique was proposed in [34], that led to the so-called Direct Flux Control (DFC). Since this work is mainly based on the DFC technique, a more detailed description of its functioning and its evolution over the years will be presented. The DFC method is based on the evaluation of the inductance variations of a star-connected PMSM by measuring the transients of the neutral-point voltage when the machine is excited by means of a proper PWM pattern. In this way, the technique was described by Thiemann and Mantala in [35, 36]. In particular, these works provided a practical approach to the implementation of the technique togheter with first results about the electrical position estimation. As shown in [37–39], the design of the machine has a direct effect on the anisotropy information carried by the DFC signals. In particular, the scientific contributions proved that different anisotropy signals are obtained by each PMSM referring to the geometry and the position of the permanent magnets, the windings configuration and the pole-slot set-up. Hence, the machine design influences directly the estimated sensorless electrical position. Nevertheless, in [40–42], the aforementioned technique has been proven to obtain high-performance performance in driving low power PMSMs. Issues and limitations of applicability of the DFC techniques are also highligthed by the mentioned works. One of

these issues is the presence of switching electronic noise in the measured voltages. Therefore, low-noise electronics should be used for the measurement process of the anisotropy information. In order to overcome this issue, a Fast Resettable Integrator Circuit (FRIC) capable of providing better measurements for the implementation of the DFC technique by means of an improved signal-to-noise ratio was proposed in [43–45]. The new proposed circuitry extends the application of the technique to high-load conditions and reduces the influence of the ringing generated by the three-phase inverter. A proper tuning of the FRIC circuitry can lead to an augmented sensitivity of the measurements for those motors exhibiting weak anisotropy. Another approach for the reduction of the measurement noise was proposed in [45] where a Sliding Mode Differentiator has been applied. Over the years, the analyses performed on the DFC technique have also shown that the technique works better in the low speed range. Hence, in order to overcome this limitation, in [46] the technique has been combined with back-EMF information in order to extend the speed range also to high speeds using an Extended Kalman Filter. Moreover, the DFC technique has been successfully used in several practical applications such as the identification of electrical and mechanical parameters of PMSMs [47] and the estimation of load torque using state observation techniques [48].

1.2 Scientific motivation and focus of this work

The presented techniques for the sensorless control of electrical machines are so heterogeneous that they can fit almost every system requirement. As mentioned, sensorless techniques based on the exploitation of the star-point voltage are suitable for low-power motors whose embedded system is based on low cost electronics and do not require current sensors. Although this category of techniques needs an accessible star-point, which is not available for a large part of the motors present on the market, it can provide interesting advantages when applied to PMSMs and for some applications, such as the possibility of developing sensorless techniques relying on higher signal-to-noise ratio measurements, since they do not require current but rather voltage sensors. For that reason, this work focuses on the application of the DFC technique. Besides the advantages provided by the use of this technique, it has been proven that the DFC method exhibits a systematic error on the estimated position that is dependent on the magnetic characteristics of the machine. Obviously, this error does not only negatively affect the drive of the motor but also the estimation of the speed and currents and, consequently, their control. Moreover, the presence of a systematic error deteriorates the performance of a potential state observer for the estimation of the external load torque. This work addresses these issues by introducing a new static iterative algorithm for the reduction of the position error. This algorithm, called IVD (Iterative Vector Decoupling), is based on the multiple iteration of the position estimation process and it requires the knowledge of only one parameter. The mathematical proof of the algorithm convergence to the real position is provided and its sensitivity to parameter variations should be analyzed. Moreover, the combination of the IVD technique with a state observer, namely a Kalman filter, is proposed. The use of a state observer provides an additional tool for the rejection of disturbances and, thanks to the IVD, the estimation of the external load torque is enhanced.

1.3 Work structure

The contents of each chapter of this work can be summarized as follows. In Chapter 2, the mathematical model of the PMSM as well as its control strategy are presented in order to introduce the DFC technique operations and the extraction of the DFC signals. The machine star-point voltage dynamic is thoroughly presented within a detailed mathematical description. Chapter 3 presents the relation between the DFC signals and the rotor angular position. Considerations about the effects of position estimation error on the drive of the machine are made and an iterative algorithm for the improvement of the estimated position is proposed. The use of a state observer for the further improvement of the estimation process is presented in Chapter 4. Moreover, the performances of the combination of the iterative algorithm with an RLS estimation method are presented by means of simulation results. Chapter 5 provides the experimantal validations of the theory presented within the previous chapters. In particular, two PMSMs with different characteristic are tested. Eventually, conclusions are drawn in Chapter 5.3, summarizing and discussing the main results of this work, and an outlook on further research works is provided.

2 Mathematical Foundation

Within this chapter the mathematical derivation of the Direct Flux Control sensorless technique is presented.This chapter presents mathematical formulations and figures firstly introduced in [49] by E. Grasso. It is a result of a strictly collaboration with him, since his work provides a solid basis for the original scientific contributions that will be presented starting from chapter 3. Hence, the text presents strong similarities with his thesis but it does not claim to provide any innovative or original ideas.
Firstly, the mathematical model of a PMSM is revealed in order to provide a common notation and a solid structure for the understanding of its operation. Afterwards, the Field Oriented Control (FOC) is recalled as control strategy for the driving of the machine. The introduction of the FOC is useful since it offers a tool for the simplification of the mathematics, thanks to a transformation of the system coordinates, and at the same time provides the basic concept of drive and control of a PMSM. The before mentioned section is completed by the introduction of the PWM excitation method for the electrical machine, namely, the Space Vector Modulation (SVM). Besides its importance for the actuation of the control strategy, the SVM provides the mathematical foundation for the derivation of the DFC technique. In fact, starting from the exploitation of the star point voltage dynamic due to the machine anisotropy, a modification of the SVM pattern allows to extract the DFC signals using the measured star point voltage, which will be used for the estimation of the electrical rotor position presented in the next chapter.

2.1 Mathematical model of a PMSM

A PMSM is an electrical motor constituted of two mechanical parts, namely: the stator, which is predisposed to generate a magnetic field through the exploitation of electromagnets, and the rotor, which is the rotary part and it is constituted of permanent magnets. In case of three-phase PMSMs, the stator electromagnets, which are constituted of coils wound around magnets, are placed spatially at 120° of phase shift from each other and they can be represented, as shown in Figure (2.1), in a three axis reference system. The proper excitation of these coils will generate a magnetic field that interacts with the field produced by the rotor permanent magnets generating a mechanical torque.
In order to understand completely the functioning concepts of a PMSM, let us present the mathematical equations in matricial form that model the motor starting from its electrical part:

$$\mathbf{v}_{abc} = \mathbf{R}\mathbf{i}_{abc} + \frac{\mathrm{d}\boldsymbol{\lambda}_{abc}}{\mathrm{d}t}, \tag{2.1}$$

$$\mathbf{v}_{abc} = \begin{bmatrix} v_{AN} \\ v_{BN} \\ v_{CN} \end{bmatrix} \quad \text{voltage vector,} \tag{2.2}$$

$$\mathbf{i}_{abc} = \begin{bmatrix} i_A \\ i_B \\ i_C \end{bmatrix} \quad \text{current vector,} \tag{2.3}$$

$$\boldsymbol{\lambda}_{abc} = \begin{bmatrix} \lambda_A \\ \lambda_B \\ \lambda_C \end{bmatrix} \quad \text{flux linkage vector.} \tag{2.4}$$

The voltages v_{AN}, v_{BN} and v_{CN} are the phase voltages. The matrix $\mathbf{R}$ is typically diagonal and its entries are identical. The flux linkage vector $\boldsymbol{\lambda}_{abc}$ is the sum of the flux generated by the stator and the flux provided by the rotor:

$$\boldsymbol{\lambda}_{abc} = \mathbf{L}_{abc}\mathbf{i}_{abc} + \boldsymbol{\lambda}_{PM}, \tag{2.5}$$

where $\mathbf{L}_{abc}$ is the machine phase inductance matrix and $\boldsymbol{\lambda}_{PM}$ is the rotor flux.

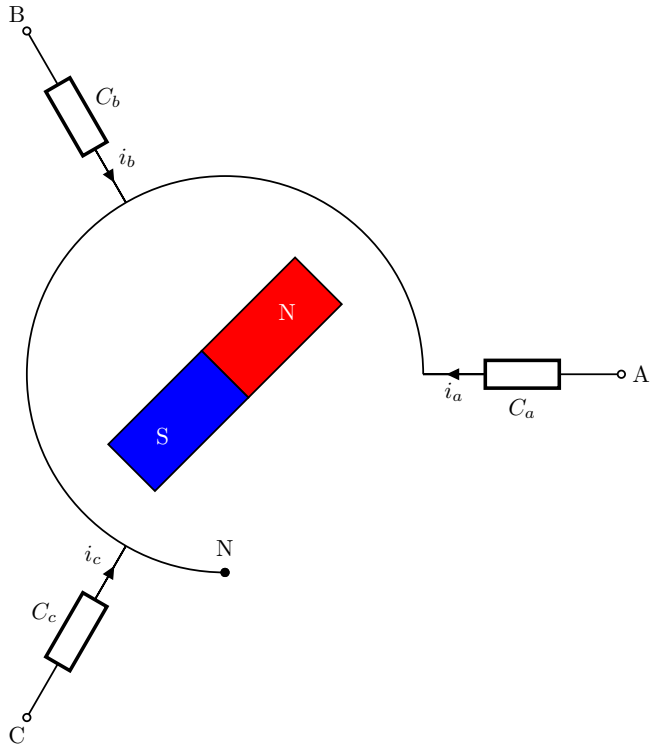

Figure 2.1: Schematic of a synchronous machine with accessible star-point.

In our case the rotor flux is considered constant since it is generated by the permanent magnets. The electrical equation of the machine can now be expressed as:

$$\begin{aligned}\mathbf{v}_{abc} &= \mathbf{R}\mathbf{i}_{abc} + \frac{\mathrm{d}\left(\mathbf{L}_{abc}\mathbf{i}_{abc}\right)}{\mathrm{d}t} + \frac{\mathrm{d}\boldsymbol{\lambda}_{PM}}{\mathrm{d}t} \\ &= \mathbf{R}\mathbf{i}_{abc} + \frac{\mathrm{d}\mathbf{L}_{abc}}{\mathrm{d}t}\mathbf{i}_{abc} + \mathbf{L}_{abc}\frac{\mathrm{d}\mathbf{i}_{abc}}{\mathrm{d}t} + \frac{\mathrm{d}\boldsymbol{\lambda}_{PM}}{\mathrm{d}t}.\end{aligned} \tag{2.6}$$

The rotor flux direction as well as the phase inductance matrix are a function of the electrical rotor position. For this reason, the derivatives of these quantities with respect to time in equation (2.6) can be rearranged and written as:

$$\begin{aligned}\mathbf{v}_{abc} &= \mathbf{R}\mathbf{i}_{abc} + \frac{\mathrm{d}\theta_e}{\mathrm{d}t}\frac{\partial\mathbf{L}_{abc}}{\partial\theta_e}\mathbf{i}_{abc} + \mathbf{L}_{abc}\frac{\mathrm{d}\mathbf{i}_{abc}}{\mathrm{d}t} + \frac{\mathrm{d}\theta_e}{\mathrm{d}t}\frac{\partial\boldsymbol{\lambda}_{PM}}{\partial\theta_e} \\ &= \mathbf{R}\mathbf{i}_{abc} + \mathbf{L}_{abc}\frac{\mathrm{d}\mathbf{i}_{abc}}{\mathrm{d}t} + \omega_e\frac{\partial\mathbf{L}_{abc}}{\partial\theta_e}\mathbf{i}_{abc} + \omega_e\frac{\partial\boldsymbol{\lambda}_{PM}}{\partial\theta_e},\end{aligned} \tag{2.7}$$

where θ_e and ω_e are the electrical rotor position and speed, respectively. Without loss of generalization, one can pose the following definition for the rotor flux:

$$\boldsymbol{\lambda}_{PM} = \Psi_{PM}\begin{bmatrix}\cos\left(\theta_e\right)\\ \cos\left(\theta_e - \frac{2}{3}\pi\right)\\ \cos\left(\theta_e + \frac{2}{3}\pi\right)\end{bmatrix} \rightarrow \frac{\partial\boldsymbol{\lambda}_{PM}}{\partial\theta_e} = \mathbf{e}_{abc} = -\Psi_{PM}\begin{bmatrix}\sin\left(\theta_e\right)\\ \sin\left(\theta_e - \frac{2}{3}\pi\right)\\ \sin\left(\theta_e + \frac{2}{3}\pi\right)\end{bmatrix}, \tag{2.8}$$

and, eventually, we come to the following form:

$$\mathbf{v}_{abc} = \underbrace{\mathbf{R}\mathbf{i}_{abc} + \mathbf{L}_{abc}\frac{\mathrm{d}\mathbf{i}_{abc}}{\mathrm{d}t}}_{\text{RL circuit part}} + \underbrace{\omega_e\frac{\partial\mathbf{L}_{abc}}{\partial\theta_e}\mathbf{i}_{abc}}_{\substack{\text{anysothropy}\\ \text{dependent part}}} + \underbrace{\omega_e\mathbf{e}_{abc}}_{\text{BEMF part}}. \tag{2.9}$$

The inductance matrix $\mathbf{L}_{abc}$ is typically a symmetric matrix, whose values are the self and mutual inductances of the machine phases.
The mechanical differential equation of the PMSM can be now be presented. It is obtained from the torque equilibrium on the shaft and can be expressed as:

$$\Xi_e - \Xi_l = J\frac{\mathrm{d}\omega_m}{\mathrm{d}t} + f\left(\omega_m\right), \tag{2.10}$$

where Ξ_e is the electromagnetic torque generated by the motor, Ξ_l the load torque applied on the rotor shaft from the environment, J is the rotor inertia, ω_m is the mechanical angular speed of the rotor and $f\left(\omega_m\right)$ is a term that models the viscous friction as well as other friction components that are acting on the rotor shaft. Its most common and simple definition is: $f\left(\omega_m\right) = B\omega_m$ where B is the viscous friction coefficient. In order to derive the expression

of the electromagnetic torque Ξ_e, the input power of the PMSM, P_e, is considered:

$$\begin{aligned} P_e &= \frac{3}{2} n_{pp} \mathbf{i}_{abc}^T \mathbf{v}_{abc} \\ &= \frac{3}{2} n_{pp} \left(\underbrace{\mathbf{i}_{abc}^T \mathbf{R} \mathbf{i}_{abc}}_{\substack{\text{resistive} \\ \text{power loss}}} + \underbrace{\mathbf{i}_{abc}^T \mathbf{L}_{abc} \frac{\mathrm{d}\mathbf{i}_{abc}}{\mathrm{d}t}}_{\substack{\text{rate of change of} \\ \text{magnetic energy}}} + \underbrace{\omega_e \mathbf{i}_{abc}^T \frac{\partial \mathbf{L}_{abc}}{\partial \theta_e} \mathbf{i}_{abc} + \omega_e \mathbf{i}_{abc}^T \mathbf{e}_{abc}}_{\text{air-gap power}} \right) \\ &= P_{\text{loss}} + P_{\text{mag}} + P_{\text{air}}. \end{aligned} \tag{2.11}$$

The input power P_e is the sum of three components: the resistive power losses, the rate of change of magnetic energy and the air gap power. The latter term is related to the generated electromagnetic torque, that can be derived as follows:

$$P_{\text{air}} = \omega_m \Xi_e = \frac{\omega_e}{n_{pp}} \Xi_e, \tag{2.12}$$

hence:

$$\Xi_e = \frac{3}{2} n_{pp}^2 \left(\mathbf{i}_{abc}^T \frac{\partial \mathbf{L}_{abc}}{\partial \theta_e} \mathbf{i}_{abc} + \mathbf{i}_{abc}^T \mathbf{e}_{abc} \right), \tag{2.13}$$

where n_{pp} is the number of pole pairs of the machine and $\omega_e = n_{pp} \omega_m$.

2.2 Field Oriented Control

As shown in the previous section, the generation of torque at the shaft of the motor is strictly dependent on the current vector and, consequently, on the excitation of the stator coils. Considering equation (2.13), we can state that, for PMSMs, the most efficient way to generate torque is to let the current vector $\mathbf{i}_{abc}$ and the vector $\mathbf{e}_{abc}$ be orthogonal. This task is not trivial if we consider the equations presented in the previous section. In order to generate torque, the most simple approach is the scalar control method, also called V/f (Volt per Hertz) control. This method is based on an injection of a rotating voltage vector at the machine terminals which frequency increases up to the desired angular speed whereas its amplitude is controlled in order to maintain the ratio V/f constant. Despite its simplicity, this approach does not achieve the maximization of the torque since the currents are not directly controlled and, in case of PMSMs, it could let the system be unstable. In order to reach the full torque at any speed, the FOC can be used. This approach is based on the transformation of the motor quantities from a three axis stationary reference frame to a two axis orthogonal rotary frame. Consequently, the currents are also defined as a two component vector, respectively, one for the generation of magnetic flux, the other for the torque. A control strategy can be then applied to this new reference frame, for example by means of PI controllers. Let us now present the form of the transformation matrices and how they modify the motor differential equations.

2.2.1 Stator reference frame: Clarke transformation

The stator reference frame is an orthogonal three axes system forming the triple (α, β, γ) that is fixed to the stator and, by definition, aligns the axis α with the axis of the phase a. In order to derive the mathematical model of the synchronous machine in the stator reference system, the Clark transformation matrix $\mathbf{T}_C$ can be used:

$$\mathbf{T}_C = \frac{2}{3}\begin{bmatrix} 1 & \frac{1}{2} & \frac{1}{2} \\ 0 & \frac{\sqrt{3}}{2} & -\frac{\sqrt{3}}{2} \\ \frac{1}{2} & \frac{1}{2} & \frac{1}{2} \end{bmatrix}, \qquad \mathbf{T}_C^{-1} = \frac{2}{3}\begin{bmatrix} 1 & 0 & 1 \\ -\frac{1}{2} & \frac{\sqrt{3}}{2} & 1 \\ -\frac{1}{2} & \frac{\sqrt{3}}{2} & 1 \end{bmatrix}, \tag{2.14}$$

and the following vectors can be defined:

$$\begin{aligned} \mathbf{i}_{\alpha\beta\gamma} &= \mathbf{T}_C \mathbf{i}_{abc}, \quad \mathbf{i}_{abc} = \mathbf{T}_C^{-1}\mathbf{i}_{\alpha\beta\gamma}, \\ \mathbf{v}_{\alpha\beta\gamma} &= \mathbf{T}_C \mathbf{v}_{abc}, \quad \mathbf{v}_{abc} = \mathbf{T}_C^{-1}\mathbf{v}_{\alpha\beta\gamma}, \\ \mathbf{e}_{\alpha\beta\gamma} &= \mathbf{T}_C \mathbf{e}_{abc}, \quad \mathbf{e}_{abc} = \mathbf{T}_C^{-1}\mathbf{e}_{\alpha\beta\gamma}. \end{aligned} \tag{2.15}$$

Thus, the electrical equations can be derived as follows:

$$\begin{aligned} \mathbf{v}_{\alpha\beta\gamma} &= \mathbf{T}_C \mathbf{v}_{abc} = \mathbf{T}_C \mathbf{R} \mathbf{i}_{abc} + \mathbf{T}_C \mathbf{L}_{abc} \frac{\mathrm{d}}{\mathrm{d}t}\mathbf{i}_{abc} + \mathbf{T}_C \frac{\partial \mathbf{L}_{abc}}{\partial \theta_e}\mathbf{i}_{abc}\omega_e + \mathbf{T}_C \mathbf{e}_{abc}\omega_e \\ &= \mathbf{T}_C \mathbf{R} \mathbf{T}_C^{-1}\mathbf{i}_{\alpha\beta\gamma} + \mathbf{T}_C \mathbf{L}_{abc} \frac{\mathrm{d}}{\mathrm{d}t}\mathbf{T}_C^{-1}\mathbf{i}_{\alpha\beta\gamma} + \mathbf{T}_C \frac{\partial \mathbf{L}_{abc}}{\partial \theta_e}\mathbf{T}_C^{-1}\mathbf{i}_{\alpha\beta\gamma}\omega_e + \mathbf{T}_C \mathbf{e}_{abc}\omega_e \\ &= \mathbf{R} i_{\alpha\beta\gamma} + \mathbf{L}_{\alpha\beta\gamma} \frac{\mathrm{d}}{\mathrm{d}t}\mathbf{i}_{\alpha\beta\gamma} + \frac{\partial \mathbf{L}_{\alpha\beta\gamma}}{\partial \theta_e}\mathbf{i}_{\alpha\beta\gamma}\omega_e + \mathbf{e}_{\alpha\beta\gamma}\omega_e, \end{aligned} \tag{2.16}$$

where the machine phase inductance matrix in the stator reference frame has been defined as:

$$\mathbf{L}_{\alpha\beta\gamma} = \mathbf{T}_C \mathbf{L}_{abc} \mathbf{T}_C^{-1}. \tag{2.17}$$

As in the case of the three phase reference frame, the electromagnetic torque can be derived and results to be:

$$\Xi_e = \frac{3}{2} n_{pp} \left(\mathbf{i}_{\alpha\beta\gamma}^T \frac{\partial \mathbf{L}_{\alpha\beta\gamma}}{\partial \theta_e}\mathbf{i}_{\alpha\beta\gamma} + \mathbf{i}_{\alpha\beta\gamma}^T \mathbf{e}_{\alpha\beta\gamma} \right). \tag{2.18}$$

Finally, it can be easily calculated that:

$$\mathbf{e}_{\alpha\beta\gamma} = \Psi_{PM} \begin{bmatrix} -\sin(\theta_e) \\ \cos(\theta_e) \\ 0 \end{bmatrix}. \tag{2.19}$$

We can notice that the stator reference system reduces into a two phase system in case of star connected motor. In fact, applying the Kirchhoff's circuit law at the star-point N, the

following equation holds:

$$i_a + i_b + i_c = 0, \tag{2.20}$$

hence:

$$i_\gamma = 0. \tag{2.21}$$

That condition holds if none , or at least very small, parasitic capacities are present between the star-point N and ground O. Since this assumption is almost always satisfied, the γ equation can be avoided. Thus, the system passes from a three phase to a two phase reference frame.

2.2.2 Rotor reference frame: Park transformation

In order to derive the mathematical model of the machine in the rotor reference system, the Park transformation matrix $\mathbf{T}_P$ can be used:

$$\mathbf{T}_P = \begin{bmatrix} \cos(\theta_e) & \sin(\theta_e) & 0 \\ -\sin(\theta_e) & \cos(\theta_e) & 0 \\ 0 & 0 & 1 \end{bmatrix}, \qquad \mathbf{T}_P^{-1} = \begin{bmatrix} \cos(\theta_e) & -\sin(\theta_e) & 0 \\ \sin(\theta_e) & \cos(\theta_e) & 0 \\ 0 & 0 & 1 \end{bmatrix}, \tag{2.22}$$

that, differently from the Clark transformation matrix, is an orthogonal matrix, i.e. ($\mathbf{T}_P^{-1} = \mathbf{T}_P^T$). The following vectors can be then defined:

$$\begin{aligned} \mathbf{v}_{dqo} &= \mathbf{T}_P \mathbf{v}_{\alpha\beta\gamma}, \quad \mathbf{v}_{\alpha\beta\gamma} = \mathbf{T}_P^{-1} \mathbf{v}_{dqo}, \\ \mathbf{i}_{dqo} &= \mathbf{T}_P \mathbf{i}_{\alpha\beta\gamma}, \quad \mathbf{i}_{\alpha\beta\gamma} = \mathbf{T}_P^{-1} \mathbf{i}_{dqo}, \\ \mathbf{e}_{dqo} &= \mathbf{T}_P \mathbf{e}_{\alpha\beta\gamma}, \quad \mathbf{e}_{\alpha\beta\gamma} = \mathbf{T}_P^{-1} \mathbf{e}_{dqo}. \end{aligned} \tag{2.23}$$

The electrical equations can be derived as follows:

$$\begin{aligned} \mathbf{v}_{dqo} &= \mathbf{T}_P \mathbf{v}_{\alpha\beta\gamma} = \mathbf{T}_P \mathbf{R} \mathbf{i}_{\alpha\beta\gamma} + \mathbf{T}_P \mathbf{L}_{\alpha\beta\gamma} \frac{\mathrm{d}}{\mathrm{d}t} \mathbf{i}_{\alpha\beta\gamma} + \mathbf{T}_P \frac{\partial \mathbf{L}_{\alpha\beta\gamma}}{\partial \theta_e} \mathbf{i}_{\alpha\beta\gamma} \omega_e + \mathbf{T}_P \mathbf{e}_{\alpha\beta\gamma} \omega_e \\ &= \mathbf{T}_P \mathbf{R} \mathbf{T}_P^{-1} \mathbf{i}_{dqo} + \mathbf{T}_P \mathbf{L}_{\alpha\beta\gamma} \frac{\mathrm{d}}{\mathrm{d}t} \left(\mathbf{T}_P^{-1} \mathbf{i}_{dqo} \right) + \mathbf{T}_P \frac{\partial \mathbf{L}_{\alpha\beta\gamma}}{\partial \theta_e} \mathbf{T}_P^{-1} \mathbf{i}_{dqo} \omega_e + \mathbf{T}_P \mathbf{e}_{\alpha\beta\gamma} \omega_e. \end{aligned} \tag{2.24}$$

Let us define the phase inductance matrix in the rotor reference frame as:

$$\mathbf{L}_{dqo} = \mathbf{T}_P \mathbf{L}_{\alpha\beta\gamma} \mathbf{T}_P^{-1}. \tag{2.25}$$

Also, since the Park transformation matrix, differently from the Clark transformation matrix, is a function of the angle θ_e, it is important to note that:

$$\frac{\mathrm{d}\mathbf{i}_{\alpha\beta\gamma}}{\mathrm{d}t} = \frac{\mathrm{d}}{\mathrm{d}t} \left(\mathbf{T}_P^{-1} \mathbf{i}_{dqo} \right) = \mathbf{T}_P^{-1} \frac{\mathrm{d}}{\mathrm{d}t} \mathbf{i}_{dqo} + \frac{\mathrm{d}\mathbf{T}_P^{-1}}{\mathrm{d}t} \mathbf{i}_{dqo} = \mathbf{T}_P^{-1} \frac{\mathrm{d}}{\mathrm{d}t} \mathbf{i}_{dqo} + \frac{\partial \mathbf{T}_P^{-1}}{\partial \theta_e} \mathbf{i}_{dqo} \omega_e. \tag{2.26}$$

For the same reason, the expression $\mathbf{T}_P \frac{\partial \mathbf{L}_{\alpha\beta\gamma}}{\partial \theta_e} \mathbf{T}_P^{-1}$ is not equivalent to $\frac{\partial \mathbf{L}_{dqo}}{\partial \theta_e}$. Thus, the electrical equation is expressed as:

$$\begin{aligned}\mathbf{v}_{dqo} &= \mathbf{R}\mathbf{i}_{dqo} + \mathbf{T}_P \mathbf{L}_{\alpha\beta\gamma} \mathbf{T}_P^{-1} \frac{\mathrm{d}}{\mathrm{d}t}\mathbf{i}_{dqo} + \mathbf{T}_P \mathbf{L}_{\alpha\beta\gamma} \frac{\partial \mathbf{T}_P^{-1}}{\partial \theta_e}\mathbf{i}_{dqo}\omega_e + \mathbf{T}_P \frac{\partial \mathbf{L}_{\alpha\beta\gamma}}{\partial \theta_e}\mathbf{T}_P^{-1}\mathbf{i}_{dqo}\omega_e + \mathbf{e}_{dqo}\omega_e \\ &= \mathbf{R}\mathbf{i}_{dqo} + \mathbf{L}_{dqo}\frac{\mathrm{d}}{\mathrm{d}t}\mathbf{i}_{dqo} + \mathbf{T}_P\left(\mathbf{L}_{\alpha\beta\gamma}\frac{\partial \mathbf{T}_P^{-1}}{\partial \theta_e} + \frac{\partial \mathbf{L}_{\alpha\beta\gamma}}{\partial \theta_e}\mathbf{T}_P^{-1}\right)\mathbf{i}_{dqo}\omega_e + \mathbf{e}_{dqo}\omega_e.\end{aligned} \tag{2.27}$$

The electromagnetic torque can be easily derived and is expressed as:

$$\Xi_e = \frac{3}{2} n_{pp}\left(\mathbf{i}_{dqo}^T \mathbf{T}_P\left(\mathbf{L}_{\alpha\beta\gamma}\frac{\partial \mathbf{T}_P^{-1}}{\partial \theta_e} + \frac{\partial \mathbf{L}_{\alpha\beta\gamma}}{\partial \theta_e}\mathbf{T}_P^{-1}\right)\mathbf{i}_{dqo} + \mathbf{i}_{dqo}^T \mathbf{e}_{dqo}\right). \tag{2.28}$$

Finally, it is easy to verify that:

$$\mathbf{e}_{dqo} = \Psi_{PM}\begin{bmatrix}0\\1\\0\end{bmatrix}. \tag{2.29}$$

Thus:

$$\mathbf{i}_{dqo}^T \mathbf{e}_{dqo} = i_q \Psi_{PM}. \tag{2.30}$$

As for the previous case, the o component of the system can be neglected since $i_o = i_\gamma$.

2.2.3 Common definition of the inductance matrix

In commonly adopted models, the following machine inductance matrix is assumed:

$$\mathbf{L}_{abc} = \begin{bmatrix} L_0 + L_2\cos(2\theta_e) & -\frac{L_0}{2} + L_2\cos\left(2\theta_e - \frac{2\pi}{3}\right) & -\frac{L_0}{2} + L_2\cos\left(2\theta_e + \frac{2\pi}{3}\right) \\ -\frac{L_0}{2} + L_2\cos\left(2\theta_e - \frac{2\pi}{3}\right) & L_0 + L_2\cos\left(2\theta_e + \frac{2\pi}{3}\right) & -\frac{L_0}{2} + L_2\cos(2\theta_e) \\ -\frac{L_0}{2} + L_2\cos\left(2\theta_e + \frac{2\pi}{3}\right) & -\frac{L_0}{2} + L_2\cos(2\theta_e) & L_0 + L_2\cos\left(2\theta_e + \frac{4\pi}{3}\right) \end{bmatrix}, \tag{2.31}$$

where L_0 is the mean value of the phase self inductances and L_2 the amplitude of their modulation on twice the electrical rotor position. Also, the mean value of the mutual inductances is assumed equal to $-\frac{L_0}{2}$ and having equal modulation amplitude. This assumption holds for the case where no stator magnetic saturation and slotting effects are considered. The derivative of this matrix with respect to the rotor position is then obtained:

$$\frac{\partial \mathbf{L}_{abc}}{\partial \theta_e} = -2L_2\begin{bmatrix} \sin(2\theta_e) & \sin\left(2\theta_e - \frac{2\pi}{3}\right) & \sin\left(2\theta_e + \frac{2\pi}{3}\right) \\ \sin\left(2\theta_e - \frac{2\pi}{3}\right) & \sin\left(2\theta_e + \frac{2\pi}{3}\right) & \sin(2\theta_e) \\ \sin\left(2\theta_e + \frac{2\pi}{3}\right) & \sin(2\theta_e) & \sin\left(2\theta_e + \frac{4\pi}{3}\right) \end{bmatrix}. \tag{2.32}$$

The machine phase inductance and its derivative with respect to the electrical rotor position can then be expressed also in the stator and rotor reference frames:

$$\mathbf{L}_{\alpha\beta\gamma} = \frac{3}{2}\begin{bmatrix} L_0 + L_2\cos(2\theta_e) & L_2\sin(2\theta_e) & 0 \\ L_2\sin(2\theta_e) & L_0 - L_2\cos(2\theta_e) & 0 \\ 0 & 0 & 0 \end{bmatrix}, \tag{2.33}$$

$$\frac{\partial \mathbf{L}_{\alpha\beta\gamma}}{\partial\theta_e} = 3\begin{bmatrix} -L_2\sin(2\theta_e) & L_2\cos(2\theta_e) & 0 \\ L_2\cos(2\theta_e) & L_2\sin(2\theta_e) & 0 \\ 0 & 0 & 0 \end{bmatrix}, \tag{2.34}$$

$$\mathbf{L}_{dqo} = \frac{3}{2}\begin{bmatrix} L_0 + L_2 & 0 & 0 \\ 0 & L_0 - L_2 & 0 \\ 0 & 0 & 0 \end{bmatrix} = \begin{bmatrix} L_d & 0 & 0 \\ 0 & L_q & 0 \\ 0 & 0 & 0 \end{bmatrix}, \tag{2.35}$$

$$\mathbf{T}_P\left(\mathbf{L}_{\alpha\beta\gamma}\frac{\partial \mathbf{T}_P^{-1}}{\partial\theta_e} + \frac{\partial \mathbf{L}_{\alpha\beta\gamma}}{\partial\theta_e}\mathbf{T}_P^{-1}\right) = \frac{3}{2}\begin{bmatrix} 0 & -L_0 + L_2 & 0 \\ L_0 + L_2 & 0 & 0 \\ 0 & 0 & 0 \end{bmatrix} = \begin{bmatrix} 0 & -L_q & 0 \\ L_d & 0 & 0 \\ 0 & 0 & 0. \end{bmatrix} \tag{2.36}$$

The electrical equations of the synchronous machine in the rotor reference frame and the electromagnetic torque can be finally derived:

$$\begin{aligned} v_d &= Ri_d + L_d\frac{\mathrm{d}i_d}{\mathrm{d}t} - L_q i_q\omega_e \\ v_q &= Ri_q + L_q\frac{\mathrm{d}i_q}{\mathrm{d}t} + L_d i_d\omega_e + \Psi_{PM}\omega_e \\ T_e &= \underbrace{\frac{3}{2}n_{pp}\Psi_{PM}i_q}_{\text{stator-rotor torque}} + \underbrace{\frac{3}{2}n_{pp}\left(L_{dd} - L_{qq}\right)i_d i_q}_{\text{reluctance torque}}. \end{aligned} \tag{2.37}$$

The $d-$ and $q-$axes are then coupled and the rotor speed has a contribution to this coupling effect. Moreover, the electromagnetic torque can now be more clearly divided in two components. The first one has been presented in the previous subsection. The second one, instead, is generated through the reluctance of the machine, that is the inductance difference between the $d-$ and $q-$directions. In particular, reluctance can change its value considerably depending on the permanent magnets alignment with the motor phases, since their permeability is close to the permeability of air. For the purpose of this doctoral thesis, only motors which present negligible reluctance torque, i.e. very low saliency, are considered. Hence, the control strategy will focus on the control of the i_q current as unique contribution to the torque and the i_d current as unique contribution to the flux generation.

2.2.4 Control strategy

Starting from the system presented in (2.37), the torque and consequently the rotation of the motor can be achieved by the direct control of the current i_q, the current i_d instead is used in order to perform flux weakening of the machine, i.e. for high-speed control of the motor. There are different control methods that can be considered for this purpose. The most common way is to use PI controllers. The schematic shown in Figure (2.2) presents clearly the FOC concept.

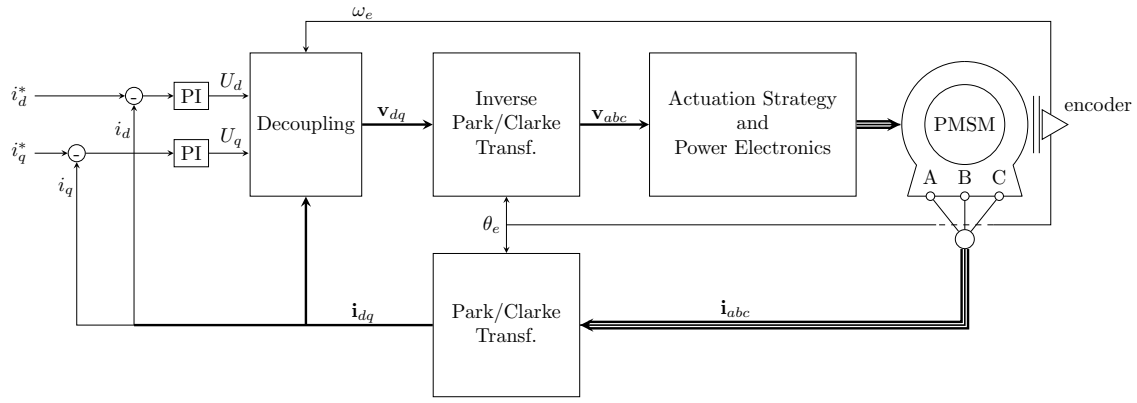

Figure 2.2: Schematic of the FOC with PI controllers for the control of the motor currents.

The PI controllers process the error between the reference current vector $\mathbf{i}_{dq}^*$ and the measured current vector $\mathbf{i}_{dq}$, that has been previously transformed applying the Park-Clarke transformation to the measured current vector $\mathbf{i}_{abc}$. Accordingly to (2.37), the $d-$ and $q-$equations are coupled to each other and this dependency varies linearly to the rotor speed. This coupling could lead the control to perform less efficiently and smoothly if the motor reaches high speeds. Usually, decoupling is proposed thorough a feedforward loop. In this case, the knowledge of the inductances L_d and L_q as well as the rotor speed ω_e are needed. Thus, the control output U_d^* and U_q^* are modified as follows:

$$\begin{aligned} v_d &= U_d + L_q i_q \omega_e, \\ v_q &= U_q - L_d i_d \omega_e, \end{aligned} \tag{2.38}$$

where v_d and v_q are the control output signals to be applied at the motor terminals. In order to do that, these signals are reconverted using the inverse transformations and fed into the actuator block, which modulates them and performs the actuation of the machine by means of a power electronic stage (discussed more deeply within the next section).
In order to perform the speed control of the motor, a second control loop can be realized, see Figure 2.3. Again, a PI controller can be used for this purpose.

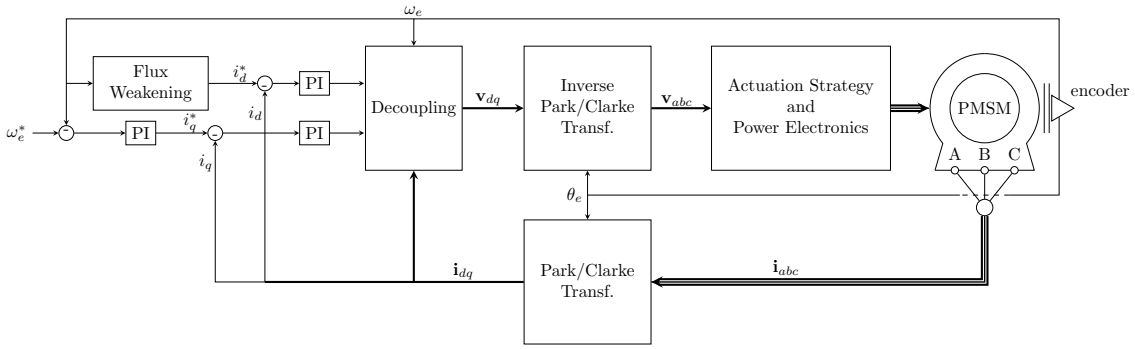

Figure 2.3: Schematic of the speed control of the PMSM.

There are different tuning methods that can be considered for the PI controllers. Commonly, the Amplitude Value Optimum (AVO) for the current loop and the Symmetrical Optimum (SO) for the speed control loop are used. Both methods aim at the optimization of a particular control aspect as described in [50]. The design objective of the AVO is to maintain the magnitude response of the control system as flat and as close to unity for a large a bandwidth as possible. Thus, the control is designed to have a very low settling time with low overshoots. On the other hand, the rejection of external disturbances is not optimized, because the path between disturbances and system output is not considered. Instead, the SO aims at optimize both control paths finding a trade-off between convergence rapidity to the reference point and disturbance rejection. The description and analysis of these tuning methods applied for PMSMs are presented [51].

2.2.5 Machine actuation strategy: Space Vector Modulation

The knowledge of the rotor angular position allows the control system to generate the desired vector command direction independently of the rotor speed. A three-phase inverter is typically used in order to apply the requested voltages at the machine terminals. This solution is based on a switching power electronic which convert the common DC link voltage into three alternating voltages applied at the machine phases by means of Pulse Width Modulation (PWM). Recalling the definitions of equation (2.2), the following phase voltages have to be achieved:

$$\mathbf{v}_{abc} = \begin{cases} v_{AN} = V_M \sin(\omega_e t) \\ v_{BN} = V_M \sin\left(\omega_e t - \frac{2}{3}\pi\right), \quad \text{where} \quad \omega_e t = \theta_e. \\ v_{CN} = V_M \sin\left(\omega_e t - \frac{4}{3}\pi\right) \end{cases} \tag{2.39}$$

The voltage vector $\mathbf{v}_{abc}$ can be written in a vectorial form in the stator reference frame as $\mathbf{v}_{\alpha\beta} = V_M e^{j\omega_e t}$, being V_M the amplitude of the vector and ω_e its angular speed. A three phase inverter with a unipolar input bus voltage v_{DC} is shown in Figure 2.4. Each leg of the inverter is provided with one low side and one high side switch. The point in between low and high sides is connected to the respective machine phase terminal. The switches are usually power transistors such as IGBTs or MosFETs. The specific properties of these transistors allow them to change its state from a short-circuit to an open-circuit and vice versa within a relative short time (in the order of ns for the MosFETs and μs for the IGBTs). Please note

that the voltages at the machine terminals are referred to GND and will be indicated as v_{XO} with $x \in \{A, B, C\}$ while the phase voltages (between terminal and neutral point N) will be indicated as v_{XN} with $x \in \{A, B, C\}$. Thus, it is easy to see that $v_{XO} = v_{XN} + v_{NO}$. Thus, the following holds:

$$\begin{aligned} v_{AN} &= v_{AO} - v_{NO}, \\ v_{BN} &= v_{BO} - v_{NO}, \\ v_{CN} &= v_{CO} - v_{NO}. \end{aligned} \tag{2.40}$$

Considering that the sum of the phase voltages equals zero, i.e. $v_{AN} + v_{BN} + v_{CN} = 0$, it is easy to verify that:

$$v_{NO} = \frac{1}{3}\left(v_{AO} + v_{BO} + v_{CO}\right). \tag{2.41}$$

Therefore, phase voltages can be expressed as function solely of the terminal voltages:

$$\begin{aligned} v_{AN} &= v_{AO} - \frac{1}{3}\left(v_{AO} + v_{BO} + v_{CO}\right), \\ v_{BN} &= v_{BO} - \frac{1}{3}\left(v_{AO} + v_{BO} + v_{CO}\right), \\ v_{CN} &= v_{CO} - \frac{1}{3}\left(v_{AO} + v_{BO} + v_{CO}\right). \end{aligned} \tag{2.42}$$

Considering Table 2.1, it is clear that only few discrete values of $\mathbf{v}_{abc}$ can be applied to the phase terminals. More precisely, a total of eight voltage configurations can be determined to which a voltage vector in the stator reference frame coincides. In order to obtain a wider range of applicable voltage, the Space Vector Modulation (SVM) is used.

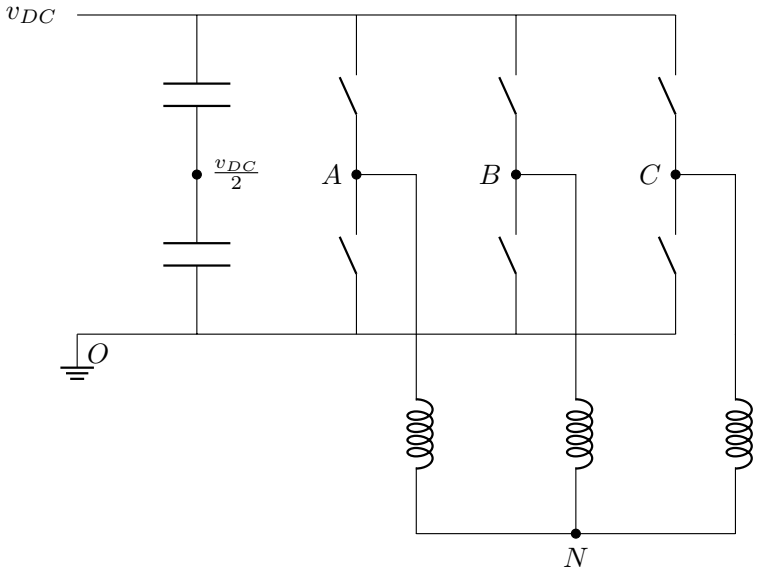

Figure 2.4: Schematic of a three-phase inverter with unipolar input voltage.

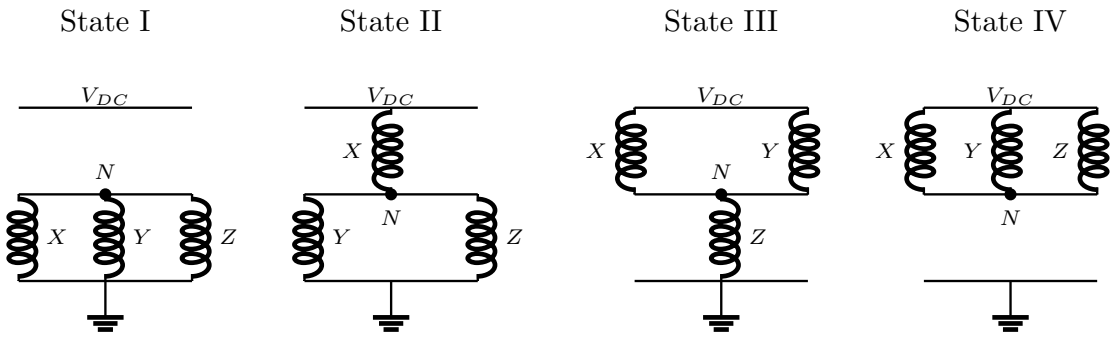

Figure 2.5: The four states of excitation of a synchronous machine where $X, Y, Z \in \{A, B, C\}$.

The SVM is a useful technique that allows determining the required duty cycle value at each PWM phase in order to obtain the desired phase voltage v_{XN}. Moreover, no tristate configuration of the inverter legs is allowed since the SVM considers only the possibility the transistors to be alternately open and close for each leg at every time instant. Under this assumption, one can identify the machine excitation states in Figure 2.5.

State	v_{AO}	v_{BO}	v_{CO}	$\mathbf{v}_{\alpha\beta}$
I	0	0	0	$\mathbf{v}_0$
II	v_{DC}	0	0	$\mathbf{v}_1$
III	v_{DC}	v_{DC}	0	$\mathbf{v}_2$
II	0	v_{DC}	0	$\mathbf{v}_3$
III	0	v_{DC}	v_{DC}	$\mathbf{v}_4$
II	0	0	v_{DC}	$\mathbf{v}_5$
III	v_{DC}	0	v_{DC}	$\mathbf{v}_6$
IV	v_{DC}	v_{DC}	v_{DC}	$\mathbf{v}_7$

Table 2.1: Vector configurations for the SVM-PWM technique.

The vectors can be displayed on the stator reference frame as in Figure 2.6. It can be noticed that the disposition of the vectors on the plane, excluding the vectors $\mathbf{v}_0$ and $\mathbf{v}_7$, forms an hexagon. The vectors, which have amplitude of $\frac{2}{3}v_{DC}$, define the distance between the vertices and the center of the hexagon, instead, the vectors $\mathbf{v}_0$ and $\mathbf{v}_7$ have no length, thus, they will be called zero-current vectors. The SVM-PWM technique combines multiple vectors in order to apply a mean voltage value, obtained through a PWM period, which is the desired voltage to be applied at the motor terminals. The circle inscribed within the hexagon defines the maximal amplitude of the voltage vector applicable. The radius r of this circle is defined as follows:

$$r = \frac{2}{3}\cos\left(\frac{\pi}{6}\right)v_{DC} = \frac{2}{3}\frac{\sqrt{3}}{2}v_{DC} = \frac{\sqrt{3}}{3}v_{DC}. \tag{2.43}$$

In Figure 2.7 an example of a possible vector combination is presented.

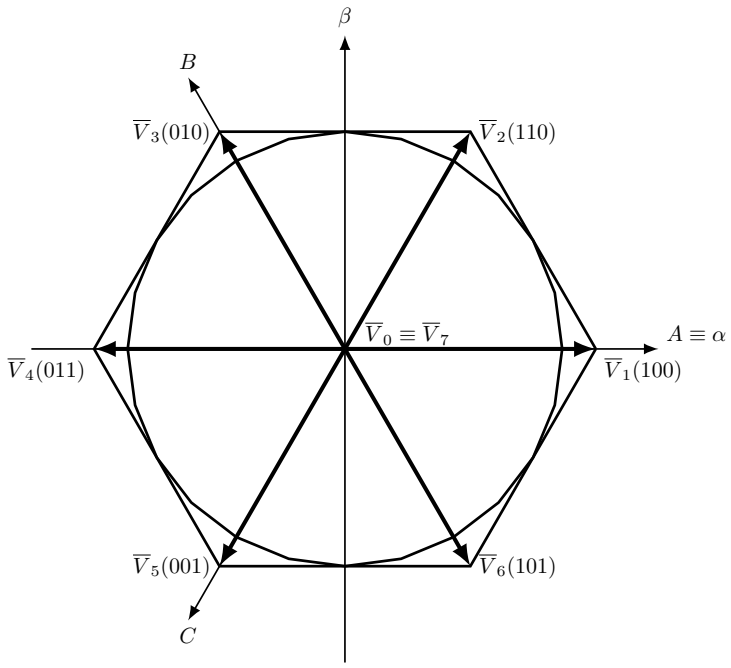

Figure 2.6: Voltage vectors $\mathbf{v}_i$, $i = 0,\ldots,7$ on the $\alpha - \beta$ plane.

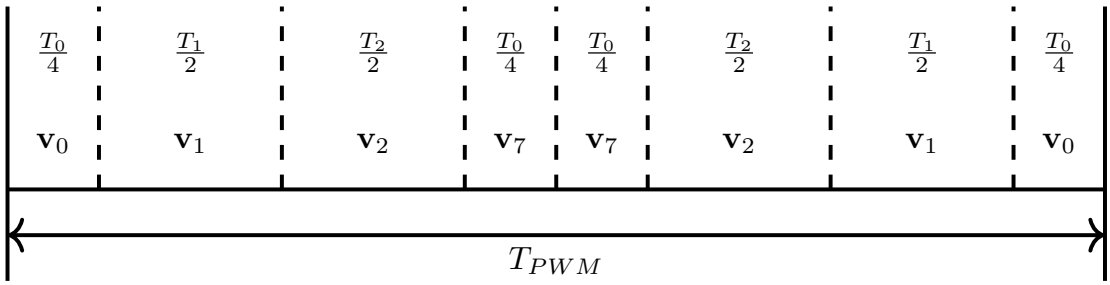

Figure 2.7: Center-aligned voltage vector succession in Space Vector Modulation.

The order of the applied vector within one PWM period does not change the amplitude of the resulting vector but it can modify the harmonic component of the induced currents. The presented schema in Figure 2.7 is based on the so-called center-aligned PWM due to its symmetry with respect to the time instant at the center of the T_{PWM} period. Another approach is the edge-aligned PWM which is usually more simple to be implemented. However, it can be shown that the center-aligned PWMs introduces less harmonics then its counterpart. Moreover, it also allows to perform one single switch at each transition. Assuming 0 when the low-side transistor is activated and 1 when the high-side transistor is activated, this can be represented as follows:

$\mathbf{v}_0$	$\mathbf{v}_1$	$\mathbf{v}_2$	$\mathbf{v}_7$	$\mathbf{v}_7$	$\mathbf{v}_2$	$\mathbf{v}_1$	$\mathbf{v}_0$
0	1	1	1	1	1	1	0
0	0	1	1	1	1	0	0
0	0	0	1	1	0	0	0

Each switch will be activated for a precise time $dc_X T_{PWM}$ with $X \in \{A, B, C\}$, where dc_X is the the duty cycle. Thus, the duty cycles of the three phases are:

$$\begin{aligned} dc_A &= \frac{T_1 + T_2 + \frac{T_0}{2}}{T_{PWM}} = \frac{T_{ON_A}}{T_{PWM}}, \\ dc_B &= \frac{T_2 + \frac{T_0}{2}}{T_{PWM}} = \frac{T_{ON_B}}{T_{PWM}}, \\ dc_C &= \frac{\frac{T_0}{2}}{T_{PWM}} = \frac{T_{ON_C}}{T_{PWM}}. \end{aligned} \tag{2.44}$$

Let us recall equation (2.42) for the determination of T_0, T_1 and T_2. It is possible to rewrite the equation as:

$$\begin{aligned} v_{AN} T_{PWM} &= v_{DC} T_{ON_A} - \frac{1}{3} v_{DC} \left(T_{ON_A} + T_{ON_B} + T_{ON_C} \right), \\ v_{BN} T_{PWM} &= v_{DC} T_{ON_B} - \frac{1}{3} v_{DC} \left(T_{ON_A} + T_{ON_B} + T_{ON_C} \right), \\ v_{CN} T_{PWM} &= v_{DC} T_{ON_C} - \frac{1}{3} v_{DC} \left(T_{ON_A} + T_{ON_B} + T_{ON_C} \right). \end{aligned} \tag{2.45}$$

By substituting the expression of T_{ON_X} with $X \in \{A, B, C\}$, after some algebraic calculation it is possible to find:

$$\begin{aligned} T_1 &= \frac{T_{PWM}}{v_{DC}} \left(2 v_{AN} + v_{CN} \right), \\ T_2 &= \frac{T_{PWM}}{v_{DC}} \left(-2 v_{CN} - v_{AN} \right). \end{aligned} \tag{2.46}$$

Hence, the following can be written:

$$\begin{aligned} v_{AN} T_{PWM} &= v_{DC} T_{ON_A} - \frac{1}{2} v_{DC} T_{PWM} + \frac{1}{2} \left(v_{AN} + v_{CN} \right), \\ v_{BN} T_{PWM} &= v_{DC} T_{ON_B} - \frac{1}{2} v_{DC} T_{PWM} + \frac{1}{2} \left(v_{AN} + v_{CN} \right), \\ v_{CN} T_{PWM} &= v_{DC} T_{ON_C} - \frac{1}{2} v_{DC} T_{PWM} + \frac{1}{2} \left(v_{AN} + v_{CN} \right). \end{aligned} \tag{2.47}$$

After the adjustment of these equations as:

$$\begin{aligned} \frac{v_{AN}}{v_{DC}} &= \frac{T_{ON_A}}{T_{PWM}} - \frac{1}{2} + \frac{1}{2} \left(\frac{v_{AN} + v_{CN}}{v_{DC}} \right), \\ \frac{v_{BN}}{v_{DC}} &= \frac{T_{ON_B}}{T_{PWM}} - \frac{1}{2} + \frac{1}{2} \left(\frac{v_{AN} + v_{CN}}{v_{DC}} \right), \\ \frac{v_{CN}}{v_{DC}} &= \frac{T_{ON_C}}{T_{PWM}} - \frac{1}{2} + \frac{1}{2} \left(\frac{v_{AN} + v_{CN}}{v_{DC}} \right), \end{aligned} \tag{2.48}$$

the duty cycles can be directly expressed as follows:

$$\begin{aligned} dc_A &= \frac{T_{ON_A}}{T_{PWM}} = \frac{v_{AN}}{v_{DC}} + \frac{1}{2} - \frac{1}{2}\left(\frac{v_{AN}+v_{CN}}{v_{DC}}\right), \\ dc_B &= \frac{T_{ON_B}}{T_{PWM}} = \frac{v_{BN}}{v_{DC}} + \frac{1}{2} - \frac{1}{2}\left(\frac{v_{AN}+v_{CN}}{v_{DC}}\right), \\ dc_C &= \frac{T_{ON_C}}{T_{PWM}} = \frac{v_{CN}}{v_{DC}} + \frac{1}{2} - \frac{1}{2}\left(\frac{v_{AN}+v_{CN}}{v_{DC}}\right). \end{aligned} \tag{2.49}$$

The previous equations refers to the application of a voltage vector lying between $\mathbf{v}_1$ and $\mathbf{v}_2$ Nevertheless, the generic equation for the determination of the duty cycle of each phase is expressed as follows:

$$dc_X = \frac{T_{ON_X}}{T_{PWM}} = \frac{v_{XN}}{v_{DC}} + \frac{1}{2} - \frac{1}{2}\left(\frac{\min\left(v_{AN}, v_{BN}, v_{CN}\right) + \max\left(v_{AN}, v_{BN}, v_{CN}\right)}{v_{DC}}\right), \tag{2.50}$$

where $X \in \{A, B, C\}$. The last term of this equation, $\frac{\min(v_{AN},v_{BN},v_{CN})+\max(v_{AN},v_{BN},v_{CN})}{v_{DC}}$, is called third harmonic component. This component represents an alternating signal with a frequency three times the frequency of v_{XN}. It is interesting to notice that v_{XO} is contained in $\pm\frac{v_{DC}}{2}$ while the phase voltage v_{XN} is contained in $\pm\frac{v_{DC}}{\sqrt{3}}$, as shown in Figure 2.8.

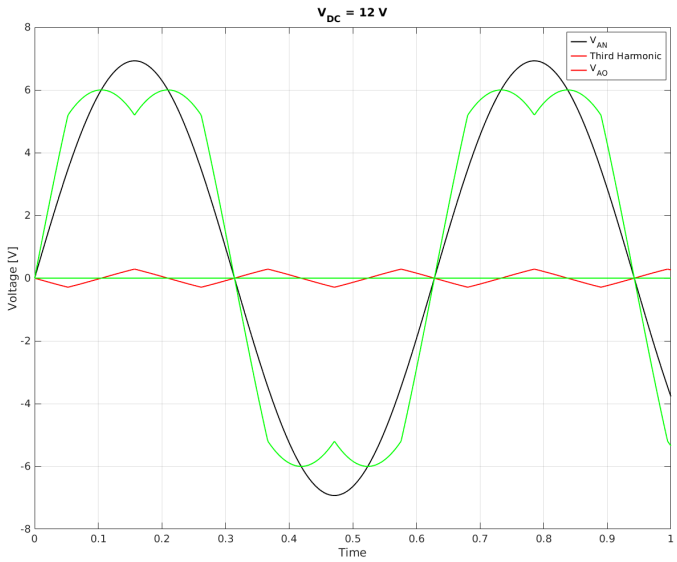

Figure 2.8: v_{AN}, v_{AO} and third harmonic component for the case $v_{DC} = 12V$

Finally, it is possible to observe that in the case of a star-connected synchronous machine, a third harmonic component has to be injected at the phase terminals in order to apply sinusoidal voltages on the machine phases.

2.3 Direct Flux Control for PMSMs

The control strategy previously presented is strictly dependent on the information about the angular rotor position since it is needed in order to perform the Park transformation necessary for the actuation of the FOC. The most straightforward solution to this issue is to mount a position sensor, for example an encoder, at the motor shaft. However, the introduction of an additional mechanical moving part to the plant could lead the system to be less reliable as well as more expensive in term of costs. Moreover, these issues could worsen if small low-power motors are considered since smaller sensors are more expensive and fragile than their bigger counterpart. In order to avoid the utilization of external mechanical sensors, the implementation of a sensorless technique is considered. Among several techniques, the Direct Flux Control (DFC) is a sensorless technique particularly suited for low-power PMSMs with accessible star-point. In fact, the exploitation of the behavior of the star-point provides information about the machine phase inductances and consequently about the rotor position for those machines whose phase inductances are modulated by the rotor flux. Firstly, the mathematical model of the star-point voltage dynamic will be presented in order to give a better understanding of the DFC technique. Then, the extraction process of the DFC signals will thoroughly described. The estimation of the rotor position will be presented within the next chapter.

2.3.1 Mathematical model of the star-point voltage dynamic

Within the previous section, the assumption of a static behavior of the star-point voltage has been considered in order to derive the SVM-PWM technique. For this purpose, the proposed model can be considered accurate enough. Nevertheless, the star-point voltage v_{NO} has actually a dependency on the machine dynamics and its behavior in relation to the applied terminal voltages is the foundation of the DFC technique. A more accurate modeling of the v_{NO} dynamic is essential in order to understand the functioning of this sensorless method. Let us recall the electrical equation of the synchronous machine in the phase reference frame, introduced previously in equation (2.51), with explicit time dependency:

$$\mathbf{v}_{abc}(t) = \mathbf{R}\mathbf{i}_{abc}(t) + \mathbf{L}_{abc}(\theta_e(t))\frac{\mathrm{d}\mathbf{i}_{abc}(t)}{\mathrm{d}t} + \frac{\mathrm{d}\mathbf{L}_{abc}(\theta_e(t))}{\mathrm{d}t}\mathbf{i}_{abc}(t) + \mathbf{e}_{abc}(\theta_e(t))\,\omega_e(t)\,, \quad (2.51)$$

where $\mathbf{L}_{abc}$, $\mathbf{e}_{abc}$ and ω_e are time-dependent. Since the frequency component of the voltage signals applied is much higher than the bandwidth of the mechanical part of the motor due to the PWM technique, the quantities related to the mechanical variables, namely $\mathbf{L}_{abc}$ and $\mathbf{e}_{abc}$, will be treated as constants. Thus, the electrical equation can be rewritten as:

$$\mathbf{v}_{abc}(t) = \mathbf{R}\mathbf{i}_{abc}(t) + \mathbf{L}_{abc}\frac{\mathrm{d}\mathbf{i}_{abc}(t)}{\mathrm{d}t} + \omega_e\mathbf{e}_{abc}. \quad (2.52)$$

At this point, it is convenient to continue the analysis in the Laplace domain. Quantities are represented with capital letters in the Laplace domain and small letters in the time domain. Therefore, by applying the Laplace transformation, the machine electrical equation can be

rewritten as:

$$\mathbf{V}_{abc}(s) = \mathbf{R}\mathbf{I}_{abc}(s) + \mathbf{L}_{abc}s\mathbf{I}_{abc}(s) - \mathbf{L}_{abc}\mathbf{i}_{abc}(0^-) + \frac{\omega_e \mathbf{e}_{abc}}{s}. \tag{2.53}$$

Then, isolating the term $s\mathbf{I}_{abc}$, one obtains:

$$s\mathbf{I}_{abc}(s) = \mathbf{L}_{abc}^{-1}\mathbf{V}_{abc}(s) - \mathbf{R}\mathbf{L}_{abc}^{-1}\mathbf{I}_{abc}(s) + \mathbf{L}_{abc}^{-1}\mathbf{L}_{abc}\mathbf{i}_{abc}(0^-) - \frac{\omega_e \mathbf{L}_{abc}^{-1}\mathbf{e}_{abc}}{s}, \tag{2.54}$$

where the term $\mathbf{L}_{abc}^{-1}\mathbf{L}_{abc}$ has not been simplified at this stage for convenience. A generic impedance z is connected between the machine star-point and ground, as shown in Figure (2.9, in order to model the current i_z that is potentially flowing through it. Also, this impedance is considered to be constant. Therefore, defining $Z(s)$ as the transfer function between $I_z(s)$ and $V_{NO}(s)$, the following equation holds:

$$V_{NO}(s) = Z(s)I_z(s). \tag{2.55}$$

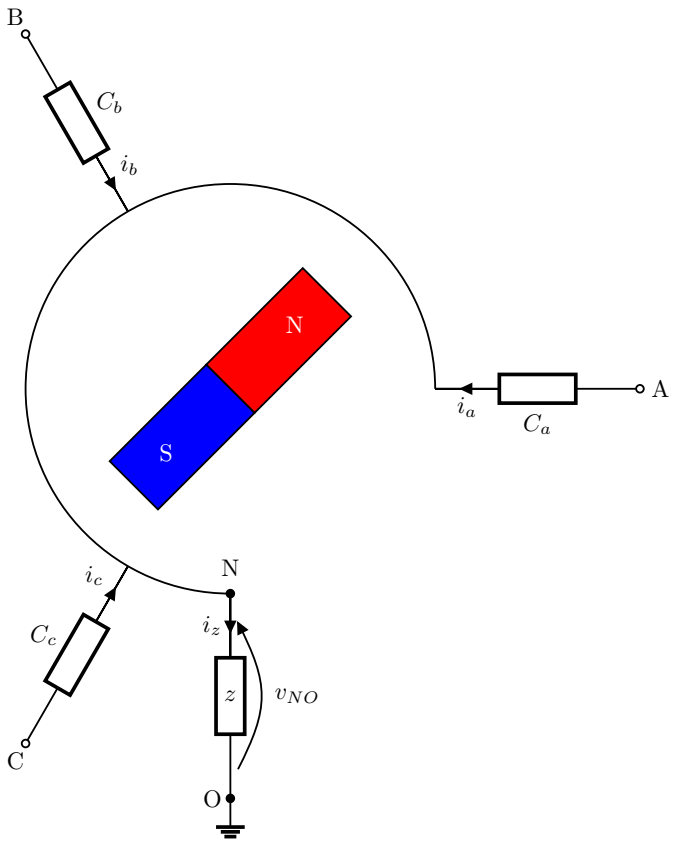

Figure 2.9: Schematic drawing of a synchronous machine with star-point impedance z connected to ground.

Also, according to Kirchhoff laws, the following equations can be posed:

$$\sum_{k=a,b,c} i_k = i_z, \sum_{k=a,b,c} \frac{\mathrm{d}}{\mathrm{d}t} i_k = \frac{\mathrm{d}}{\mathrm{d}t} i_z, \tag{2.56}$$

leading to:

$$\sum_{k=a,b,c} I_k(s) = I_z(s), \sum_{k=a,b,c} sI_k(s) = sI_z(s). \tag{2.57}$$

At this point, the following row vector is introduced:

$$\mathbf{T} = \begin{bmatrix} 1 & 1 & 1 \end{bmatrix}. \tag{2.58}$$

Multiplying equation (2.54) on the left by the vector $\mathbf{T}$ leads to:

$$s\mathbf{T}\mathbf{I}_{abc}(s) = \mathbf{T}\mathbf{L}_{abc}^{-1}\mathbf{V}_{abc}(s) - \mathbf{R}\mathbf{T}\mathbf{L}_{abc}^{-1}\mathbf{I}_{abc}(s) + \mathbf{T}\mathbf{L}_{abc}^{-1}\mathbf{L}_{abc}\mathbf{i}_{abc}(0^-) - \omega_e\mathbf{T}\mathbf{L}_{abc}^{-1}\frac{\mathbf{e}_{abc}}{s}. \tag{2.59}$$

Noting that equation (2.57) can be expressed also as:

$$s\mathbf{T}\mathbf{I}_{abc} = sI_z(s), \tag{2.60}$$

it is possible to rewrite the previous equation as:

$$sI_z = s\frac{V_{NO}}{Z(s)} = \mathbf{T}\mathbf{L}_{abc}^{-1}\mathbf{V}_{abc}(s) - \mathbf{R}\mathbf{T}\mathbf{L}_{abc}^{-1}\mathbf{I}_{abc}(s) + \mathbf{T}\mathbf{L}_{abc}^{-1}\mathbf{L}_{abc}\mathbf{i}_{abc}(0^-) - \omega_e\mathbf{T}\mathbf{L}_{abc}^{-1}\frac{\mathbf{e}_{abc}}{s}. \tag{2.61}$$

Let us express the inverse of $\mathbf{L}_{abc}$ in terms of its adjoint matrix $\mathbf{L}_{abc}^{*}$ and its determinant, as:

$$\mathbf{L}_{abc}^{-1} = \frac{\mathbf{L}_{abc}^{*}}{|\mathbf{L}_{abc}|}. \tag{2.62}$$

Thus, by substituting equation (2.62) in (2.61) and multiplying it by $|\mathbf{L}_{abc}|$, one obtains:

$$s\frac{|\mathbf{L}_{abc}|V_{NO}}{Z(s)} = \mathbf{T}\mathbf{L}_{abc}^{*}\mathbf{V}_{abc}(s) - \mathbf{R}\mathbf{T}\mathbf{L}_{abc}^{*}\mathbf{I}_{abc}(s) + \mathbf{T}\mathbf{L}_{abc}^{*}\mathbf{L}_{abc}\mathbf{i}_{abc}(0^-) - \omega_e\mathbf{T}\mathbf{L}_{abc}^{*}\frac{\mathbf{e}_{abc}}{s}. \tag{2.63}$$

It is now possible to introduce the row vector $\mathbf{L}_{\Sigma_{abc}}$ defined as:

$$\mathbf{L}_{\Sigma_{abc}} = \mathbf{T}\mathbf{L}_{abc}^{*} = \begin{bmatrix} L_{\Sigma_1} & L_{\Sigma_2} & L_{\Sigma_3} \end{bmatrix}, \tag{2.64}$$

where each i^{th} element represents the sum of the elements of the i^{th} column of the adjoint matrix associated to $\mathbf{L}_{abc}$. Thus, equation (2.63) can be written as:

$$s\frac{|\mathbf{L}_{abc}|V_{NO}(s)}{Z(s)} = \mathbf{L}_{\Sigma_{abc}}\mathbf{V}_{abc}(s) - \mathbf{R}\mathbf{L}_{\Sigma_{abc}}\mathbf{I}_{abc}(s) + \mathbf{L}_{\Sigma_{abc}}\mathbf{L}_{abc}\mathbf{i}_{abc}(0^-) - \omega_e\mathbf{L}_{\Sigma_{abc}}\frac{\mathbf{e}_{abc}}{s}. \tag{2.65}$$

The phase voltages can be expressed as the difference between terminal voltages and star-

point voltage:

$$\mathbf{v}_{abc} = \mathbf{v}_{XO} - v_{NO}\mathbf{T}^T, \tag{2.66}$$

where:

$$\mathbf{v}_{XO} = \begin{bmatrix} v_{AO} \\ v_{BO} \\ v_{CO} \end{bmatrix}. \tag{2.67}$$

Thus:

$$\mathbf{V}_{abc}(s) = \mathbf{V}_{XO}(s) - V_{NO}(s)\,\mathbf{T}^T. \tag{2.68}$$

Equation (2.65) can be then rearranged as:

$$s\frac{|\mathbf{L}_{abc}|\,V_{NO}(s)}{Z(s)} = \mathbf{L}_{\Sigma_{abc}}\left(\mathbf{V}_{XO}(s) - V_{NO}(s)\,\mathbf{T}^T\right) - \mathbf{R}\mathbf{L}_{\Sigma_{abc}}\mathbf{I}_{abc}(s) + \\ + \mathbf{L}_{\Sigma_{abc}}\mathbf{L}_{abc}\mathbf{i}_{abc}(0^-) - \omega_e\mathbf{L}_{\Sigma_{abc}}\frac{\mathbf{e}_{abc}}{s}, \tag{2.69}$$

and again as:

$$V_{NO}(s)\left[s\frac{|\mathbf{L}_{abc}|}{Z(s)} + \mathbf{L}_{\Sigma_{abc}}\mathbf{T}^T\right] = \mathbf{L}_{\Sigma_{abc}}\mathbf{V}_{XO}(s) - \mathbf{R}\mathbf{L}_{\Sigma_{abc}}\mathbf{I}_{abc}(s) + \\ + \mathbf{L}_{\Sigma_{abc}}\mathbf{L}_{abc}\mathbf{i}_{abc}(0^-) - \omega_e\mathbf{L}_{\Sigma_{abc}}\frac{\mathbf{e}_{abc}}{s}. \tag{2.70}$$

At this point, $\mathbf{I}_{abc}$ can be calculated from the machine equation 2.53 that can be easily manipulated in order to obtain:

$$(\mathbf{L}_{abc}s + \mathbf{R})\,\mathbf{I}_{abc}(s) = \mathbf{V}_{XO}(s) - V_{NO}(s)\,\mathbf{T}^T + \mathbf{L}_{abc}\mathbf{i}_{abc}(0^-) - \omega_e\frac{\mathbf{e}_{abc}}{s}. \tag{2.71}$$

The following quantities can be now defined:

$$\mathbf{Z}_{abc} = \mathbf{L}_{abc}s + \mathbf{R}. \tag{2.72}$$

Equation 2.71 can then be rearranged as:

$$\mathbf{I}_{abc} = \mathbf{Z}_{abc}^{-1}\mathbf{V}_{XO} - \mathbf{Z}_{abc}^{-1}V_{NO}\mathbf{T}^T + \mathbf{Z}_{abc}^{-1}\mathbf{L}_{abc}\mathbf{i}_{abc}(0^-) - \mathbf{Z}_{abc}^{-1}\omega_e\frac{\mathbf{e}_{abc}}{s}. \tag{2.73}$$

The expression $\mathbf{I}_{abc}$ from (2.73) can be inserted into equation (2.70), leading to:

$$V_{NO}\left[s\frac{|\mathbf{L}_{abc}|}{Z(s)} + \mathbf{L}_{\Sigma_{abc}}\left(\mathbf{I} - \mathbf{R}\mathbf{Z}_{abc}^{-1}\right)\mathbf{T}^T\right] = \mathbf{L}_{\Sigma_{abc}}\left(\mathbf{I} - \mathbf{R}\mathbf{Z}_{abc}^{-1}\right)\mathbf{V}_{XO} + \\ + \mathbf{L}_{\Sigma_{abc}}\left(\mathbf{I} - \mathbf{R}\mathbf{Z}_{abc}^{-1}\right)\mathbf{L}_{abc}\mathbf{i}_{abc}(0^-) - \omega_e\mathbf{L}_{\Sigma_{abc}}\left(\mathbf{I} - \mathbf{R}\mathbf{Z}_{abc}^{-1}\right)\frac{\mathbf{e}_{abc}}{s}. \tag{2.74}$$

by definition of:

$$\mathbf{M}(s) = \mathbf{I} - \mathbf{R}\mathbf{Z}_{abc}^{-1}, \tag{2.75}$$

we can rewrite the (2.74) in a compact form as:

$$V_{NO}(s)\left[s\frac{|\mathbf{Z}_{abc}||\mathbf{L}_{abc}|}{Z(s)} + \mathbf{L}_{\Sigma_{abc}}\mathbf{M}(s)\mathbf{T}^T\right] = \mathbf{L}_{\Sigma_{abc}}\mathbf{M}(s)\left(\mathbf{V}_{XO}(s) - \frac{\omega_e \mathbf{e}_{abc}}{s} + \mathbf{L}_{abc}\mathbf{i}_{abc}(0^-)\right). \tag{2.76}$$

Thus, defining:

$$s\frac{|\mathbf{Z}_{abc}||\mathbf{L}_{abc}|}{Z(s)} = Z_{star}(s) \tag{2.77}$$

as the star point impedance dynamic contribution to the v_{NO}, the following expressions can be now defined:

$$D(s) = Z_{star}(s) + \mathbf{L}_{\Sigma_{abc}}\mathbf{M}(s)\mathbf{T}^T, \tag{2.78}$$

$$\mathbf{N}(s) = \mathbf{L}_{\Sigma_{abc}}\mathbf{M}(s) = \begin{bmatrix} N_1(s) & N_2(s) & N_3(s) \end{bmatrix}. \tag{2.79}$$

Considering:

$$\mathbf{G}(s) = \frac{\mathbf{N}(s)}{D(s)} = \begin{bmatrix} \frac{N_1(s)}{D(s)} \\ \frac{N_2(s)}{D(s)} \\ \frac{N_3(s)}{D(s)} \end{bmatrix}^T = \begin{bmatrix} G_1(s) \\ G_2(s) \\ G_3(s) \end{bmatrix}^T = \begin{bmatrix} \frac{\sum_{i=1}^{3} L_{\Sigma_i} M_{1i}(s)}{Z_{star}(s) + \sum_{i=1}^{3}\sum_{j=1}^{3} L_{\Sigma_j} M_{ij}(s)} \\ \frac{\sum_{i=1}^{3} L_{\Sigma_i} M_{2i}(s)}{Z_{star}(s) + \sum_{i=1}^{3}\sum_{j=1}^{3} L_{\Sigma_j} M_{ij}(s)} \\ \frac{\sum_{i=1}^{3} L_{\Sigma_i} M_{3i}(s)}{Z_{star}(s) + \sum_{i=1}^{3}\sum_{j=1}^{3} L_{\Sigma_j} M_{ij}(s)} \end{bmatrix}^T. \tag{2.80}$$

Finally, equation (2.76) can be rewritten as:

$$V_{NO}(s) = \mathbf{G}(s)\left(\mathbf{V}_{XO}(s) - \frac{\omega_e \mathbf{e}_{abc}}{s} + \mathbf{L}_{abc}\mathbf{i}_{abc}(0^-)\right). \tag{2.81}$$

Eventually, it is clear that the star-point signal v_{NO} is the result of a the multiplication in the Laplace domain between a Multi-Input Single-Output (MISO) system with transfer functions given by $\mathbf{G}(s)$ and the terminal voltages vector, the back electromotive force (back-EMF) and the initial conditions. In the following section, the extraction process of the DFC signals is provided.

2.3.2 Extraction of the DFC signals

The Direct Flux Control technique allows obtaining information about the inductances of the machine phases by measuring the difference between the star-point of the machine, v_{NO} and the voltage of a virtual star-point v_{VO} (see Figure 2.10) during the transition between two excitation states.

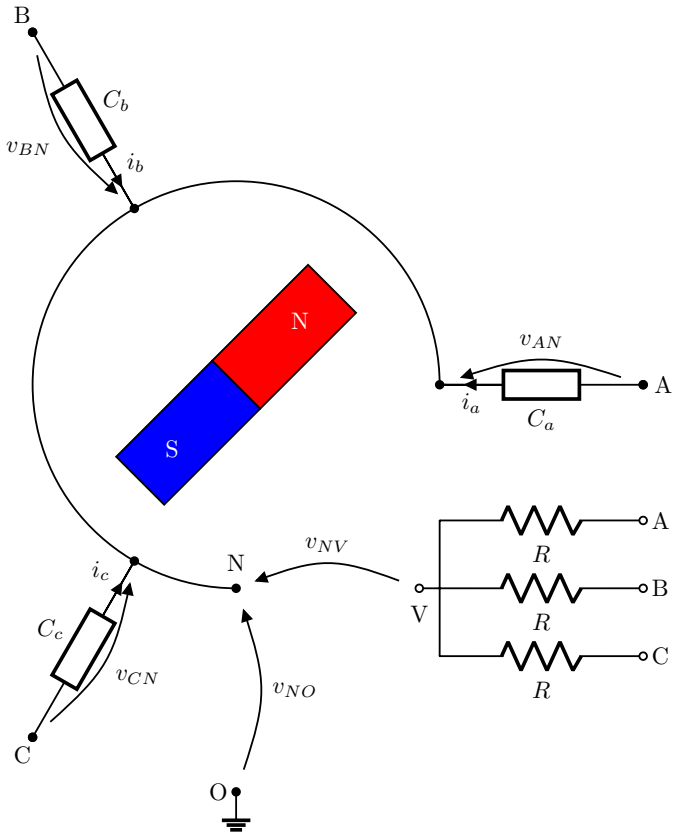

Figure 2.10: The four states of excitation of a synchronous machine where $X, Y, Z \in \{A, B, C\}$.

Let us recall the four machine excitation states in Figure 2.5, where X, Y, Z can be any combination of the phases A, B, C. Obviously, we can state that:

for state I :

$$v_{XO}(t) = 0, \quad v_{YO}(t) = 0, \quad v_{ZO}(t) = 0 \implies \mathbf{V}_{XO}(s) = \begin{bmatrix} 0 \\ 0 \\ 0 \end{bmatrix} \tag{2.82}$$

for state II :

$$v_{XO}(t) = v_{DC}, \quad v_{YO}(t) = 0, \quad v_{ZO}(t) = 0 \implies \mathbf{V}_{XO}(s) = \begin{bmatrix} \frac{v_{DC}}{s} \\ 0 \\ 0 \end{bmatrix} \tag{2.83}$$

for state III :

$$v_{XO}(t) = v_{DC}, \quad v_{YO}(t) = v_{DC}, \quad v_{ZO}(t) = 0 \implies \mathbf{V}_{XO}(s) = \begin{bmatrix} \frac{v_{DC}}{s} \\ \frac{v_{DC}}{s} \\ 0 \end{bmatrix} \tag{2.84}$$

for state IV :

$$v_{XO}(t) = v_{DC}, \quad v_{YO}(t) = v_{DC}, \quad v_{ZO}(t) = v_{DC} \implies \mathbf{V}_{XO}(s) = \begin{bmatrix} \frac{v_{DC}}{s} \\ \frac{v_{DC}}{s} \\ \frac{v_{DC}}{s} \end{bmatrix} \tag{2.85}$$

and the virtual star-point voltage v_{VO} can be expressed as:

$$v_{VO} = \frac{1}{3}\mathbf{T}\mathbf{v}_{XO}. \tag{2.86}$$

Let us now recall equation (2.81) where, for simplicity, the initial conditions are neglected and the considerations made in equations (2.82),(2.83),(2.84) and (2.85) are taken into account:

$$V_{NO}(s) = \mathbf{G}(s)\left(\mathbf{V}_{XO}(s) - \frac{\omega_e \mathbf{e}_{abc}}{s}\right). \tag{2.87}$$

It can be proven, as shown in [52], that the transfer function $\mathbf{G}(s)$ is biproper, thus, the $\mathbf{G}(s)$ can be divided into two term: a constant gain $\mathbf{G}_c$ and a strictly proper function $\mathbf{R}(s)$:

$$\mathbf{G}(s) = \mathbf{G}_c + \mathbf{R}(s). \tag{2.88}$$

It has to be remarked that a strictly proper transfer function will approach zero as the frequency approaches infinity: $\lim_{s\to j\infty} \mathbf{R}(j\infty) = 0$. Hence:

$$\lim_{s\to j\infty} \mathbf{G}(s) = \lim_{s\to j\infty} (\mathbf{G}_c + \mathbf{R}(s)) = \mathbf{G}_c. \tag{2.89}$$

The value of $\mathbf{G}_c$ can be found easily considering that $\mathbf{M}(j\infty) = \mathbf{I}$:

$$\mathbf{G}_c = \lim_{s\to j\infty} \mathbf{G}(s) = \frac{\mathbf{L}_{\Sigma_{abc}}\mathbf{M}(j\infty)}{\mathbf{L}_{\Sigma_{abc}}\mathbf{M}(j\infty)\mathbf{T}^T} = \frac{\mathbf{L}_{\Sigma_{abc}}\mathbf{M}(j\infty)}{\mathbf{L}_{\Sigma_{abc}}\mathbf{T}^T} = \frac{\mathbf{L}_{\Sigma_{abc}}}{\mathbf{L}_{\Sigma_{abc}}\mathbf{T}^T}, \tag{2.90}$$

The value of the star-point voltage v_{NO} can be found by applying the Laplace antitransform:

$$\begin{aligned} v_{NO}(t) = {} & \mathscr{L}^{-1}\left[\mathbf{G}(s)\left(\mathbf{V}_{XO}(s) - \frac{\omega_e \mathbf{e}_{abc}}{s}\right)\right] = \\ & = \mathscr{L}^{-1}\left[\mathbf{G}(s)\mathbf{V}_{XO}(s)\right] - \mathscr{L}^{-1}\left[\mathbf{G}(s)\frac{\omega_e \mathbf{e}_{abc}}{s}\right] = v^v_{NO}(t) - v^e_{NO}(t). \end{aligned} \tag{2.91}$$

It is clear from the previous equation that the evolution of the $v^e_{NO}(t)$ is not dependent on the switching of the state excitation. Hence, considering t_1 as the time in which the state excitation switching occurs, two measurements of the star-point voltage v_{NO} are taken respectively at t_1^- and t_1^+ and subtracted in order to eliminate the $v^e_{NO}(t)$ term:

$$v_{NO}(t_1^+) - v_{NO}(t_1^-) = v^v_{NO}(t_1^+) + v^e_{NO}(t_1^+) - v^v_{NO}(t_1^-) - v^e_{NO}(t_1^-) = v^v_{NO}(t_1^+) - v^v_{NO}(t_1^-), \tag{2.92}$$

since $v^e_{NO}\left(t_1^+\right) = v^e_{NO}\left(t_1^-\right)$. If we consider the evolution of $v^v_{NO}(t)$ starting from $t = t_1$ we can state that:

$$v^v_{NO}(t-t_1) = \mathscr{L}^{-1}\left[\mathbf{G}(s)\mathbf{V}^+_{XO}(s)\right] = \mathscr{L}^{-1}\left[\left(\mathbf{G}_c + \mathbf{R}(s)\right)\mathbf{V}^+_{XO}(s)\right] = \\ = \mathbf{G}_c\mathbf{v}_{XO}(t_1^+) + \mathscr{L}^{-1}\left[\mathbf{R}(s)\mathbf{V}^+_{XO}(s)\right], \quad (2.93)$$

and

$$v^v_{NO}(-t-t_1) = \mathscr{L}^{-1}\left[\mathbf{G}(s)\mathbf{V}^-_{XO}(s)\right] = \mathscr{L}^{-1}\left[\left(\mathbf{G}_c + \mathbf{R}(s)\right)\mathbf{V}^-_{XO}(s)\right] = \\ = \mathbf{G}_c\mathbf{v}_{XO}(t_1^-) + \mathscr{L}^{-1}\left[\mathbf{R}(s)\mathbf{V}^-_{XO}(s)\right], \quad (2.94)$$

where $\mathbf{V}^+_{XO}(s)$ is the Laplace transform of $\mathbf{v}_{XO}\left(t-t_1^+\right)$ and $\mathbf{V}^-_{XO}(s)$ is the Laplace transform of $\mathbf{v}_{XO}\left(-t-t_1^-\right)$. Considering that $\mathbf{R}(s)$ is strictly proper, the application of a step function input to $\mathbf{R}(s)$ does not generate a discontinuity to the output, thus we can consider at t_1 the results of the antitransform $\mathscr{L}^{-1}\left[\mathbf{R}(s)\mathbf{V}^+_{XO}(s)\right]$ and $\mathscr{L}^{-1}\left[\mathbf{R}(s)\mathbf{V}^-_{XO}(s)\right]$ equal. We obtain:

$$v^v_{NO}(t_1^+) - v^v_{NO}(t_1^-) = \\ = \mathbf{G}_c\mathbf{v}_{XO}(t_1^+) + \mathscr{L}^{-1}\left[\mathbf{R}(s)\mathbf{V}^+_{XO}(s)\right] - \mathbf{G}_c\mathbf{v}_{XO}(t_1^-) - \mathscr{L}^{-1}\left[\mathbf{R}(s)\mathbf{V}^-_{XO}(s)\right] = \\ = \mathbf{G}_c\left(\mathbf{v}_{XO}(t_1^+) - \mathbf{v}_{XO}(t_1^-)\right) = \frac{\mathbf{L}_{\Sigma_{abc}}}{\mathbf{L}_{\Sigma_{abc}}\mathbf{T}^T}\left(\mathbf{v}_{XO}(t_1^+) - \mathbf{v}_{XO}(t_1^-)\right). \quad (2.95)$$

We can now define the virtual star-point voltage equation:

$$v_{NV}(t) = v_{NO}(t) - v_{VO}(t) = v_{NO}(t) - \frac{1}{3}\mathbf{T}\mathbf{v}_{XO}(t). \quad (2.96)$$

The difference between two consecutive measurement of v_{NV} at t_1^+ and t_1^- when the states are switching is considered:

$$v_{NV}(t_1^+) - v_{NV}(t_1^-) = \left(\frac{\mathbf{L}_{\Sigma_{abc}}}{\mathbf{L}_{\Sigma_{abc}}\mathbf{T}^T} - \frac{1}{3}\mathbf{T}\right)\left(\mathbf{v}_{XO}(t_1^+) - \mathbf{v}_{XO}(t_1^-)\right). \quad (2.97)$$

Considering that:

between state I and II:

$$\underbrace{\mathbf{v}_{XO}(t_1^+)}_{\text{state II}} - \underbrace{\mathbf{v}_{XO}(t_1^-)}_{\text{state I}} = \begin{bmatrix} v_{DC} \\ 0 \\ 0 \end{bmatrix}, \quad (2.98)$$

between state II and III:

$$\underbrace{\mathbf{v}_{XO}(t_1^+)}_{\text{state III}} - \underbrace{\mathbf{v}_{XO}(t_1^-)}_{\text{state II}} = \begin{bmatrix} 0 \\ v_{DC} \\ 0 \end{bmatrix}, \quad (2.99)$$

between state III and IV:

$$\underbrace{\mathbf{v}_{XO}\left(t_1^+\right)}_{\text{state IV}} - \underbrace{\mathbf{v}_{XO}\left(t_1^-\right)}_{\text{state III}} = \begin{bmatrix} 0 \\ 0 \\ v_{DC} \end{bmatrix}, \tag{2.100}$$

we can define the DFC signal vector $\Gamma_{abc} = [\Gamma_a \quad \Gamma_b \quad \Gamma_c]^T$ as:

$$\begin{aligned}
\Gamma_a &= \underbrace{v_{NV}\left(t_1^+\right)}_{\text{state II}} - \underbrace{v_{NV}\left(t_1^-\right)}_{\text{state I}} = \left(\frac{\mathbf{L}_{\Sigma_{abc}}}{\mathbf{L}_{\Sigma_{abc}}\mathbf{T}^T} - \frac{1}{3}\mathbf{T}\right)\begin{bmatrix} v_{DC} \\ 0 \\ 0 \end{bmatrix} = \left(\frac{L_{\Sigma_1}}{\mathbf{L}_{\Sigma_{abc}}\mathbf{T}^T} - \frac{1}{3}\right)v_{DC}, \\
\Gamma_b &= \underbrace{v_{NV}\left(t_1^+\right)}_{\text{state III}} - \underbrace{v_{NV}\left(t_1^-\right)}_{\text{state II}} = \left(\frac{\mathbf{L}_{\Sigma_{abc}}}{\mathbf{L}_{\Sigma_{abc}}\mathbf{T}^T} - \frac{1}{3}\mathbf{T}\right)\begin{bmatrix} 0 \\ v_{DC} \\ 0 \end{bmatrix} = \left(\frac{L_{\Sigma_2}}{\mathbf{L}_{\Sigma_{abc}}\mathbf{T}^T} - \frac{1}{3}\right)v_{DC}, \\
\Gamma_c &= \underbrace{v_{NV}\left(t_1^+\right)}_{\text{state IV}} - \underbrace{v_{NV}\left(t_1^-\right)}_{\text{state III}} = \left(\frac{\mathbf{L}_{\Sigma_{abc}}}{\mathbf{L}_{\Sigma_{abc}}\mathbf{T}^T} - \frac{1}{3}\mathbf{T}\right)\begin{bmatrix} 0 \\ 0 \\ v_{DC} \end{bmatrix} = \left(\frac{L_{\Sigma_3}}{\mathbf{L}_{\Sigma_{abc}}\mathbf{T}^T} - \frac{1}{3}\right)v_{DC}.
\end{aligned} \tag{2.101}$$

Considering these equations and the previously mentioned edge-aligned application of the PWM signal it is clear that a modification of the PWM pattern is necessary in order to obtain a meaningful measurement of the DFC signals. The idea is to modify directly the edge-aligned pattern in order to exploit only the machine excitation states I and II. The edge-aligned pattern application in case $\mathbf{v}_1$ and $\mathbf{v}_2$ are considered can be represented as follows:

$$\mathbf{v}_7 \quad \rightarrow \quad \mathbf{v}_2 \quad \rightarrow \quad \mathbf{v}_1 \quad \rightarrow \quad \mathbf{v}_0$$

In order to introduce a modification to this PWM pattern suitable for DFC measurements in excitation states I and II, two vectors are introduced for a very short time at the beginning of the PWM period T_{PWM}:

$$\underbrace{\mathbf{v}_0 \quad \rightarrow \quad \mathbf{v}_X}_{\text{DFC measurement}} \quad \rightarrow \quad \underbrace{\mathbf{v}_7 \quad \rightarrow \quad \mathbf{v}_2 \quad \rightarrow \quad \mathbf{v}_1 \quad \rightarrow \quad \mathbf{v}_0}_{\text{edge-aligned PWM pattern}},$$

where $\mathbf{v}_X \in \{\mathbf{v}_1, \mathbf{v}_3, \mathbf{v}_5\}$. Following, a short list relating the applied voltage vectors and the retrieved quantity is shown:

$$\begin{aligned}
\mathbf{v}_1 &\rightarrow \left(\frac{L_{\Sigma_1}}{\mathbf{L}_{\Sigma_{abc}}\mathbf{T}^T} - \frac{1}{3}\right)v_{DC} = \left(\frac{L_{\Sigma_2} + L_{\Sigma_3}}{L_{\Sigma_1} + L_{\Sigma_2} + L_{\Sigma_3}}\right)v_{DC}, \\
\mathbf{v}_3 &\rightarrow \left(\frac{L_{\Sigma_2}}{\mathbf{L}_{\Sigma_{abc}}\mathbf{T}^T} - \frac{1}{3}\right)v_{DC} = \left(\frac{L_{\Sigma_1} + L_{\Sigma_3}}{L_{\Sigma_1} + L_{\Sigma_2} + L_{\Sigma_3}}\right)v_{DC}, \\
\mathbf{v}_5 &\rightarrow \left(\frac{L_{\Sigma_3}}{\mathbf{L}_{\Sigma_{abc}}\mathbf{T}^T} - \frac{1}{3}\right)v_{DC} = \left(\frac{L_{\Sigma_1} + L_{\Sigma_2}}{L_{\Sigma_1} + L_{\Sigma_2} + L_{\Sigma_3}}\right)v_{DC}.
\end{aligned} \tag{2.102}$$

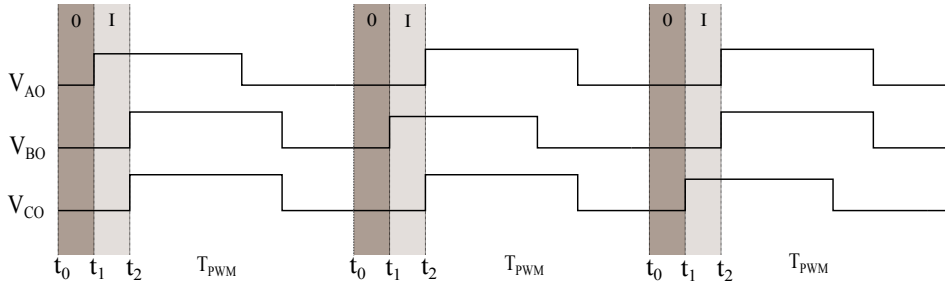

Figure 2.11: Modified edge-aligned PWM pattern used for measurement of the v_{NV} voltage.

Figure 2.11 shows the discussed modified edge-aligned PWM pattern. The first measurement is taken at t_1^- that it is located between t_0 and t_1, the second measurement at $t_1 + \Delta_t$ located between t_1 and t_2.
Within the next section, the relation between the DFC signals and the rotor angular position will be presented considering a generic definition of the inductance matrix.

3 Position Estimation with the Direct Flux Control

As shown in the previous section, the application of a modified PWM pattern at the motor voltage terminals and the measurement of the star-point voltage allow the extraction of the DFC signals. The star-point voltage behavior is determined by a MISO type transfer function dependent on the machine electrical parameters, potentially including the circuit elements needed for the voltage measurement of the star-point. Since the numerator and the denominator of the transfer function have the same degree, namely the same number of poles and zeros, a static relation between star-point and phase voltages can be identified. This relation is dependent on the values of the vector $\mathbf{L}_{\Sigma_{abc}}$ which contains the information about the rotor position. By the measurement of two consecutive star-point voltages and subtracting them, the DFC signals are obtained in the form presented in equation (2.101). Taking into account the previous considerations, this chapter aims at defining the main algorithms used for the extraction of the angular position starting from the DFC signals as well as presenting the potential limitations of this sensorless technique. The effect of position estimation error over the machine equations and then over the FOC are considered and presented. Eventually, a new algorithm for the improvement of the position estimation will be presented. This algorithm, called Iterative Vector Decoupling (IVD), is based on an iteration process that aims at eliminating the systematic error carried by the DFC signals.

3.1 DFC position estimation algorithms

Two main approaches can be considered in order to estimate the angular position from the DFC signals: the standard and the inverse DFC method. Before their description, a relation between angular position and inductance matrix $\mathbf{L}_{abc}$ has to be given. Let us consider the relation presented in equation (2.31). If the matrix $\mathbf{L}_{\Sigma_{abc}}$ is calculated we obtain:

$$\mathbf{L}_{\Sigma_{abc}} = \mathbf{T}\mathbf{L}^{*}_{abc}. \tag{3.1}$$

Since the adjoint matrix $\mathbf{L}^{*}_{abc}$ has every of its entries equal to zero, we get:

$$\mathbf{L}_{\Sigma_{abc}} = \begin{bmatrix} 0 & 0 & 0 \end{bmatrix}. \tag{3.2}$$

Hence, for this particular definition of the inductance matrix the DFC signal vector $\mathbf{\Gamma}_{abc}$ does not carry any information. Although the matrix definition in equation (2.31) is commonly considered for control purpose due to its simplicity, it is not suitable for the description of the DFC signal model. Thus, let us introduce a more generic definition of the inductance matrix:

$$\mathbf{L}_{abc} = \begin{bmatrix} L_0 + L_2\cos(2\theta_e) & M_0 + M_2\cos\left(2\theta_e - \frac{2\pi}{3}\right) & M_0 + M_2\cos\left(2\theta_e + \frac{2\pi}{3}\right) \\ M_0 + M_2\cos\left(2\theta_e - \frac{2\pi}{3}\right) & L_0 + L_2\cos\left(2\theta_e + \frac{2\pi}{3}\right) & M_0 + M_2\cos(2\theta_e) \\ M_0 + M_2\cos\left(2\theta_e + \frac{2\pi}{3}\right) & M_0 + M_2\cos(2\theta_e) & L_0 + L_2\cos\left(2\theta_e + \frac{4\pi}{3}\right) \end{bmatrix}, \quad (3.3)$$

where the terms M_0 and M_2 model the mutual inductance between the phases considering the effect on the magnetic field caused by the permanent magnet. After some algebraic calculation, the $\mathbf{L}_{\Sigma_{abc}}$ can be now defined as:

$$\mathbf{L}^*_{\Sigma_{abc}} = \begin{bmatrix} a_1\cos(2\theta_e) + & a_3\cos(4\theta_e) + & a_5 \\ b_1\cos(2\theta_e) + b_2\sin(2\theta_e) + & b_3\cos(4\theta_e) + b_4\sin(4\theta_e) + & b_5 \\ c_1\cos(2\theta_e) + c_2\sin(2\theta_e) + & c_3\cos(4\theta_e) + c_4\sin(4\theta_e) + & c_5 \end{bmatrix}^T, \quad (3.4)$$

where:

$$\begin{aligned} a_1 &= L_0M_2 - L_0L_2 + L_2M_0 - M_0M_2, \\ a_3 &= -\frac{L_2^2}{2} - \frac{L_2M_2}{2} - M_2^2, \\ a_5 &= L_0^2 - 2L_0M_0 + M_0^2 - \frac{L_2^2}{4} - L_2M_2 - 3M_2, \\ b_1 &= c_1 = \frac{a_1}{2} - L_2M_0 + M_0M_2, \\ b_2 &= -c_2 = \frac{\sqrt{3}}{2}b_1, \\ b_3 &= c_3 = \frac{a_3}{2} + M_2^2, \\ b_4 &= -c_4 = -\frac{\sqrt{3}}{2}b_3, \\ b_5 &= c_5 = a_5 + 2M_2^2. \end{aligned} \quad (3.5)$$

The expression of the vector $\mathbf{L}^*_{\Sigma_{abc}}$ presented in equation (3.4) shows the relation between its values and the rotor position θ_e. It is clear from equation (3.5) that by adding and subtracting properly the vector elements the cosine and sine dependent terms can be isolated.

3.1.1 Standard DFC algorithm

Considering the relation between the $\mathbf{L}^*_{\Sigma_{abc}}$ and the DFC signals $\mathbf{\Gamma}_{abc}$ presented in equation (2.101) and applying the Clarke transformation to the $\mathbf{\Gamma}_{abc}$, one obtains:

$$\mathbf{\Gamma}_{\alpha\beta\gamma} = T_C\mathbf{\Gamma}_{abc} = \begin{bmatrix} \Gamma_\alpha \\ \Gamma_\beta \\ \Gamma_\gamma \end{bmatrix} = \begin{bmatrix} -a\cos(2\theta_e) + b\cos(4\theta_e) \\ a\sin(2\theta_e) + b\sin(4\theta_e) \\ 0 \end{bmatrix} = \begin{bmatrix} -a\cos(2\omega_e t) + b\cos(4\omega_e t) \\ a\sin(2\omega_e t) + b\sin(4\omega_e t) \\ 0 \end{bmatrix}, \quad (3.6)$$

where:

$$\begin{aligned} a &= (L_0 - M_0) \cdot \frac{L_2 - M_2}{3\left[(L_0 - M_0)^2 - \left(\frac{L_2}{2} + M_2\right)^2\right]}, \\ b &= \left(\frac{L_2}{2} + M_2\right) \cdot \frac{L_2 - M_2}{3\left[(L_0 - M_0)^2 - \left(\frac{L_2}{2} + M_2\right)^2\right]}, \\ \omega_e t &= \theta_e. \end{aligned} \tag{3.7}$$

Starting from the previous equation, we can define the conditions for which the DFC signals carry information about the rotor position:

- first condition : $L_2 - M_2 \neq 0$,
- second condition: $L_0 - M_0 \neq \frac{L_2}{2} + M_2$.

It is noticeable that if $a \gg b$ the angular position can be estimated simply using the full quadrant arc tangent function:

$$\chi = -\operatorname{atan2}\left(\Gamma_\alpha, \Gamma_\beta\right) \approx -\operatorname{atan2}\left(-a\cos\left(2\theta_e\right), a\sin\left(2\theta_e\right)\right) = 2\theta_e, \tag{3.8}$$

defining $\operatorname{atan2}(\cdot,\cdot)$ as:

$$\operatorname{atan2}(x,y) = \begin{array}{l} \arctan\left(\frac{y}{x}\right) \text{ if } x \text{ and } y \geq 0, \\ \arctan\left(\frac{y}{x}\right) + 90^\circ \text{ if } x < 0 \text{ and } y \geq 0, \\ \arctan\left(\frac{y}{x}\right) + 180^\circ \text{ if } x \text{ and } y < 0, \\ \arctan\left(\frac{y}{x}\right) + 360^\circ \text{ if } x \geq 0 \text{ and } y < 0. \end{array} \tag{3.9}$$

From now on, for sake of readability, we will consider $\operatorname{atan2}(x,y) = \operatorname{atan}\left(\frac{y}{x}\right)$. Then, we can define the estimated rotor position $\hat{\theta}_e$ as:

$$\hat{\theta}_e = \frac{\chi}{2}. \tag{3.10}$$

Let us now consider the vector $\mathbf{\Gamma}^*_{\alpha\beta}$ (avoiding the third component Γ_γ) on a complex plane as a vector with the following normalized components:

$$\Gamma^*_{\alpha\beta} = \frac{\Gamma_\alpha}{a} + j\frac{\Gamma_\beta}{a} = -\cos\left(2\theta_e\right) + p\cos\left(4\theta_e\right) + j\left(\sin\left(2\theta_e\right) + p\sin\left(4\theta_e\right)\right), \tag{3.11}$$

where p is defined as the ratio between b and a. Then, the parameter p introduces a fourth harmonic term on the DFC signals. It is clear that the presence of this additional harmonic will result into a systematic error on the position estimation. Reminding that:

$$x + jy = \sqrt{x^2 + y^2}e^{j\theta}, \quad \theta = \angle\left(\frac{y}{x}\right) = \operatorname{atan}\left(\frac{y}{x}\right), \tag{3.12}$$

the estimation error can be defined as follows:

$$\begin{aligned}
\chi &= -\operatorname{atan}\left(\frac{\Gamma_\beta}{\Gamma_\alpha}\right) \\
&= -\operatorname{atan}\left(\frac{a\sin(2\theta_e)+b\sin(4\theta_e)}{-a\cos(2\theta_e)+b\cos(4\theta_e)}\right) \\
&= \operatorname{atan}\left(\frac{a\sin(2\theta_e)+b\sin(4\theta_e)}{a\cos(2\theta_e)-b\cos(4\theta_e)}\right) \\
&= \angle\left(ae^{j2\theta_e}-be^{-j4\theta_e}\right) \\
&= \angle\left(ae^{j2\theta_e}\left(1-\frac{b}{a}e^{-j6\theta_e}\right)\right) \\
&= 2\theta_e+\angle\left(1-\frac{b}{a}e^{-j6\theta_e}\right) \\
&= 2\theta_e+\operatorname{atan}\left(\frac{p\sin(6\theta_e)}{1-p\cos(6\theta_e)}\right).
\end{aligned} \tag{3.13}$$

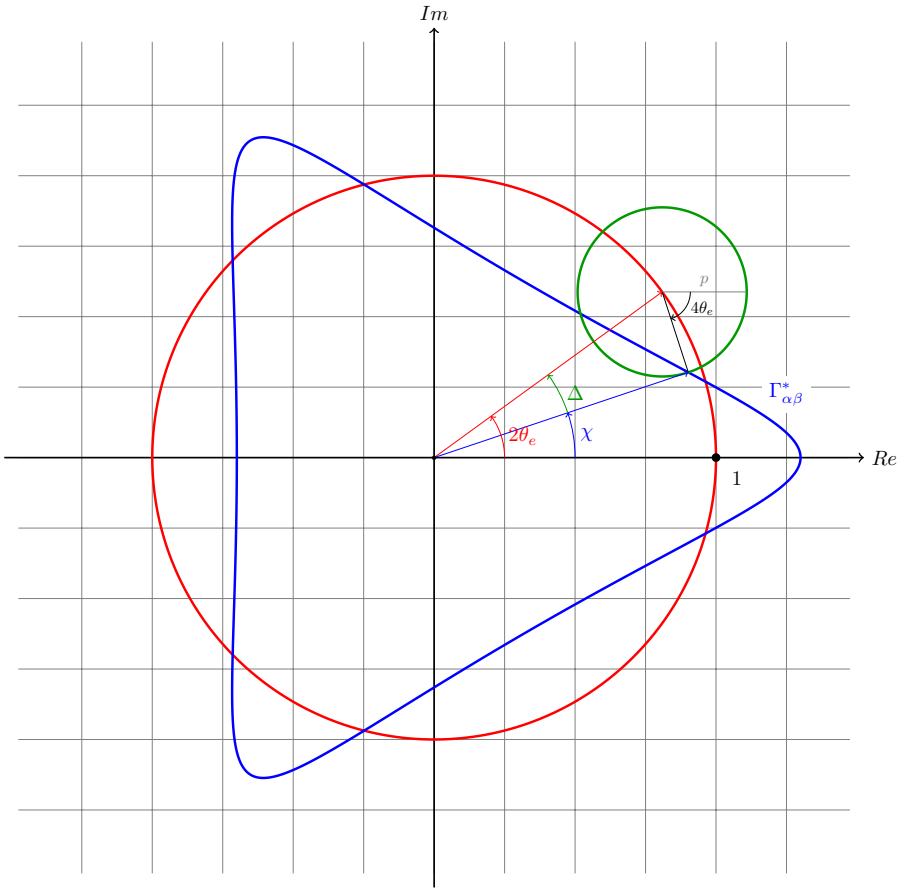

Figure 3.1: The vector $\cos(2\theta_e)+j\sin(2\theta_e)$ is depicted with a red line, the vector $\mathbf{\Gamma}^*_{\alpha\beta}$ is depicted with a blue line. The estimation error is depicted with the green line.

Eventually, we can write:

$$\chi = 2\theta_e + \Delta, \tag{3.14}$$

where $\Delta = \operatorname{atan}\left(\frac{p\sin(6\theta_e)}{1-p\cos(6\theta_e)}\right)$ is the estimation error. Its determination can be also proven geometrically as shown in Figure 3.1. The standard DFC algorithm can be summarized using the following Flowchart 3.2

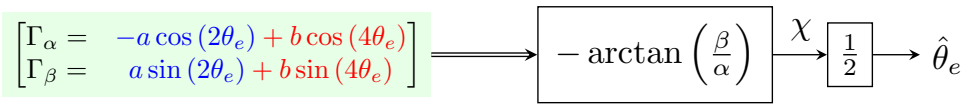

Figure 3.2: Flowchart of the DFC position extraction operations

3.1.2 Inverse DFC algorithm

A different method for extracting the electrical rotor position, that can perform very well for a broader range of machines has been firstly proposed in [53]. This method is based on the direct measurement of the star-point voltage v_{NO} instead of the v_{NV} referenced to the virtual star-point. This permits the definition of a new measurement vector $\boldsymbol{\kappa}_{abc}$:

$$\boldsymbol{\kappa}_{abc} = \begin{bmatrix}\kappa_a\\ \kappa_b\\ \kappa_c\end{bmatrix} = \begin{bmatrix}\frac{\mathbf{L}_{\Sigma_{abc}}\mathbf{T}^T}{L_{\Sigma_1}}\\ \frac{\mathbf{L}_{\Sigma_{abc}}\mathbf{T}^T}{L_{\Sigma_2}}\\ \frac{\mathbf{L}_{\Sigma_{abc}}\mathbf{T}^T}{L_{\Sigma_3}}\end{bmatrix} = \begin{bmatrix}\frac{L_{\Sigma_1}+L_{\Sigma_2}+L_{\Sigma_3}}{L_{\Sigma_1}}\\ \frac{L_{\Sigma_1}+L_{\Sigma_2}+L_{\Sigma_3}}{L_{\Sigma_2}}\\ \frac{L_{\Sigma_1}+L_{\Sigma_2}+L_{\Sigma_3}}{L_{\Sigma_3}}\end{bmatrix}, \tag{3.15}$$

that is indeed the reciprocal value of the measurement vector obtained considering the voltage v_{NO}. The $\boldsymbol{\kappa}_{abc}$ is also transformed using the Clarke matrix and the new vector can be considered for the estimation of the position:

$$\chi_{inv} = \operatorname{atan}\left(\frac{\kappa_\beta}{\kappa_\alpha}\right) \approx 2\theta_e. \tag{3.16}$$

It is more difficult to find an analytical expression for the position estimation error of χ_{inv} respect to the standard approach. However, a comparison between these two methods can be given using a numerical analysis, as shown in Figure 3.3. Although the inverse algorithm is more simple to be implemented, the resulting estimated position could be worse than in case of the standard algorithm depending on the motor parameters. An example in which the inverse approach gives a perfect position estimation is when the machine has a diagonal phase inductance matrix, hence, $M_0 = M_2 = 0$.

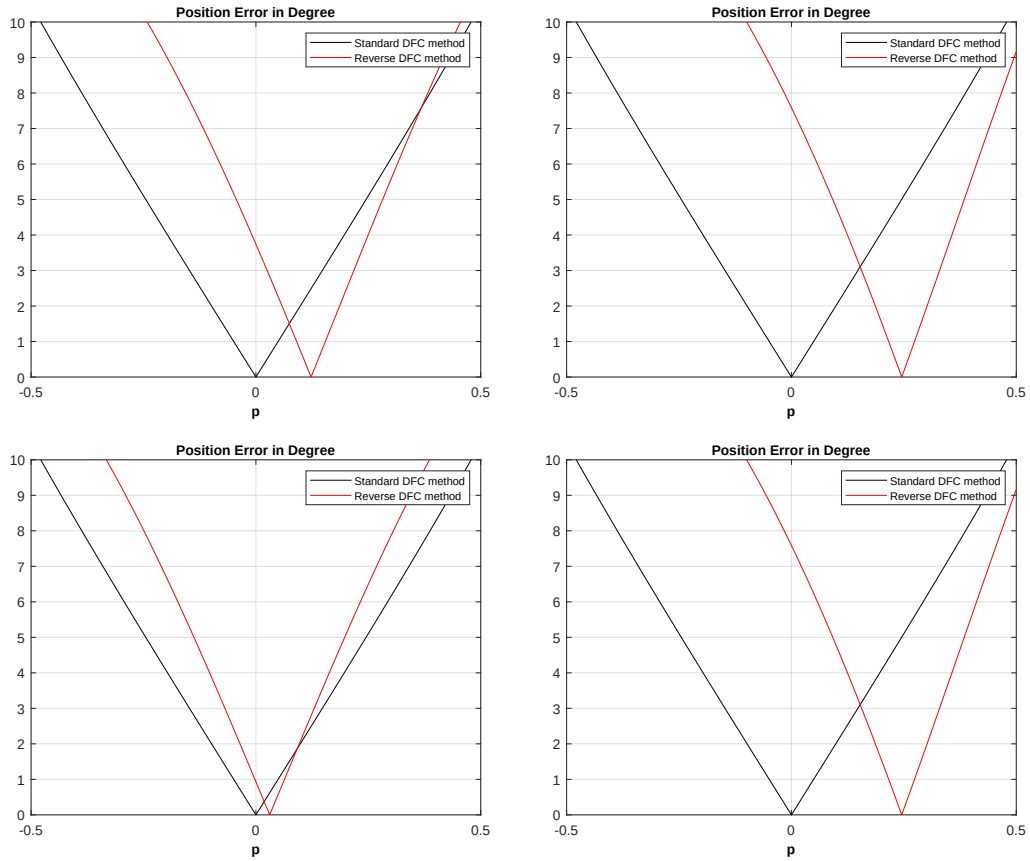

Figure 3.3: Comparison of the position errors of the presented methods. The plot is referred to a machine with the following inductance values: L_0 = 442.2 mH, M_0 = 20.7 mH, L_2 = 103.3 mH. The parameter M_2 is let vary between $-L_0 + M_0 - L_2$ and $L_0 - M_0 - L_2$ in order to get the p range between -0.5 and 0.5. Left-above: parameters as declared. Right-above: the parameters L_0 and M_0 are doubled. Left-below: the parameters L_0 and M_0 are halved. Right-below: the parameters L_2 is halved.

3.1.3 Duality of the rotor position

As shown, both standard and inverse algorithms provide an estimation of $2\theta_e$ since the flux generated by the permanent magnet of the motor modulates the machine phase inductance regardless of the north or south magnetic pole shown. For that reason, the magnetic flux linked to a phase reaches its maximum every 180°. This effect causes the DFC technique to present an uncertainty of 180° on the estimated position which must be avoided in order to not invert accidentally the rotation direction of the rotor. This is actually a common issue that affects machine anisotropy based sensorless technique and many solutions have been proposed for solving this ambiguity problem in literature. The most straightforward method is to align the magnetic flux generated by the permanent magnet, i.e. the rotor direction, with one phase of the machine before its operation. For example, by applying the vector $\mathbf{v}_1$, the rotor aligns with phase a and, therefore, the rotor shows its north pole. However, for some applications, this rotation is not always possible or attractive since the potential mechanical

element attached to the motor shaft may not be allowed to move at every initialization. A valid alternative is the usage of current injection along the $d-$axis of the machine. In fact, considering the direct influence that such current has on the L_d inductance of the machine in the rotor reference frame, one is able to determine what pole the rotor exhibits. A direct way to obtain a direct influence of this inductance on the DFC measurements cannot be found. For that reason, it is possible to resort to alignment or to high-frequency injection techniques for the solution of the initial rotor position ambiguity.

3.2 Effect of the position error on the machine equations

The position estimation methods for the DFC technique have been presented within the previous section. As shown, the estimated position accuracy depends on the motor parameters, i.e. on the definition of the inductance matrix. Since the estimated position will be used for the FOC, it is understandable to ask ourselves how much the use of a possibly inaccurate knowledge of the angular position affects the drive and control of the machine. In order to investigate this aspect, a closer look to the effects of the application of Clarke and Park transformations to the system equations is needed. Hence, some results already provided in section 2.2.1 and 2.2.2 will be proposed again in a form suitable for this purpose. Let us consider the symmetric inductance matrix for a three-phase PMSM as defined as in equation (3.3).

3.2.1 Further considerations on the machine equations

Let us recall the electrical machine equation defined on the three phase stator reference frame:

$$\mathbf{V}_{abc} = \mathbf{R}\mathbf{i}_{abc} + \frac{d}{dt}\left(\mathbf{L}_{abc}\mathbf{i}_{abc} + \mathbf{\Psi}_{abc}\right). \tag{3.17}$$

By developing the time derivative and applying the Clarke transformation to the previous equation, we get the $\alpha\beta\gamma$ system equation as presented in equation (2.16). Considering the current $i_\gamma = 0$ and the parasitic effects on the star-point neglectable, we can eliminate the third equation and write:

$$\mathbf{V}_{\alpha\beta} = \mathbf{R}_s\mathbf{i}_{\alpha\beta} + \frac{d\mathbf{L}_{\alpha\beta}}{dt}\mathbf{i}_{\alpha\beta} + \mathbf{L}_{\alpha\beta}\frac{d\mathbf{i}_{\alpha\beta}}{dt} + \omega_e\frac{\partial\mathbf{\Psi}_{\alpha\beta}}{\partial\theta_e}, \tag{3.18}$$

where:

$$\mathbf{L}_{\alpha\beta} = \begin{bmatrix} \gamma_0 - \gamma_2\cos(2\theta_e) & -\gamma_2\sin(2\theta_e) \\ -\gamma_2\sin(2\theta_e) & \gamma_0 + \gamma_2\cos(2\theta_e) \end{bmatrix}, \tag{3.19}$$

$$\frac{d\mathbf{L}_{\alpha\beta}}{dt} = \omega_e\frac{\partial\mathbf{L}_{\alpha\beta}}{\partial\theta_e} = 2\omega_e\begin{bmatrix} \gamma_2\sin(2\theta_e) & -\gamma_2\cos(2\theta_e) \\ -\gamma_2\cos(2\theta_e) & -\gamma_2\sin(2\theta_e) \end{bmatrix}, \tag{3.20}$$

$$\gamma_0 = L_0 - M_0, \tag{3.21}$$

$$\gamma_2 = \frac{L_2}{2} + M_2. \tag{3.22}$$

Bringing the derivative of the current with respect to time to the left-hand side of the equation, one obtains:

$$\frac{d}{dt}\mathbf{i}_{\alpha\beta} = \mathbf{L}_{\alpha\beta}^{-1}\left(-\left(\mathbf{R}_s + \omega_e\frac{\partial\mathbf{L}_{\alpha\beta}}{\partial\theta_e}\right)\mathbf{i}_{\alpha\beta} - \omega_e\mathbf{e}_{\alpha\beta} + \mathbf{V}_{\alpha\beta}\right), \tag{3.23}$$

with:

$$\mathbf{L}_{\alpha\beta}^{-1} = \frac{1}{\gamma_0^2 - \gamma_2^2}\begin{bmatrix}\gamma_0 + \gamma_2\cos(2\theta_e) & \gamma_2\sin(2\theta_e)\\ \gamma_2\sin(2\theta_e) & \gamma_0 - \gamma_2\cos(2\theta_e)\end{bmatrix}. \tag{3.24}$$

Defining the following vector:

$$\begin{aligned}\mathbf{F}_{\alpha\beta} = -\left(\mathbf{R}_s + \omega_e\frac{\partial\mathbf{L}_{\alpha\beta}}{\partial\theta_e}\right)\mathbf{i}_{\alpha\beta} - \omega_e\mathbf{e}_{\alpha\beta} + \mathbf{V}_{\alpha\beta} = \begin{bmatrix}F_\alpha\\ F_\beta\end{bmatrix} = \\ = \begin{bmatrix}-R_s i_\alpha - \omega_e\left(2\gamma_2\left(i_\alpha\sin(2\theta_e) - i_\beta\cos(2\theta_e)\right) - \Psi_{PM}\sin(\theta_e)\right) + V_\alpha\\ -R_s i_\beta + \omega_e\left(2\gamma_2\left(i_\alpha\cos(2\theta_e) + i_\beta\sin(2\theta_e)\right) - \Psi_{PM}\cos(\theta_e)\right) + V_\beta\end{bmatrix},\end{aligned} \tag{3.25}$$

the equation (3.23) becomes:

$$\frac{d}{dt}\mathbf{i}_{\alpha\beta} = \mathbf{L}_{\alpha\beta}^{-1}\mathbf{F}_{\alpha\beta} = \begin{bmatrix}(K_0 + K_2\cos(2\theta_e))F_\alpha + K_2\sin(2\theta_e)F_\beta\\ (K_0 - K_2\cos(2\theta_e))F_\beta + K_2\sin(2\theta_e)F_\alpha\end{bmatrix}, \tag{3.26}$$

where:

$$\begin{aligned}K_0 &= \frac{\gamma_0}{\gamma_0^2 - \gamma_2^2},\\ K_2 &= \frac{\gamma_2}{\gamma_0^2 - \gamma_2^2}.\end{aligned} \tag{3.27}$$

If γ_2 is small enough, we can simplify the electrical differential equation (3.26):

$$\frac{d}{dt}\mathbf{i}_{\alpha\beta} = K_0\mathbf{F}_{\alpha\beta}. \tag{3.28}$$

However, the assumption that γ_2 is small can be considered only for a narrow class of PMSMs. Equation (3.28) can be expressed simply as:

$$\begin{aligned}\tfrac{d}{dt}i_\alpha &= \tfrac{1}{L_0}\left(-R_s i_\alpha + \omega_e\Psi_{PM}\sin(\theta_e) + V_\alpha\right),\\ \tfrac{d}{dt}i_\beta &= \tfrac{1}{L_0}\left(-R_s i_\beta - \omega_e\Psi_{PM}\cos(\theta_e) + V_\beta\right).\end{aligned} \tag{3.29}$$

The previous equations are usually used for the implementation of back-EMF based sensorless technique since the extraction of the position information is straightforward. Let us now

consider the Park transformation matrix:

$$\mathbf{T}_P(\theta_e) = \begin{bmatrix} \cos(\theta_e) & \sin(\theta_e) & 0 \\ -\sin(\theta_e) & \cos(\theta_e) & 0 \\ 0 & 0 & 1 \end{bmatrix}. \tag{3.30}$$

In our case, only equations α and β will be considered, hence, the third row and column of $\mathbf{T}_P$ are not considered. The result of this transformation is calculated as follows:

$$\mathbf{V}_{dq} = \mathbf{T}_P \mathbf{V}_{\alpha\beta} = \mathbf{R}_s \mathbf{T}_P \mathbf{i}_{\alpha\beta} + \mathbf{T}_P \frac{d\mathbf{L}_{\alpha\beta}}{dt} \mathbf{i}_{\alpha\beta} + \mathbf{T}_P \mathbf{L}_{\alpha\beta} \frac{d\mathbf{i}_{\alpha\beta}}{dt} + \omega_e \mathbf{T}_P \frac{\partial \mathbf{\Psi}_{\alpha\beta}}{\partial \theta_e}, \tag{3.31}$$

thus:

$$\mathbf{V}_{dq} = \mathbf{R}_s \mathbf{i}_{dq} + \omega_e \mathbf{T}_P \frac{\partial \mathbf{L}_{\alpha\beta}}{\partial \theta_e} \mathbf{T}_P^{-1} \mathbf{i}_{dq} + \mathbf{T}_P \mathbf{L}_{\alpha\beta} \frac{d\left(\mathbf{T}_P^{-1} \mathbf{i}_{dq}\right)}{dt} + \omega_e \frac{\partial\left(\mathbf{T}_P \mathbf{\Psi}_{\alpha\beta}\right)}{\partial \theta_e}, \tag{3.32}$$

where:

$$\mathbf{T}_P \frac{\partial \mathbf{L}_{\alpha\beta}}{\partial \theta_e} \mathbf{T}_P^{-1} = \begin{bmatrix} 0 & -2\gamma_2 \\ -2\gamma_2 & 0 \end{bmatrix}, \tag{3.33}$$

$$\frac{d\left(\mathbf{T}_P^{-1} \mathbf{i}_{dq}\right)}{dt} = \omega_e \frac{\partial \mathbf{T}_P^{-1}}{\partial \theta_e} \mathbf{i}_{dq} + \mathbf{T}_P^{-1} \frac{d\mathbf{i}_{dq}}{dt}, \tag{3.34}$$

hence:

$$\mathbf{V}_{dq} = \mathbf{R}_s \mathbf{i}_{dq} + \omega_e \mathbf{L}_{rel} \mathbf{i}_{dq} + \mathbf{L}_{dq} \frac{d\mathbf{i}_{dq}}{dt} + \omega_e \mathbf{L}_{dq}^* \mathbf{i}_{dq} + \omega_e \mathbf{e}_{dq}, \tag{3.35}$$

where:

$$\mathbf{L}_{dq} = \mathbf{T}_P \mathbf{L}_{\alpha\beta} \mathbf{T}_P^{-1} = \begin{bmatrix} L_d & L_{dq} \\ L_{qd} & L_q \end{bmatrix} = \begin{bmatrix} \gamma_0 - \gamma_2 & 0 \\ 0 & \gamma_0 + \gamma_2 \end{bmatrix}, \tag{3.36}$$

$$\mathbf{L}_{dq}^* = \mathbf{T}_P \mathbf{L}_{\alpha\beta} \frac{\partial \mathbf{T}_P^{-1}}{\partial \theta_e} = \begin{bmatrix} 0 & -\gamma_0 + \gamma_2 \\ \gamma_0 + \gamma_2 & 0 \end{bmatrix}, \tag{3.37}$$

$$\mathbf{L}_{rel} = \mathbf{T}_P \frac{\partial \mathbf{L}_{\alpha\beta}}{\partial \theta_e} \mathbf{T}_P^{-1} = \begin{bmatrix} 0 & -2\gamma_2 \\ -2\gamma_2 & 0 \end{bmatrix}, \tag{3.38}$$

$$\mathbf{e}_{dq} = \frac{\partial\left(\mathbf{T}_P \mathbf{\Psi}_{\alpha\beta}\right)}{\partial \theta_e} = \begin{bmatrix} 0 \\ \Psi_{PM} \end{bmatrix}. \tag{3.39}$$

If we regroup the terms in common, we obtain:

$$\mathbf{V}_{dq} = \left(\mathbf{R}_s + \omega_e \left(\mathbf{L}_{rot,dq}\right)\right) \mathbf{i}_{dq} + \mathbf{L}_{dq} \frac{d\mathbf{i}_{dq}}{dt} + \omega_e \mathbf{e}_{dq}, \tag{3.40}$$

where:

$$\mathbf{L}_{rot,dq} = \mathbf{L}_{rel} + \mathbf{L}^*_{dq} = \begin{bmatrix} 0 & -\gamma_0 - \gamma_2 \\ \gamma_0 - \gamma_2 & 0 \end{bmatrix} = \begin{bmatrix} 0 & -L_q \\ L_d & 0 \end{bmatrix}, \tag{3.41}$$

Thus, in other terms:

$$\begin{bmatrix} V_d \\ V_q \end{bmatrix} = \begin{bmatrix} R_s i_d - \omega_e L_q i_q + L_d \dfrac{di_d}{dt} \\ R_s i_q + \omega_e L_d i_d + L_q \dfrac{di_q}{dt} + \omega_e \Psi_{PM} \end{bmatrix}. \tag{3.42}$$

Thus, even considering the generalized expression of the inductance matrix presented in equation (3.3) the stator reference frame can be simplified into equation (3.42) using the Park transformation.

3.2.2 Position error reference frame: tn-axis

In order to appreciate the effect of a potential position error on the evaluation of the Park-transformed equations, a new reference frame is defined, namely, the tn reference frame or position error reference frame. The following transformation matrix based on the position error $\tilde{\theta}_e$ is defined:

$$\mathbf{T}_P\left(\tilde{\theta}_e\right) = \begin{bmatrix} \cos\left(\tilde{\theta}_e\right) & \sin\left(\tilde{\theta}_e\right) \\ -\sin\left(\tilde{\theta}_e\right) & \cos\left(\tilde{\theta}_e\right) \end{bmatrix}. \tag{3.43}$$

The new equation system based on the reference frame tn can be defined as:

$$\begin{aligned} \mathbf{V}_{tn} &= \mathbf{T}_p\left(\tilde{\theta}_e\right) \mathbf{V}_{dq} = \\ &= \mathbf{T}_p \left(\mathbf{R}_s + \omega_e \mathbf{L}_{rot,dq}\right) \mathbf{T}_p^{-1} \mathbf{i}_{tn} + \mathbf{T}_p \mathbf{L}_{dq} \frac{d\left(\mathbf{T}_P^{-1} \mathbf{i}_{tn}\right)}{dt} + \omega_e \mathbf{e}_{tn}, \end{aligned} \tag{3.44}$$

where:

$$\frac{d\left(\mathbf{T}_P^{-1} \mathbf{i}_{tn}\right)}{dt} = \tilde{\omega}_e \frac{\partial \mathbf{T}_P^{-1}}{\partial \tilde{\theta}_e} \mathbf{i}_{tn} + \mathbf{T}_P^{-1} \frac{d\mathbf{i}_{tn}}{dt}, \tag{3.45}$$

then:

$$\mathbf{L}_{tn} = \mathbf{T}_P \mathbf{L}_{dq} \mathbf{T}_P^{-1} = \begin{bmatrix} \gamma_0 - \gamma_2 \cos\left(2\tilde{\theta}_e\right) & \gamma_2 \sin\left(2\tilde{\theta}_e\right) \\ \gamma_2 \sin\left(2\tilde{\theta}_e\right) & \gamma_0 + \gamma_2 \cos\left(2\tilde{\theta}_e\right) \end{bmatrix}, \tag{3.46}$$

$$\mathbf{L}^*_{tn} = \mathbf{T}_P \mathbf{L}_{dq} \frac{\partial \mathbf{T}_P^{-1}}{\partial \tilde{\theta}_e} = \begin{bmatrix} \gamma_2 \sin\left(2\tilde{\theta}_e\right) & -\gamma_0 + \gamma_2 \cos\left(2\tilde{\theta}_e\right) \\ \gamma_0 + \gamma_2 \cos\left(2\tilde{\theta}_e\right) & -\gamma_2 \sin\left(2\tilde{\theta}_e\right) \end{bmatrix}, \tag{3.47}$$

$$\mathbf{L}_{rot,tn} = \mathbf{T}_P \mathbf{L}_{rot,dq} \mathbf{T}_P^{-1} = \begin{bmatrix} -\gamma_2 \sin\left(2\tilde{\theta}_e\right) & -\gamma_0 - \gamma_2 \cos\left(2\tilde{\theta}_e\right) \\ \gamma_0 - \gamma_2 \cos\left(2\tilde{\theta}_e\right) & \gamma_2 \sin\left(2\tilde{\theta}_e\right) \end{bmatrix}, \tag{3.48}$$

leading to, eventually:

$$\mathbf{V}_{tn} = \left(\mathbf{R}_s + \omega_e \mathbf{L}_{rot,tn} + \tilde{\omega}_e \mathbf{L}_{tn}^*\right) \mathbf{i}_{tn} + \mathbf{L}_{tn} \frac{d\mathbf{i}_{tn}}{dt} + \omega_e \mathbf{e}_{tn}. \tag{3.49}$$

Let us bring the current derivative term in equation (3.49) on the left side and the voltage on the right side:

$$\frac{d\mathbf{i}_{tn}}{dt} = \mathbf{L}_{tn}^{-1} \left(- \left(\mathbf{R}_s + \omega_e \mathbf{L}_{rot,tn} + \tilde{\omega}_e \mathbf{L}_{tn}^*\right) \mathbf{i}_{tn} - \omega_e \mathbf{e}_{tn} + \mathbf{V}_{tn} \right), \tag{3.50}$$

where:

$$\mathbf{L}_{tn}^{-1} = \frac{1}{\gamma_0^2 - \gamma_2^2} \begin{bmatrix} \gamma_0 + \gamma_2 \cos\left(2\tilde{\theta}_e\right) & -\gamma_2 \sin\left(2\tilde{\theta}_e\right) \\ -\gamma_2 \sin\left(2\tilde{\theta}_e\right) & \gamma_0 - \gamma_2 \cos\left(2\tilde{\theta}_e\right) \end{bmatrix}. \tag{3.51}$$

We can notice the similarity of equation (3.50) to the $\alpha\beta$ reference frame equation (3.23). The effect of the parameter γ_2 cannot be neglected, therefore, the terms dependent on γ_2 will be isolated and a deeper analysis of the effect of the position error on the machine equation will be presented within the next subsection.

3.2.3 Equations description considering the position error

The previous equations will be now divided into two part: the first part will be similar to the dq reference frame equation, while the second part will contain all the terms depending on the position error $\tilde{\theta}_e$. In this way we could define the part depending on the rotor position as a disturbance term. The equations can be readjusted as:

$$\begin{aligned} \frac{d}{dt}\begin{bmatrix} i_t \\ i_n \end{bmatrix} = & \begin{bmatrix} -\frac{R_s}{L_d} & \omega_e \frac{L_q}{L_d} + \tilde{\omega}_e \\ -\omega_e \frac{L_d}{L_q} - \tilde{\omega}_e & -\frac{R_s}{L_q} \end{bmatrix} \begin{bmatrix} i_t \\ i_n \end{bmatrix} + \omega_e \frac{\Psi_{PM}}{L_q} \begin{bmatrix} \sin\left(\tilde{\theta}_e\right) \\ -\cos\left(\tilde{\theta}_e\right) \end{bmatrix} + \begin{bmatrix} \frac{1}{L_d} & 0 \\ 0 & \frac{1}{L_q} \end{bmatrix} \begin{bmatrix} V_t \\ V_n \end{bmatrix} + \\ & + G\left(\tilde{\theta}_e\right) \left(\begin{bmatrix} \chi_1\left(\tilde{\theta}_e\right) & \chi_1\left(\tilde{\theta}_e + \frac{\pi}{2}\right) \\ \chi_2\left(\tilde{\theta}_e + \frac{\pi}{2}\right) & \chi_2\left(\tilde{\theta}_e\right) \end{bmatrix} \begin{bmatrix} i_t \\ i_n \end{bmatrix} - \mathbf{T}_P\left(\tilde{\theta}_e\right) \begin{bmatrix} V_n \\ V_t \end{bmatrix} + 2\omega_e \Psi_{PM} \begin{bmatrix} K_1\left(\tilde{\theta}_e\right) \\ K_2\left(\tilde{\theta}_e\right) \end{bmatrix} \right), \end{aligned} \tag{3.52}$$

$$
\begin{aligned}
\chi_1\left(\tilde{\theta}_e\right) &= R_s \sin\left(\tilde{\theta}_e\right) + \omega_e \left(L_q + L_d\right) \cos\left(\tilde{\theta}_e\right), \\
\chi_2\left(\tilde{\theta}_e\right) &= R_s \cos\left(\tilde{\theta}_e\right) + \omega_e \left(L_q + L_d\right) \sin\left(\tilde{\theta}_e\right), \\
K_1\left(\tilde{\theta}_e\right) &= \cos^2\left(\tilde{\theta}_e\right) \sin\left(\tilde{\theta}_e\right), \\
K_2\left(\tilde{\theta}_e\right) &= -\sin^2\left(\tilde{\theta}_e\right) \cos\left(\tilde{\theta}_e\right), \\
G\left(\tilde{\theta}_e\right) &= \frac{L_q - L_d}{L_d L_q} \sin\left(\tilde{\theta}_e\right).
\end{aligned}
\tag{3.53}
$$

By applying the decoupling strategy:

$$
\begin{aligned}
V_t &= -L_q i_n \hat{\omega}_e + V_t^*, \\
V_n &= L_d i_t \hat{\omega}_e + V_n^*,
\end{aligned}
\tag{3.54}
$$

we obtain:

$$
\begin{aligned}
\frac{d}{dt}\begin{bmatrix} i_t \\ i_n \end{bmatrix} = &\begin{bmatrix} -\frac{R_s}{L_d} & \left(\frac{L_q + L_d}{L_d}\right)\tilde{\omega}_e \\ -\left(\frac{L_q + L_d}{L_q}\right)\tilde{\omega}_e & -\frac{R_s}{L_q} \end{bmatrix}\begin{bmatrix} i_t \\ i_n \end{bmatrix} + \omega_e \frac{\Psi_{PM}}{L_q}\begin{bmatrix} \sin\left(\tilde{\theta}_e\right) \\ -\cos\left(\tilde{\theta}_e\right) \end{bmatrix} + \\
&+ \begin{bmatrix} \frac{1}{L_d} & 0 \\ 0 & \frac{1}{L_q} \end{bmatrix}\begin{bmatrix} V_t^* \\ V_n^* \end{bmatrix} + G\left(\tilde{\theta}_e\right)\left(\begin{bmatrix} \chi_1\left(\tilde{\theta}_e\right) & \chi_1\left(\tilde{\theta}_e + \frac{\pi}{2}\right) \\ \chi_2\left(\tilde{\theta}_e + \frac{\pi}{2}\right) & \chi_2\left(\tilde{\theta}_e\right) \end{bmatrix}\begin{bmatrix} i_t \\ i_n \end{bmatrix} - \mathbf{T}_P\left(\tilde{\theta}_e\right)\begin{bmatrix} V_n \\ V_t \end{bmatrix}\right),
\end{aligned}
\tag{3.55}
$$

or equivalently:

$$
\begin{aligned}
\frac{d}{dt}\begin{bmatrix} i_t \\ i_n \end{bmatrix} = \mathbf{A}\left(\tilde{\omega}_e\right)\begin{bmatrix} i_t \\ i_n \end{bmatrix} + \omega_e \frac{\Psi_{PM}}{L_q}\begin{bmatrix} \sin\left(\tilde{\theta}_e\right) \\ -1 + 2\sin^2\left(\frac{\tilde{\theta}_e}{2}\right) \end{bmatrix} + \begin{bmatrix} \frac{1}{L_d} & 0 \\ 0 & \frac{1}{L_q} \end{bmatrix}\begin{bmatrix} V_t^* \\ V_n^* \end{bmatrix} + \\
+ G\left(\tilde{\theta}_e\right)\left(\begin{bmatrix} \chi_1\left(\tilde{\theta}_e\right) & \chi_1\left(\tilde{\theta}_e + \frac{\pi}{2}\right) \\ \chi_2\left(\tilde{\theta}_e + \frac{\pi}{2}\right) & \chi_2\left(\tilde{\theta}_e\right) \end{bmatrix}\begin{bmatrix} i_t \\ i_n \end{bmatrix} - \mathbf{T}_P\left(\tilde{\theta}_e\right)\begin{bmatrix} V_n \\ V_t \end{bmatrix}\right).
\end{aligned}
\tag{3.56}
$$

Bringing the last term dependent on $\tilde{\theta}_e$ to the right:

$$
\begin{aligned}
\frac{d}{dt}\begin{bmatrix} i_t \\ i_n \end{bmatrix} = \mathbf{A}\left(\tilde{\omega}_e\right)\begin{bmatrix} i_t \\ i_n \end{bmatrix} - \begin{bmatrix} 0 \\ \omega_e \frac{\Psi_{PM}}{L_q} \end{bmatrix} + \begin{bmatrix} \frac{1}{L_d} & 0 \\ 0 & \frac{1}{L_q} \end{bmatrix}\begin{bmatrix} V_t^* \\ V_n^* \end{bmatrix} + \omega_e \frac{\Psi_{PM}}{L_q}\begin{bmatrix} \sin\left(\tilde{\theta}_e\right) \\ 2\sin^2\left(\frac{\tilde{\theta}_e}{2}\right) \end{bmatrix} + \\
+ G\left(\tilde{\theta}_e\right)\left(\begin{bmatrix} \chi_1\left(\tilde{\theta}_e\right) & \chi_1\left(\tilde{\theta}_e + \frac{\pi}{2}\right) \\ \chi_2\left(\tilde{\theta}_e + \frac{\pi}{2}\right) & \chi_2\left(\tilde{\theta}_e\right) \end{bmatrix}\begin{bmatrix} i_t \\ i_n \end{bmatrix} - \mathbf{T}_P\left(\tilde{\theta}_e\right)\begin{bmatrix} V_n \\ V_t \end{bmatrix}\right),
\end{aligned}
\tag{3.57}
$$

we get eventually the following form:

$$\frac{d}{dt}\begin{bmatrix} i_t \\ i_n \end{bmatrix} = \mathbf{A}\left(\tilde{\omega}_e\right)\begin{bmatrix} i_t \\ i_n \end{bmatrix} - \begin{bmatrix} 0 \\ \omega_e \dfrac{\Psi_{PM}}{L_q} \end{bmatrix} + \begin{bmatrix} \dfrac{1}{L_d} & 0 \\ 0 & \dfrac{1}{L_q} \end{bmatrix}\begin{bmatrix} V_t^* \\ V_n^* \end{bmatrix} + \\ + G\left(\tilde{\theta}_e\right)\left(a_\Psi \begin{bmatrix} 1 \\ \dfrac{\tan\left(\frac{\tilde{\theta}_e}{2}\right)}{2} \end{bmatrix} + \begin{bmatrix} \chi_1\left(\tilde{\theta}_e\right) & \chi_1\left(\tilde{\theta}_e + \dfrac{\pi}{2}\right) \\ \chi_2\left(\tilde{\theta}_e + \dfrac{\pi}{2}\right) & \chi_2\left(\tilde{\theta}_e\right) \end{bmatrix}\begin{bmatrix} i_t \\ i_n \end{bmatrix} - \mathbf{T}_P\left(\tilde{\theta}_e\right)\begin{bmatrix} V_n \\ V_t \end{bmatrix}\right), \quad (3.58)$$

with:

$$a_\Psi = \omega_e L_d \frac{\Psi_{PM}}{L_q - L_d}. \quad (3.59)$$

We can simplify this equation considering that the term multiplied by $G\left(\tilde{\theta}_e\right)$ is a disturbance function dependent on the system state:

$$\frac{d}{dt}\begin{bmatrix} i_t \\ i_n \end{bmatrix} = \mathbf{A}\left(\tilde{\omega}_e\right)\begin{bmatrix} i_t \\ i_n \end{bmatrix} - \begin{bmatrix} 0 \\ \omega_e \dfrac{\Psi_{PM}}{L_q} \end{bmatrix} + \begin{bmatrix} \dfrac{1}{L_d} & 0 \\ 0 & \dfrac{1}{L_q} \end{bmatrix}\begin{bmatrix} V_t^* \\ V_n^* \end{bmatrix} + D\left(\tilde{\theta}_e, i_t, i_n, \omega_e, V_t, V_n\right), \quad (3.60)$$

or:

$$\frac{d}{dt}\begin{bmatrix} i_t \\ i_n \end{bmatrix} = \mathbf{A}\left(\tilde{\omega}_e\right)\begin{bmatrix} i_t \\ i_n \end{bmatrix} + \mathbf{B}\begin{bmatrix} V_t^* \\ V_n^* \end{bmatrix} + \omega_e \frac{\mathbf{e}_{dq}}{L_q} + D\left(\tilde{\theta}_e, i_t, i_n, \omega_e, V_t, V_n\right), \quad (3.61)$$

where:

$$\mathbf{B} = \begin{bmatrix} \dfrac{1}{L_d} & 0 \\ 0 & \dfrac{1}{L_q} \end{bmatrix}, \quad \mathbf{A}\left(\tilde{\omega}_e\right) = \begin{bmatrix} -\frac{R_s}{L_d} & \left(\frac{L_q + L_d}{L_d}\right)\tilde{\omega}_e \\ -\left(\frac{L_q + L_d}{L_q}\right)\tilde{\omega}_e & -\frac{R_s}{L_q} \end{bmatrix}. \quad (3.62)$$

Let us call the current vector $\mathbf{x}(t)$, the voltage vector $\mathbf{u}(t)$ and the disturbance vector $\mathbf{d}(t)$. We get:

$$\dot{\mathbf{x}}(t) = \mathbf{A}\left(\tilde{\omega}_e\right)\mathbf{x}(t) + \mathbf{B}\mathbf{u}(t) + \omega_e \frac{\mathbf{e}_{dq}}{L_q} + \mathbf{d}(t). \quad (3.63)$$

It is clear from equation (3.63) that the current control strategy used must be developed in order to contrast the effect of the disturbance vector $\mathbf{d}(t)$. Thus, considering the PI controllers for the $d-$ and $q-$axis, the application of a AVO tuning method could not lead anymore to the desired control behavior (the AVO method does not optimize the disturbance rejection capability of the controller). Moreover, even if a new control strategy able to perform a complete rejection of $\mathbf{d}(t)$ were developed, the following resulting torque will be actually

generated by the motor:

$$T_e = \frac{3}{2} n_{pp}^2 \left(\Psi_{PM} \left(i_n \cos\left(\tilde{\theta}_e\right) - i_t \sin\left(\tilde{\theta}_e\right) \right) - 2\gamma_2 \cos\left(2\tilde{\theta}_e\right) i_t i_n + \gamma_2 \sin\left(2\tilde{\theta}_e\right) \left(i_n^2 - i_t^2 \right) \right). \quad (3.64)$$

Thus, considering the current control with reference vector:

$$\mathbf{i}_{tn}^{ref} = \begin{bmatrix} 0 \\ I_{ref} \end{bmatrix}, \quad (3.65)$$

and considering a complete rejection of the disturbances, we obtain at steady state:

$$T_e = \frac{3}{2} n_{pp}^2 \Psi_{PM} I_{ref} \left(\cos\left(\tilde{\theta}_e\right) + \gamma_2 I_{ref} \sin\left(2\tilde{\theta}_e\right) \right). \quad (3.66)$$

3.2.4 Considerations about the standard DFC position error

Let us now consider, for example, the estimation error Δ defined in equation (3.13) for the standard DFC algorithm. We can then define:

$$\tilde{\theta}_e = \frac{\Delta}{2} = \frac{1}{2} \operatorname{atan}\left(\frac{p \sin(6\theta_e)}{1 - p\cos(6\theta_e)} \right). \quad (3.67)$$

By substituting equation (3.67) in equation (3.66), we obtain the following:

$$T_e = \frac{3}{2} n_{pp}^2 \Psi_{PM} I_{ref} \left(\cos\left(\frac{1}{2} \operatorname{atan}\left(\frac{p \sin(6\theta_e)}{1 - p\cos(6\theta_e)} \right) \right) + \gamma_2 I_{ref} \frac{p \sin(6\theta_e)}{\sqrt{p^2 - 2p\cos(6\theta_e) + 1}} \right). \quad (3.68)$$

Considering that: $\gamma_2 = \dfrac{L_q - L_d}{2}$, we obtain:

$$T_e = \frac{3}{2} n_{pp}^2 \Psi_{PM} I_{ref} \left(\cos\left(\tilde{\theta}_e\right) + \frac{L_q - L_d}{2} I_{ref} \frac{p \sin(6\theta_e)}{\sqrt{p^2 - 2p\cos(6\theta_e) + 1}} \right). \quad (3.69)$$

Since an analytical analysis would be too complicated, a numerical approach can be considered in order to determine the values of T_e. In Figure 3.4 the term T_e is depicted considering various values of p for a complete electrical rotor revolution. As shown, a ripple torque caused by the exploitation of the DFC position is generated. Then, it is clear that the DFC technique decreases the efficiency of the FOC. Beside that, we can consider this performance deterioration acceptable for the majority of PMSMs (it has to be said that normally p is smaller than 0.5). Further considerations can be made if also the speed estimation error $\tilde{\omega}_e$ is taken into account. In fact, the estimated speed ω_e is used in case speed control is required. The most straightforward way to obtain the estimated speed is through derivation of the estimated position:

$$\hat{\omega}_e = \frac{\mathrm{d}\hat{\theta}_e}{\mathrm{d}t}. \quad (3.70)$$

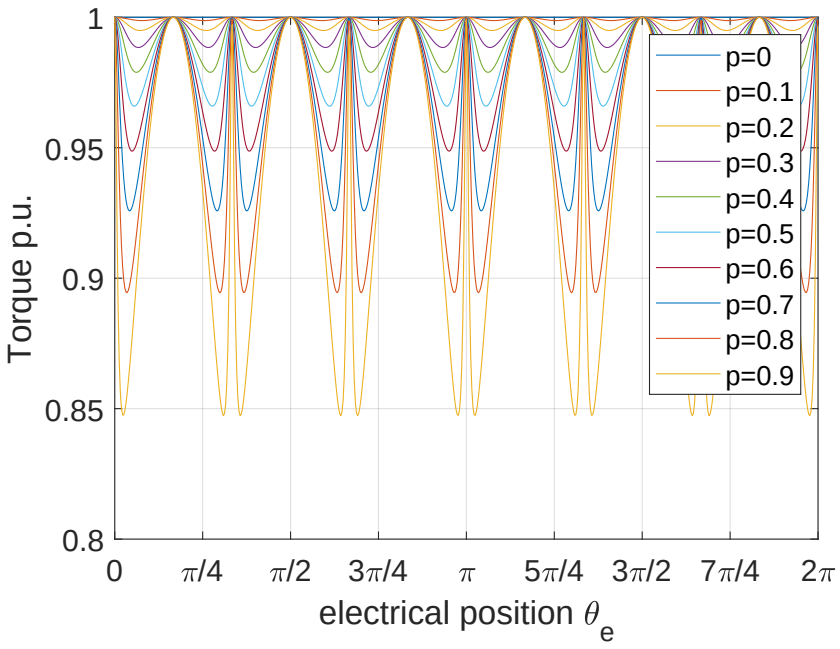

Figure 3.4: Electrical torque generated considering values of p varying from 0 to 0.9 and $\gamma_2 I_{ref} = 0$

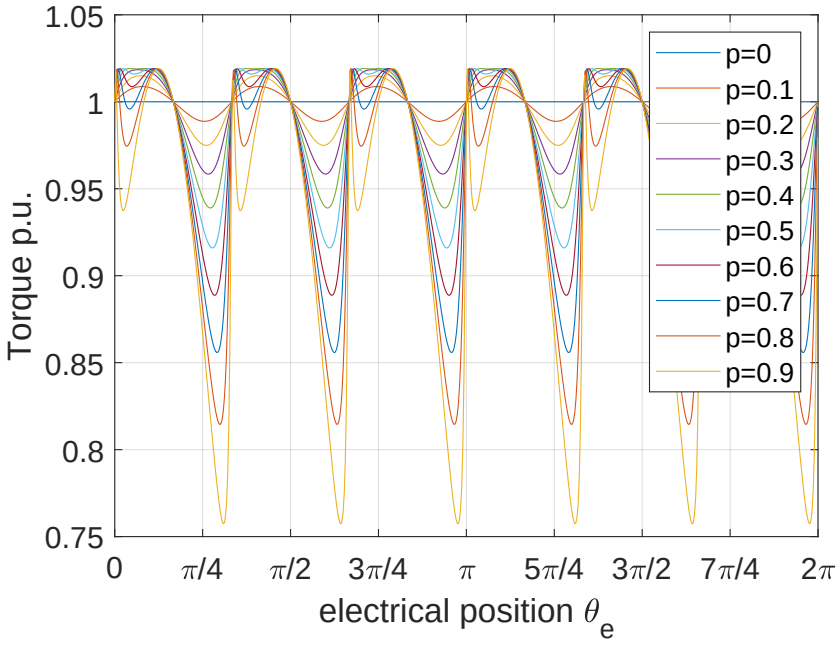

Figure 3.5: Electrical torque generated considering values of p varying from 0 to 0.9 and $\gamma_2 I_{ref} = 0.1$

Considering the DFC estimated position, we obtain:

$$\hat{\omega}_e = \frac{\mathrm{d}\left(\theta_e + \frac{\Delta}{2}\right)}{\mathrm{d}t} = \omega_e + \frac{1}{2}\frac{\mathrm{d}\Delta}{\mathrm{d}t} = \omega_e + \omega_e \frac{3p\left(p + cos(6\theta_e)\right)}{p^2 + 2p\cos\left(6\theta_e\right) + 1} = \omega_e + \tilde{\omega}_e, \tag{3.71}$$

with:

$$\tilde{\omega}_e = \omega_e \frac{3p\left(p + \cos(6\theta_e)\right)}{p^2 + 2p\cos\left(6\theta_e\right) + 1}. \tag{3.72}$$

From the previous equation we can state that:

$$\tilde{\omega}_e \in \left[\omega_e \frac{1+2|p|}{1-|p|}, \omega_e \frac{1-2|p|}{1+|p|}\right]. \tag{3.73}$$

The estimated speed error is a bounded periodic function and its boundaries are dependent on the parameter p and they are linearly dependent on ω_e. Obviously, that behavior could deteriorate the speed control of the motor especially for high-speed operations. Normally, a low-pass filter is applied to the speed measurement path in order to diminish undesired effects. The tuning of the filter is normally done by reasonable assumptions on the nature of the possible disturbances acting on the measured speed signal. In case DFC is used, these assumptions may concern also the nominal speed of the motor as well as the value of the parameter p. Indeed, the employment of a well tuned low-pass filter could solve this issue but the control system performance may in some cases be drastically reduced.

3.3 Improvement of the position estimation: Iterative Vector Decoupling

The following section is based on the scientific contributions published in [54]. As described in the previous section, the DFC technique, as well as potentially other sensorless techniques, introduces an error on the estimated position that may decrease the performance of the FOC. By a deeper analysis of the position estimation error expression, as presented in equation (3.13), one can state that a fourth harmonic is systematically introduced on the DFC signal vector $\mathbf{\Gamma}_{\alpha\beta}$ if $b_{DFC} \neq 0$ holds. In fact:

$$2\hat{\theta}_e = \chi = \operatorname{atan}\left(\frac{a\sin\left(2\omega_e t\right) + b\sin\left(4\omega_e t\right)}{a\cos\left(2\omega_e t\right) + b\cos\left(4\omega_e t\right)}\right) = 2\theta_e + \Delta \quad \text{where} \quad \omega_e t = \theta_e. \tag{3.74}$$

The effects of higher order harmonics on the estimated position using sensorless technique has been already studied by Degner in [55] for an arbitrary injection based sensorless technique. In [27], on the base of the theory presented within the previous contribution, a PLL filter was proposed in order to eliminate the fourth harmonic. This solution, beside the satisfactory behavior proven through experiments, cannot assure a convergence of the estimated position to the real one for the whole speed range, unless the PLL filter is perfectly tuned. For that reason, a new technique for the elimination of the fourth harmonic, named Iterative Vector Decoupling (IVD), is presented in this work. This method, differently from the one

proposed by Paulus, is based on an iterative algorithm that aims at eliminating the fourth harmonic statically. In other words, the IVD is able to reduce the forth harmonic effect without the use of additional dynamical processes such as PLL filters or state observers.
In this section, the IVD method is presented and analyzed considering the DFC position estimation in equation (3.74). From now on, we will refer to that combination using the acronym IVD-DFC (Iterative Vector Decoupling - Direct Flux Control). Firstly, the new algorithm operations are introduced. The convergence of the IVD-DFC to the real position will be proven using a rigorous mathematical analysis. Afterwards, a modification of the algorithm will be presented when saturation effects are considered. Eventually, sensitivity analysis is given when uncertainties on the parameters are taken into account.

3.3.1 IVD-DFC operations

As shown in equation (3.74), the variable χ carries the information about the angular position $2\theta_e$ and the error Δ. We can consider this variable a good approximation of $2\theta_e$ if the value of b is not too large. If we suppose to know the parameter b, one may try to reduce the effect of the fourth harmonic term of Γ_β and Γ_α by algebraically subtracting the fourth harmonic on Γ_β and Γ_α. Let us suppose we are working at a certain time instant. First, we include in our notation a numbered subscript as index for the iterations. Thus, the value of the initial estimation is $2\hat{\theta}_0$ and it is exactly equal to χ. Then, the initial estimation obtained is used for the first iteration:

$$2\hat{\theta}_1 = -\arctan\left(\frac{\Gamma_\beta - b\sin\left(4\hat{\theta}_0\right)}{\Gamma_\alpha - b\cos\left(4\hat{\theta}_0\right)}\right). \tag{3.75}$$

The idea is to reduce the effect of the second harmonic using the estimated $\hat{\theta}$ previously calculated. As it will be shown, equation (3.75) introduces another deviation term Δ_1. If we can prove that $\|\Delta_1\| < \|\Delta_0\|$, we may assume that the following algorithm:

$$2\hat{\theta}_k = -\arctan\left(\frac{\Gamma_\beta - b\sin\left(4\hat{\theta}_{k-1}\right)}{\Gamma_\alpha - b\cos\left(4\hat{\theta}_{k-1}\right)}\right) \quad \text{where } k = 1, 2, ..., n, \tag{3.76}$$

might bring the estimation error to zero. In other words, we want to prove that for equation (3.76) the following limit holds:

$$\lim_{n\to\infty} 2\hat{\theta}_n = 2\theta_e. \tag{3.77}$$

The IVD-DFC algorithm consists actually in equation (3.76) and its schematic is shown in Figure 3.6. The first operation is to extract the raw estimated position $2\hat{\theta}_0$ using equation (3.74). Once the first information is obtained, the iterations presented in equation (3.76) can be performed. A new estimation of the variable $2\theta_e$ is given after n iterations. Thus, a large number of iterations can be problematic for a low-cost microcontroller to be executed in real time. Anyway, as shown in Figures 3.7 and 3.8, even a single iteration can already considerably improve the position estimation.

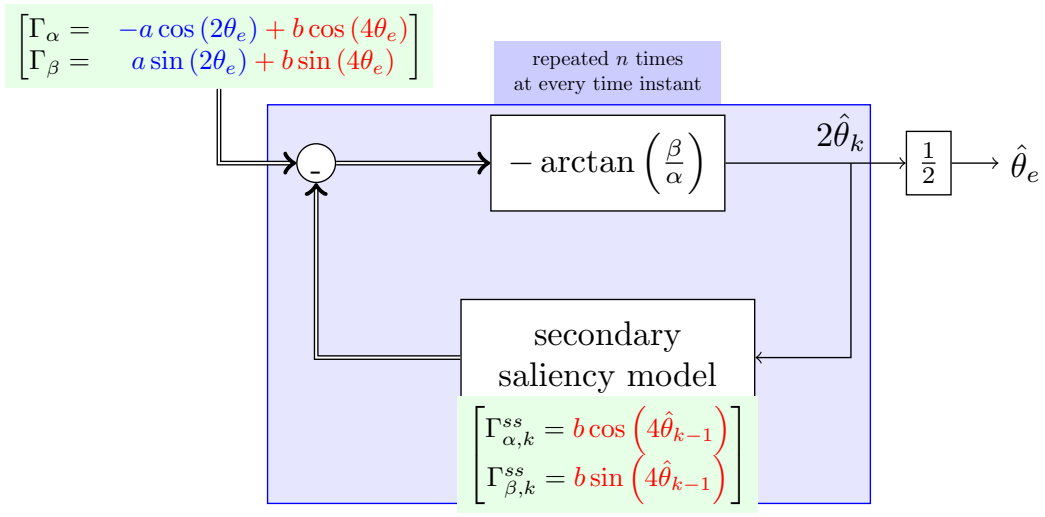

Figure 3.6: Flowchart of the IVD-DFC algorithm. The highlighted part in blue is the iterative part. It is assumed that the vector $\mathbf{\Gamma}^{ss}_{\alpha,\beta}$ is a zero vector for k = 0.

Let us now analyze the proposed algorithm by looking at the first iteration. Equation (3.75) can be manipulated in the following manner:

$$\begin{aligned}
2\hat{\theta}_1 &= \arctan\left(\frac{a\sin(2\theta_e) + b\sin(4\theta_e) - b\sin\left(4\hat{\theta}_0\right)}{a\cos(2\theta_e) - b\cos(4\theta_e) + b\cos\left(4\hat{\theta}_0\right)}\right)\\
&= \angle\left(ae^{j2\theta_e} - be^{-j4\theta_e} + be^{-j4\hat{\theta}_0}\right)\\
&= 2\theta_e + \angle\left(1 - pe^{-j6\theta_e} + pe^{-j\left(4\hat{\theta}_0 + 2\theta_e\right)}\right)\\
&= 2\theta_e + \angle\left(1 - pe^{-j6\theta_e} + pe^{-j(6\theta_e + 2\Delta_0)}\right)\\
&= 2\theta_e + \angle\left(1 + p\left(e^{-j2\Delta_0} - 1\right)e^{-j6\theta_e}\right),
\end{aligned} \tag{3.78}$$

where:

$$\begin{aligned}
\Delta_0 = \Delta &= \operatorname{atan}\left(\frac{p\sin(6\theta_e)}{1 - p\cos(6\theta_e)}\right),\\
p &= \frac{b}{a}.
\end{aligned} \tag{3.79}$$

Let us consider the following proposition:

Proposition 1. *The sum of two unitary complex exponential numbers* $\Phi = e^{j\gamma_1} + e^{j\gamma_2}$ *can be written as:* $\Phi = 2\cos\left(\frac{\gamma_2 - \gamma_1}{2}\right)e^{j\left(\frac{\gamma_2 + \gamma_1}{2}\right)}$.

From Equation (3.78) using the previous proposition and defining $\gamma_2 = -\pi$ and $\gamma_1 = -2\Delta_0$

one gets:

$$
\begin{aligned}
2\hat{\theta}_1 &= 2\theta_e + \angle\left(1 + 2p\cos\left(\Delta_0 - \frac{\pi}{2}\right)e^{-j\left(6\theta_e+\Delta_0+\frac{\pi}{2}\right)}\right) \\
&= 2\theta_e + \angle\left(1 + 2p\sin\left(\Delta_0\right)e^{-j\left(6\theta_e+\Delta_0+\frac{\pi}{2}\right)}\right) \\
&= 2\theta_e + \arctan\left(\frac{-2p\sin\left(\Delta_0\right)\sin\left(6\theta_e+\Delta_0+\frac{\pi}{2}\right)}{1+2p\sin\left(\Delta_0\right)\cos\left(6\theta_e+\Delta_0+\frac{\pi}{2}\right)}\right) \\
&= 2\theta_e + \arctan\left(\frac{-2p\sin\left(\Delta_0\right)\cos\left(6\theta_e+\Delta_0\right)}{1-2p\sin\left(\Delta_0\right)\sin\left(6\theta_e+\Delta_0\right)}\right) \\
&= 2\theta_e + \Delta_1.
\end{aligned}
\tag{3.80}
$$

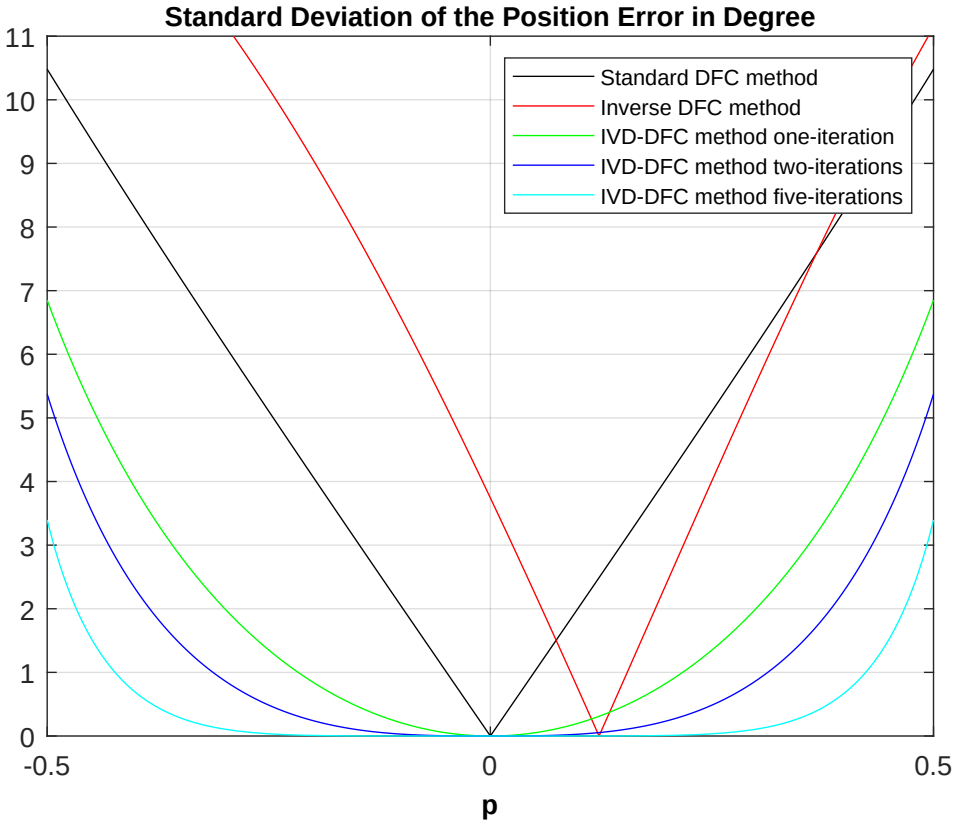

Figure 3.7: Comparison of the position standard deviation errors of the presented methods. The plot is referred to a machine with the following inductance values: $L_0 = 442.2$ µH, $M_0 = 20.7$ µH, $L_2 = 103.3$ µH. The parameter M_2 is let vary between $L_0 + M_0 - L_2$ and $L_0 - M_0 - L_2$ in order to get p range between -0.5 and 0.5.

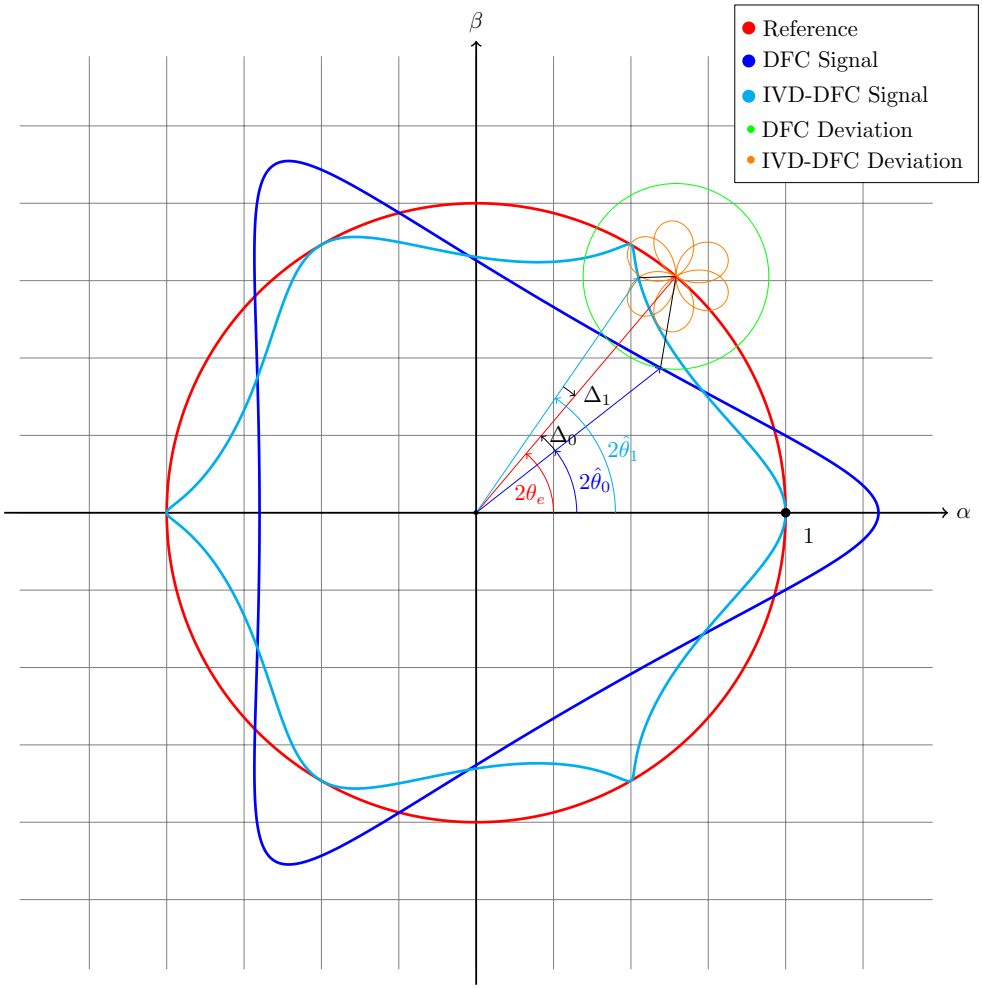

Figure 3.8: Plain representation of the DFC signals: $\frac{\Gamma_\alpha}{a}$ and $\frac{\Gamma_\beta}{a}$ respectively on the α and β axis (blue line). The red circle represents the signals for the case $b = 0$ and is taken as reference. The green circle with radius p represents the second harmonic. The light blue line represents the α and β signals obtained from the IVD-DFC algorithm. The orange line is the path taken by the new estimation error Δ_1, its maximal amplitude is smaller than p (case with $p = 0.3$).

A relation between Δ_k and its previous value Δ_{k-1} can be found from equation (3.80):

$$\Delta_k = \arctan\left(\frac{-2p\sin(\Delta_{k-1})\cos(3x+\Delta_{k-1})}{1-2p\sin(\Delta_{k-1})\sin(3x+\Delta_{k-1})}\right). \tag{3.81}$$

A graphical visualization of the iterations effect is shown in Figure 3.9. Next step is to prove that the deviation $|\Delta_k|$ is convergent to zero, namely:

$$\lim_{k\to\infty} |\Delta_k| = 0. \tag{3.82}$$

3.3.2 IVD-DFC convergence analysis

The convergence of the iterative method to the real position has been shown graphically in Figure 3.9. However, the algorithm has to be mathematically proven in order to determine for which conditions the convergence holds. Therefore, since we are dealing with discrete quantities, we will introduce the definition of a convergent sequence:

Definition 1. *Let be given a real value sequence* X_k*. The sequence is said to be linearly convergent (at least) to zero if exists a value* $\sigma \in [0,1)$ *such that* $|X_k| \leq \sigma |X_{k-1}|$ $\forall k \in [1,2,...,n]$*. Then,* $\lim_{k\to\infty} |X_k| = 0$*.*

In order to prove equation (3.82) the following lemma is presented.

Lemma 1. *Let us consider a real value sequence* X_k *defined on the interval* $\left[-\frac{\pi}{2}, \frac{\pi}{2}\right]$*. If* $\tan(X_k)$ *is at least linearly convergent to zero, then also the original sequence* X_k *is at least linearly convergent to the same value.*

The previous lemma will be useful for the proof of the following theorem.

Theorem 1. *Let be the following initial function:* $\Delta_0(\theta_e, p) = -\arctan\left(\frac{p\sin(6\theta_e)}{1+p\cos(6\theta_e)}\right)$ *parameterized by* $p \in \mathbb{R}$ *and defined* $\forall x \in \mathbb{R}$*. If the following sequence:* $\Delta_k(\theta_e, p) = \arctan\left(\frac{2p\sin(\Delta_{k-1}(\theta_e,p))\cos(6\theta_e+\Delta_{k-1}(\theta_e,p))}{1+2p\sin(\Delta_{k-1}(\theta_e,p))\sin(6\theta_e+\Delta_{k-1}(\theta_e,p))}\right)$ *is defined* $\forall k \in \mathbb{N}^0$*, then the sequence* Δ_k *is linearly convergent if and only if* $|p| < \frac{1}{2}$*.*

Proof. Let us prove first the following statement:

$$|\tan(\Delta_k(\theta_e,p))| \leq \gamma(p)\,|\tan(\Delta_{k-1}(\theta_e,p))|, \tag{3.83}$$

where:

$$\gamma(p) = 2|p|. \tag{3.84}$$

It is trivial to see that the previous sequence is linearly convergent only if $\gamma(p) < 1$ or $|p| < \frac{1}{2}$ (necessary condition). Let us elaborate the equations considering $|p| < \frac{1}{2}$ (sufficient condition). First, let us develop the left side of the inequality in equation (3.83). For simplicity we put $\Delta_k(\theta_e, p) = \Delta_k$:

$$\begin{aligned}
|\tan(\Delta_k)| &= \left|\tan\left(\arctan\left(\frac{-2p\sin(\Delta_{k-1})\cos(6\theta_e+\Delta_{k-1})}{1-2p\sin(\Delta_{k-1})\sin(6\theta_e+\Delta_{k-1})}\right)\right)\right| \\
&= \left|\frac{-2p\sin(\Delta_{k-1})\cos(6\theta_e+\Delta_{k-1})}{1-2p\sin(\Delta_{k-1})\sin(6\theta_e+\Delta_{k-1})}\right| \\
&= \frac{|-2p\sin(\Delta_{k-1})\cos(6\theta_e+\Delta_{k-1})|}{|1-2p\sin(\Delta_{k-1})\sin(6\theta_e+\Delta_{k-1})|} \\
&= \frac{2|p|\,|\sin(\Delta_{k-1})|\,|\cos(6\theta_e+\Delta_{k-1})|}{|1-2p\sin(\Delta_{k-1})\sin(6\theta_e+\Delta_{k-1})|}.
\end{aligned} \tag{3.85}$$

Then, substituting equation (3.85) in equation (3.83), we obtain:

$$\frac{2|p||\sin(\Delta_{k-1})||\cos(6\theta_e+\Delta_{k-1})|}{|1-2p\sin(\Delta_{k-1})\sin(6\theta_e+\Delta_{k-1})|} \leq 2|p|\frac{|\sin(\Delta_{k-1})|}{|\cos(\Delta_{k-1})|}. \tag{3.86}$$

The previous inequality will be used in order to find the values of p that satisfy the inequality. The terms can be elaborated as follows:

$$\begin{gathered}
|\cos(\Delta_{k-1})|\frac{\cancel{2|p||\sin(\Delta_{k-1})|}|\cos(6\theta_e+\Delta_{k-1})|}{|1-2p\sin(\Delta_{k-1})\sin(6\theta_e+\Delta_{k-1})|} \leq \cancel{2|p||\sin(\Delta_{k-1})|} \\
\frac{|\cos(\Delta_{k-1})||\cos(6\theta_e+\Delta_{k-1})|}{|1-2p\sin(\Delta_{k-1})\sin(6\theta_e+\Delta_{k-1})|} \leq 1 \\
\overbrace{|\cos(\Delta_{k-1})\cos(6\theta_e+\Delta_{k-1})|}^{\chi_1(\theta_e,\Delta_{k-1})} \leq \overbrace{|1-2p\sin(\Delta_{k-1})\sin(6\theta_e+\Delta_{k-1})|}^{\chi_2(\theta_e,\Delta_{k-1})}.
\end{gathered} \tag{3.87}$$

We can see that for $|p| < \frac{1}{2}$, the statement $\chi_2(\theta_e, \Delta_{k-1}) > 0$ is always true.
In the first case: $\chi_1(\theta_e, \Delta_{k-1}) \geq 0$:

$$\begin{gathered}
\cos(\Delta_{k-1})\cos(6\theta_e+\Delta_{k-1}) \leq 1-2p\sin(\Delta_{k-1})\sin(6\theta_e+\Delta_{k-1}) \\
\cos(\Delta_{k-1})\cos(6\theta_e+\Delta_{k-1})+2p\sin(\Delta_{k-1})\sin(6\theta_e+\Delta_{k-1}) \leq 1 \\
(1+2p)\cos(-6\theta_e)+(1-2p)\cos(6\theta_e+2\Delta_{k-1}) \leq 2.
\end{gathered} \tag{3.88}$$

We can rewrite the last inequality as follows:

$$c_1\cos(y_1)+c_2\cos(y_2) \leq 2, \tag{3.89}$$

with $c_1 = 1+2p$, $c_2 = 1-2p$, $y_2 = -6\theta_e$ and $y_1 = 6\theta_e + 2\Delta_{k-1}$.
One can state that:

$$c_1\cos(y_1)+c_2\cos(y_2) \leq |c_1\cos(y_1)+c_2\cos(y_2)|. \tag{3.90}$$

Then, applying the triangular inequality statement, we can write:

$$|c_1\cos(y_1)+c_2\cos(y_2)| \leq |c_1\cos(y_1)|+|c_2\cos(y_2)| \leq |c_1|+|c_2|. \tag{3.91}$$

Thus, putting together equation (3.90) and equation (3.91):

$$c_1\cos(y_1)+c_2\cos(y_2) \leq |c_1|+|c_2|. \tag{3.92}$$

Thus, if we find a range of values of p that satisfies $|c_1|+|c_2| \leq 2$, equation (3.89) is also satisfied. Let us define the range for the p values considering $|p| \leq \frac{1}{2}$:

$$|c_1|+|c_2| \leq 2 \tag{3.93}$$

Since c_1 and c_2 are positive for $|p| \leq \frac{1}{2}$, we can avoid the absolute value notation:

$$\begin{aligned} c_1 + c_2 &\leq 2, \\ 1 + 2p + 1 - 2p &\leq 2, \\ 2 &\leq 2. \end{aligned} \tag{3.94}$$

That is feasible. Then, $|p| \leq \frac{1}{2}$ is a possible range in order for equation (3.86) to be satisfied.

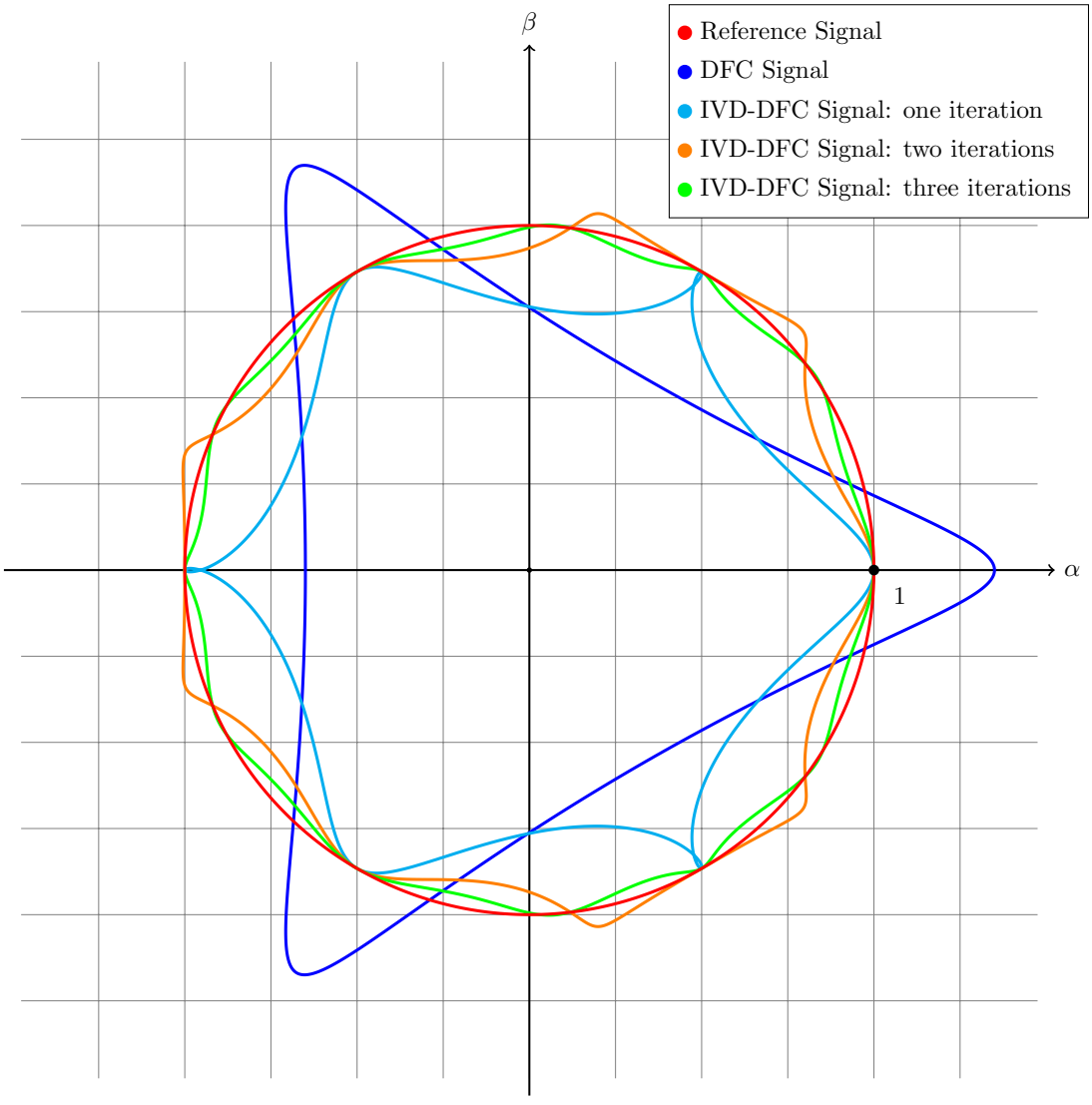

Figure 3.9: Plain representation of the DFC signals: $\frac{\Gamma_\alpha}{a}$ and $\frac{\Gamma_\beta}{a}$ respectively on the x and y axis (blue line). The red circle represents the signals for the case $b = 0$ and is taken as reference. The other lines are referring to certain numbers of iterations for the IVD-DFC algorithm (case with $p = 0.35$).

Thus, $|p| \leq \frac{1}{2}$ is a sufficient condition for equation (3.86). The case $\chi_1(x, \Delta_{k-1}) \leq 0$ can be manipulated as before and the result is the same. Then, $|p| \leq \frac{1}{2}$ is a possible range for equation (3.86) in order to be satisfied. Then, if we put together the necessary and sufficient conditions found, one can assert that:

$$\lim_{k\to\infty} |\tan(\Delta_k)| = 0, \quad \text{iff } |p| < \frac{1}{2}. \tag{3.95}$$

Thus, using the Lemma 1, we get:

$$\lim_{k\to\infty} |\Delta_k| = 0, \quad \text{iff } |p| < \frac{1}{2}. \tag{3.96}$$

□

The convergence of the algorithm has been proven for those machines whose p absolute value is smaller than a half. We can state that this requirement is achieved by the most part of the low power PMSMs. For values of p greater than 0.5 other approaches can be applied but they are not topic of this analysis. Since the maximal absolute value of Δ_k can be determined, the number of iterations can be chosen considering the maximal acceptable error for the position estimation.

3.3.3 Phase shift effect: Full IVD-DFC

Normally, the assumptions made about the inductance matrix and the rapidity of the DFC operations with respect to the machine mechanical behavior are satisfied. However, for some particular circumstances, for example the occurrence of magnetic field saturation due to currents, these assumptions cannot be considered true anymore. The analysis of the saturation effect on the estimation of the angular position has been presented by Grasso in [56]. According to this work, the expression presented in equation (3.6) does not correctly model the DFC signals behavior in case of magnetic field saturation or high speed operation. Therefore, a modified inductance matrix that considers this effect is introduced and the DFC signal vector $\mathbf{\Gamma}_{\alpha\beta}$ takes the following form:

$$\begin{aligned} \Gamma_\alpha &= -a(t)\cos(2\theta_e(t) + \varphi_a(t)) + b(t)\cos(4\theta_e(t) + \varphi_b(t)), \\ \Gamma_\beta &= a(t)\sin(2\theta_e(t) + \varphi_a(t)) + b(t)\sin(4\theta_e(t) + \varphi_b(t)), \end{aligned} \tag{3.97}$$

where the phase shifts $\varphi_a(t)$ and $\varphi_b(t)$ as well as the amplitudes $a(t)$ and $b(t)$ depend on the currents that are flowing through the windings and the rotor speed. Starting from this point, the time dependency of these parameters will be avoided for sake of readability. An estimation of the variable θ_e can be given by:

$$2\hat{\theta}_0 = -\arctan\left(\frac{\Gamma_\beta}{\Gamma_\alpha}\right) - \varphi_a. \tag{3.98}$$

The following mathematical elaboration can be done in order to find the deviation Δ_0. The process is similar to equation (3.13):

$$\begin{aligned}
2\hat{\theta}_0 &= -\arctan\left(\frac{a\sin(2\theta_e+\varphi_a)+b\sin(4\theta_e+\varphi_b)}{-a\cos(2\theta_e+\varphi_a)+b\cos(4\theta_e+\varphi_b)}\right)-\varphi_a \\
&= \arctan\left(\frac{a\sin(2\theta_e+\varphi_a)+b\sin(4\theta_e+\varphi_b)}{a\cos(2\theta_e+\varphi_a)-b\cos(4\theta_e+\varphi_b)}\right)-\varphi_a \\
&= \angle\left(ae^{j(2\theta_e+\varphi_a)}-be^{-j(4\theta_e+\varphi_b)}\right)-\varphi_a \\
&= 2\theta_e+\varphi_a+\angle\left(1-\frac{b}{a}e^{-j(6\theta_e+\varphi_a+\varphi_b)}\right)-\varphi_a \\
&= 2\theta_e+\arctan\left(\frac{-p\sin(6\theta_e+\varphi_a+\varphi_b)}{1-p\cos(6\theta_e+\varphi_a+\varphi_b)}\right) \\
&= 2\theta_e+\Delta_0.
\end{aligned} \tag{3.99}$$

Let us suppose that we know the parameter b, φ_a and φ_b, as before one can build the algorithm:

$$2\hat{\theta}_k = -\arctan\left(\frac{\Gamma_\beta-b\sin\left(4\hat{\theta}_{k-1}+\varphi_b\right)}{\Gamma_\alpha-b\cos\left(4\hat{\theta}_{k-1}+\varphi_b\right)}\right)-\varphi_a. \tag{3.100}$$

That is, for the first iteration:

$$\begin{aligned}
2\hat{\theta}_1 &= \arctan\left(\frac{a\sin(\theta_e+\varphi_a)+b\sin(4\theta_e+\varphi_b)-b\sin\left(4\hat{\theta}_0+\varphi_b\right)}{a\cos(2\theta_e+\varphi_a)-b\cos(4\theta_e+\varphi_b)+b\cos\left(4\hat{\theta}_0+\varphi_b\right)}\right)-\varphi_a \\
&= \angle\left(ae^{j(2\theta_e+\varphi_a)}-be^{-j(4\theta_e+\varphi_b)}+be^{-j\left(4\hat{\theta}_0+\varphi_b\right)}\right)-\varphi_a \\
&= 2\theta_e+\varphi_a+\angle\left(1-pe^{-j(6\theta_e+\varphi_a+\varphi_b)}+pe^{-j\left(4\hat{\theta}_0+x+\varphi_a+\varphi_b\right)}\right)-\varphi_a \\
&= 2\theta_e+\angle\left(1-pe^{-j(6\theta_e+\varphi_a+\varphi_b)}+pe^{-j(6\theta_e+2\Delta_0+\varphi_a+\varphi_b)}\right) \\
&= 2\theta_e+\angle\left(1+2p\sin(\Delta_0)\,e^{-j(6\theta_e+\Delta_0+\varphi_a+\varphi_b+\pi/2)}\right) \\
&= 2\theta_e+\Delta_1.
\end{aligned} \tag{3.101}$$

Thus:

$$\Delta_k = \arctan\left(\frac{-2p\sin(\Delta_{k-1})\cos(6\theta_e+\Delta_{k-1}+\varphi_a+\varphi_b)}{1-2p\sin(\Delta_{k-1})\sin(6\theta_e+\Delta_{k-1}+\varphi_a+\varphi_b)}\right). \tag{3.102}$$

The mathematics follows the same procedure as in the previous subsection. Using the theorem 1 we can prove the following limit:

$$\lim_{k\to\infty}|\Delta_k| = 0, \tag{3.103}$$

and:

$$\lim_{k\to\infty} 2\hat{\theta}_k = 2\theta_e. \tag{3.104}$$

Figure 3.10 shows the flowchart related to the IVD-DFC operations in case of saturation effect.

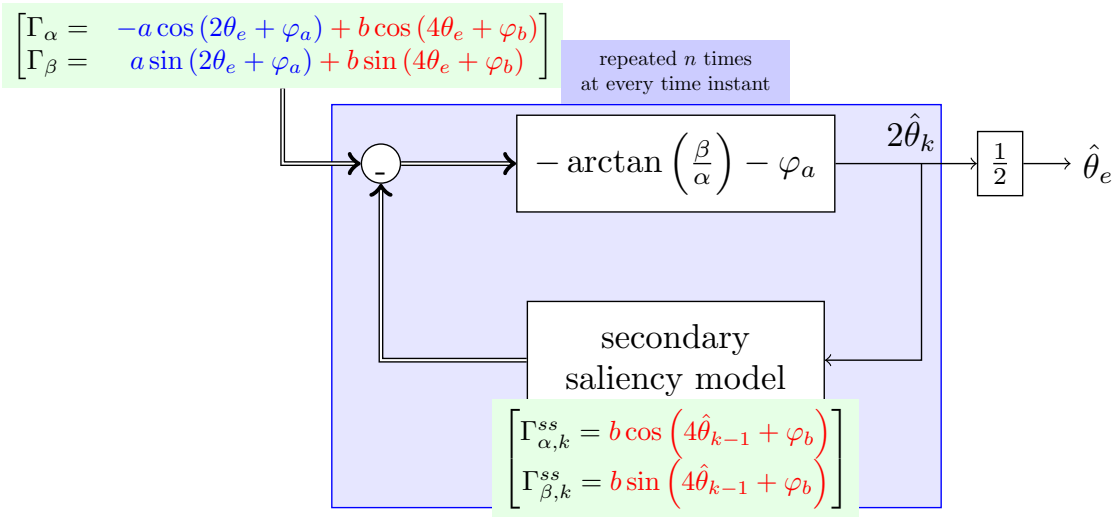

Figure 3.10: Flowchart of the IVD-DFC algorithm. The highlighted part in blue is the iterative part. It is assumed that the vector $\Gamma^{ss}_{\alpha,\beta}$ is a zero vector for k = 0.

3.3.4 Sensitivity Analysis

If the parameters b, φ_a and φ_b are not precisely known, the following algorithm can be proposed:

$$2\hat{\theta}_k = -\arctan\left(\frac{\Gamma_\beta - \hat{b}\sin\left(4\hat{\theta}_{k-1}+\hat{\varphi}_b\right)}{\Gamma_\alpha - \hat{b}\cos\left(4\hat{\theta}_{k-1}+\hat{\varphi}_b\right)}\right) - \hat{\varphi}_a. \tag{3.105}$$

The previous equation can be easily related to equation (3.100). The position information θ_e can be extracted from Equation (3.105) as presented in the previous subsections. After some mathematical elaborations we obtain:

$$2\hat{x}_k = 2\theta_e + \tilde{\varphi}_a + \arctan\left(\frac{-2p\sin(\Delta_{k-1}+\tilde{\varphi}_b)\cos(6\theta_e+\kappa_1)+\tilde{p}\sin(6\theta_e+\kappa_2)}{1-2p\sin(\Delta_{k-1}+\tilde{\varphi}_b)\sin(6\theta_e+\kappa_1)+\tilde{p}\cos(6\theta_e+\kappa_2)}\right), \tag{3.106}$$

where:

$$\begin{aligned}
\kappa_1 &= \varphi_a + \frac{\varphi_b + \hat{\varphi}_b}{2} + \Delta_{k-1}, \\
\kappa_2 &= \varphi_a + \hat{\varphi}_b + 2\Delta_{k-1}, \\
\tilde{p} &= \frac{b - \hat{b}}{a}, \\
\tilde{\varphi}_a &= \varphi_a - \hat{\varphi}_a, \\
\tilde{\varphi}_b &= \varphi_b - \hat{\varphi}_b,
\end{aligned} \tag{3.107}$$

where $\hat{b}$, $\hat{\varphi}_a$ and $\hat{\varphi}_b$ are respectively the estimated value of b, φ_a and φ_b. From equation (3.106), we cannot state that for increasing number of iterations the deviation term goes to zero. In fact, considering the results of Figure 3.11, a greater number of iterations does not imply a better convergence if the value p is too small. Figure 3.12 shows the deterioration of the performance due to the phase estimation error.

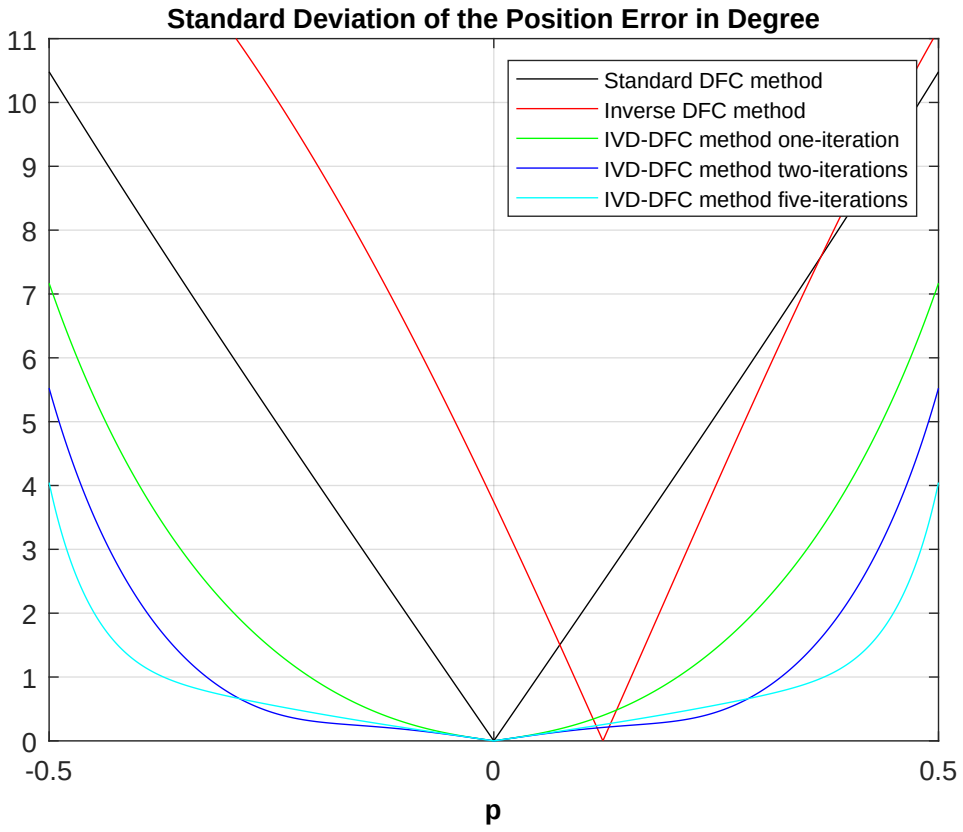

Figure 3.11: Comparison of the position standard deviation errors of the presented methods. The plot is referred to a machine with the following inductance values: $L_0 = 442.2$ µH, $M_0 = 20.7$ µH, $L_2 = 103.3$ µH. The parameter M_2 is let vary between $L_0 + M_0 - L_2$ and $L_0 - M_0 - L_2$ in order to get p range between -0.5 and 0.5. In this case $\hat{b}$ is 10% bigger than b.

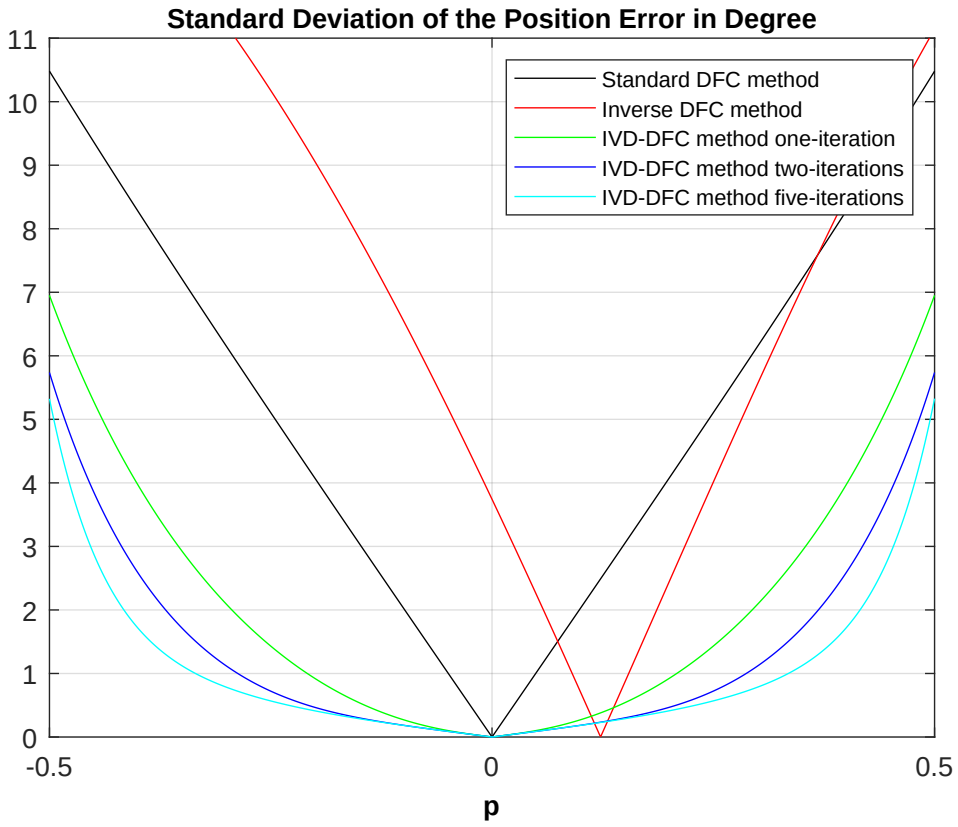

Figure 3.12: Comparison of the position standard deviation errors of the presented methods. The plot is referred to a machine with the following inductance values: $L_0 = 442.2$ µH, $M_0 = 20.7$ µH, $L_2 = 103.3$ µH. The parameter M_2 is let vary between $L_0 + M_0 - L_2$ and $L_0 - M_0 - L_2$ in order to get p range between -0.5 and 0.5. In this case $\hat{\varphi}_b$ differs from φ_b about 5 degrees.

For that reason, the parameter φ_a and φ_b should be estimated offline and their values should be saved in a look-up table depending on the current and speeds of the motor. The parameter p can be either estimated using an online or offline algorithm, as it will be shown within the next chapter.

3.4 Conclusions

Within this chapter, the estimation process of the angular rotor position by means of the DFC signals has been presented. As depicted in Figures 3.3 and 3.7, both standard and reverse DFC approaches introduce a systematic error dependent on the machine anisotropy. In the case of the standard approach, an analytical description of the DFC signals $\mathbf{\Gamma}_{\alpha\beta}$ can be given and, as shown in equation (3.6), they are the result of the combination of two terms: a second harmonic with magnitude a and a fourth harmonic with magnitude b. It has been proven that the systematic error on the position estimation is directly related to the magnitude of the fourth harmonic. The decrease in efficiency of the control algorithm due to the estimation error has been determined first mathematically and, then, through simulations. In order to

reduce the estimation error, the IVD-DFC algorithm has been proposed. This algorithm can improve the position estimation using an iterative approach based on the knowledge of the parameter b. Two additional parameters, namely φ_a and φ_b, are introduced to the IVD algorithm in order to consider the machine saturation effect leading to the Full-IVD algorithm depicted in Figure 3.10. The estimation results are satisfactory also in case of parameter deviation as depicted in Figures 3.11 and 3.12.

4 State Observation using the DFC

At this point, considering the results presented on the previous chapter, three issues arise:

- The possible deterioration of the DFC signals due to stochastic processes acting on them has not been considered yet.
- The DFC estimation might not perform as expected if high-speed operation is considered.
- The parameter b has to be estimated previously or simultaneously to the control operation in order for the IVD-DFC algorithm to perform correctly.

These issues can be handled by the introduction of a state observer. Within this chapter, the Kalman filter is presented as possible solution for the estimation of the machine mechanical state in presence of stochastic processes acting on the measurements. Moreover, the Kalman filter will be used also for the position and speed reconstruction for high-speed operations as well as for the estimation of the parameter b. Additionally, the observer can be used for the estimation of the external load-torque acting on the motor shaft in order to add more information about the system dynamic that could be possibly used for an improved motor control strategy. The Kalman filter has been chosen among other observers due to its optimal estimation capability for linear systems and its straightforward implementation on a microcontroller. Firstly, the mathematical description of the Kalman filter will be presented as well as its application to the machine equations. The observation process will be also widen to the nonlinear case and the concept of observation for high-speed operation will be presented. Afterwards, an additional observer, based on the Kalman filter structure, will be introduced in order to estimate the b parameter. Eventually, the observed state will be extended in order to include the external load torque.

4.1 Optimal state observation

A brief introduction to the Kalman filter concept and its application to the PMSM equations is presented in this section. The derivation of the observer equations are obtained considering a discrete time domain. Firstly, let us consider the following linear state space model in the continuous time domain:

$$\dot{\mathbf{x}}(t) = \mathbf{A}\mathbf{x}(t) + \mathbf{B}\mathbf{u}(t) + \mathbf{w}_c(t), \tag{4.1}$$

where $\mathbf{x}(t) \in \mathbb{R}^n$ is the state vector containing the n time dependent variables of the system, $\mathbf{u}(t) \in \mathbb{R}^m$ is the vector including the m input signals acting on the state, $\mathbf{A} \in \mathbb{R}^{n\times n}$, $\mathbf{B} \in \mathbb{R}^{m\times n}$ are respectively the state and the input matrix of the system and $\mathbf{w}_c(t) \in \mathbb{R}^n$ is a vector

containing the disturbances and the unmodelled dynamics acting on the system. Let us now discretize equation (4.1) considering the forward Euler method approximation:

$$\frac{\mathbf{x}\left(\left(k+1\right)T\right)-\mathbf{x}\left(kT\right)}{T}=\mathbf{A}\mathbf{x}\left(kT\right)+\mathbf{B}\mathbf{u}\left(kT\right)+\mathbf{w}_c\left(kT\right), \tag{4.2}$$

which becomes:

$$\mathbf{x}\left(\left(k+1\right)T\right)=\mathbf{F}\mathbf{x}\left(kT\right)+\mathbf{G}\mathbf{u}\left(kT\right)+\mathbf{w}\left(kT\right), \tag{4.3}$$

where:

$$\begin{aligned}&\mathbf{F}=\mathbf{I}+T\mathbf{A},\\&\mathbf{G}=T\mathbf{B},\\&\mathbf{w}\left(kT\right)=T\mathbf{w}_c\left(kT\right),\\&k\in\mathbb{N},\end{aligned} \tag{4.4}$$

where T is the discretization step and kT is the time instant considered. Let us now introduce the measurement vector $\mathbf{y}\left(kT\right)\in\mathbf{R}^p$:

$$\mathbf{y}\left(kT\right)=\mathbf{H}\mathbf{x}\left(kT\right)+\mathbf{v}\left(kT\right), \tag{4.5}$$

where $\mathbf{H}\in\mathbb{R}^{p\times n}$ and $\mathbf{v}\left(kT\right)$ represents the noise vector acting on the measurements. Finally, the dynamic model can be defined in the following reduced form:

$$\begin{aligned}\mathbf{x}_{k+1}&=\mathbf{F}\mathbf{x}_k+\mathbf{G}\mathbf{u}_k+\mathbf{w}_k,\\\mathbf{y}_k&=\mathbf{H}\mathbf{x}_k+\mathbf{v}_k.\end{aligned} \tag{4.6}$$

The disturbance vectors $\mathbf{w}_k$ and $\mathbf{v}_k$ are generally considered stochastical processes and their behavior can be described by their correlation matrix $\mathbf{Q}$ and $\mathbf{R}$ and their mean values $\boldsymbol{\mu}_w$ and $\boldsymbol{\mu}_v$:

$$\begin{aligned}\boldsymbol{\mu}_w(k)&=E\left[\mathbf{w}_k\right]=\frac{1}{k}\sum_{i=0}^{k}\mathbf{w}_i,\\\mathbf{Q}_k&=E\left[\left(\mathbf{w}_k-\boldsymbol{\mu}_w\right)\left(\mathbf{w}_k-\boldsymbol{\mu}_w\right)^T\right]=\frac{1}{k}\sum_{i=0}^{k}\left(\mathbf{w}_i-\boldsymbol{\mu}_w\right)\left(\mathbf{w}_i-\boldsymbol{\mu}_w\right)^T,\end{aligned} \tag{4.7}$$

for the process $\mathbf{w}_k$ and:

$$\begin{aligned}\boldsymbol{\mu}_v(k)&=E\left[\mathbf{v}_k\right]=\frac{1}{k}\sum_{i=0}^{k}\mathbf{v}_i,\\\mathbf{R}_k&=E\left[\left(\mathbf{v}_k-\boldsymbol{\mu}_v\right)\left(\mathbf{v}_k-\boldsymbol{\mu}_v\right)^T\right]=\frac{1}{k}\sum_{i=0}^{k}\left(\mathbf{v}_i-\boldsymbol{\mu}_v\right)\left(\mathbf{v}_i-\boldsymbol{\mu}_v\right)^T.\end{aligned} \tag{4.8}$$

Considering the system equations (4.6), the only information about its state $\mathbf{x}_k$ comes from the measurement vector $\mathbf{y}_k$. Thus, an observer can be implemented in order to extract the information about the system state by the exploitation of the measurement vector. That

is a feasible request, if the pair $(\mathbf{F}, \mathbf{H})$ fulfills the observability criterion. Indeed, several observers structures and approaches could be used in order to perform an estimation of the state $\mathbf{x}$ but only the Kalman filter and all its various derivations are based on an optimization process that consider the stochastic processes acting on the model equations and on the measurements.

4.1.1 Kalman filter for PMSMs

Let us recall the PMSM differential equation presented in (2.10) in the discretized form:

$$\begin{aligned} \omega_e(k+1) &= \omega_e(k) + \frac{T}{J}\left(-B\omega_e(k) + \Xi_e(k) - \Xi_l(k)\right) + w_\omega(k), \\ \theta_e(k+1) &= \theta_e(k) + T\omega_e(k) + w_\theta(k), \end{aligned} \tag{4.9}$$

where the differential equation relative to the angular position has been added. Momentarily, the external load torque term $\Xi_l(k)$ will be neglected. The system can be described in a reduced form as in equation (4.6) by definition of the following quantities:

$$\begin{aligned} &\mathbf{x}_k = \begin{bmatrix} \omega_e(k) \\ \theta_e(k) \end{bmatrix}, \quad u_k = \Xi_e(k), \quad \mathbf{w}_k = \begin{bmatrix} w_\omega(k) \\ w_\theta(k) \end{bmatrix}, \\ &\mathbf{F} = \begin{bmatrix} 1 - \dfrac{TB}{J} & 0 \\ T & 1 \end{bmatrix}, \quad \mathbf{G} = \begin{bmatrix} \dfrac{T}{J} \\ 0 \end{bmatrix}. \end{aligned} \tag{4.10}$$

Temporarily, we suppose that the position is directly measurable:

$$y_k = \theta_e(k) + v_\theta(k), \tag{4.11}$$

thus:

$$\mathbf{H} = \begin{bmatrix} 0 & 1 \end{bmatrix}, \quad v_k = v_\theta(k). \tag{4.12}$$

Let us now define the estimation state variable $\hat{\mathbf{x}}_k$ and its covariance matrix $\mathbf{P}_k$:

$$\mathbf{P}_k = E\left[\left(\mathbf{x}_k - \hat{\mathbf{x}}_k\right)\left(\mathbf{x}_k - \hat{\mathbf{x}}_k\right)^T\right] = \frac{1}{k}\sum_{i=0}^{k}\left(\mathbf{x}_k - \hat{\mathbf{x}}_k\right)\left(\mathbf{x}_k - \hat{\mathbf{x}}_k\right)^T = \frac{1}{k}\sum_{i=0}^{k}\tilde{\mathbf{x}}_k\tilde{\mathbf{x}}_k^T, \tag{4.13}$$

where the term $\tilde{\mathbf{x}}_k = \mathbf{x}_k - \hat{\mathbf{x}}_k$ represents the estimation error. We can define the dynamic of the estimated state $\hat{\mathbf{x}}_k$ in order to match the dynamic of the PMSM in (4.9), obviously the process noise $\mathbf{w}_k$ cannot be included:

$$\hat{\mathbf{x}}_{k+1} = \mathbf{F}\hat{\mathbf{x}}_k + \mathbf{G}u_k. \tag{4.14}$$

We can now introduce the Kalman filter estimation process. Its operations can be mainly divided into two tasks: prediction and update. The prediction can be summarized in the following steps:

- at time k the old estimated state $\hat{\mathbf{x}}_{k-1}^-$ evolves into the new predicted state $\hat{\mathbf{x}}_k^-$ using the

model equations in equation (4.14):

$$\hat{\mathbf{x}}_k^- = \mathbf{F}\hat{\mathbf{x}}_{k-1}^- + \mathbf{G}u_{k-1}, \tag{4.15}$$

- similarly the covariance matrix $\mathbf{P}_k$ is propagated through the matrix $\mathbf{F}$:

$$\mathbf{P}_k^- = \mathbf{F}^T\mathbf{P}_{k-1}^-\mathbf{F} + \mathbf{Q}_k. \tag{4.16}$$

The update makes use of the measurement vector $\mathbf{y}_k$ in order to correct the previous prediction of the state. The update operations can be defined as follows:

- the Kalman filter gain matrix is calculated:

$$\mathbf{K}_k = \mathbf{P}_k^-\mathbf{H}^T\left(\mathbf{H}\mathbf{P}_k^-\mathbf{H}^T + R_k\right)^{-1}, \tag{4.17}$$

- the covariance matrix $\mathbf{P}_k^-$ is updated:

$$\mathbf{P}_k^+ = \left(\mathbf{I} - \mathbf{K}_k\mathbf{H}\right)\mathbf{P}_k^-, \tag{4.18}$$

- the estimated state $\hat{\mathbf{x}}_k^-$ is updated:

$$\hat{\mathbf{x}}_k^+ = \hat{\mathbf{x}}_k^- + \mathbf{K}_k\bar{y}_k, \tag{4.19}$$

where:

$$\bar{y}_k = y_k - \mathbf{H}\hat{\mathbf{x}}_k^-, \tag{4.20}$$

is called the innovation term.

At this point the estimation process can move on the next step $k+1$, the following relations hold:

$$\hat{\mathbf{x}}_{k+1}^- = \hat{\mathbf{x}}_k^+, \quad \mathbf{P}_{k+1}^- = \mathbf{P}_k^+. \tag{4.21}$$

The calculation of the gain matrix $\mathbf{K}_k$ in equation (4.17) allows the observer to perform a minimization of the the covariance matrix $\mathbf{P}_k$. Accordingly to [57], the Kalman filter results to be the best linear observer that minimize the matrix $\mathbf{P}_k$ if the stochastic processes $\mathbf{w}_k$ and $\mathbf{v}_k$ are zero-mean, uncorrelated and white. These assumptions are not always applicable to the considered dynamical system, however, some modifications to the observer structure can be made in order to generalize its optimal behavior to a wider class of systems. In case an encoder is used for the measurement of the angular position, the covariance value R_k of the measurement is usually approximated to:

$$R_k = \frac{1}{2^{N_{bit}}}, \tag{4.22}$$

where N_{bit} is the number of bits available to the encoder that determine the resolution of the measurement. Instead, considering a sensorless technique, the definition of a value for

the measurement covariance might be more difficult. For example, if the DFC vector $\mathbf{\Gamma}_{\alpha\beta}$ is considered, we can define the measurement signal y_k as:

$$y_k = -\frac{1}{2}\operatorname{atan}\left(\frac{\Gamma_\beta(k)}{\Gamma_\alpha(k)}\right) = \theta_e(k) + v_\theta(k). \tag{4.23}$$

Without loss of generality, the parameter b is temporarily taken equal to zero and the terms $\Gamma_\alpha(k)$ and $\Gamma_\beta(k)$ are affected by white noise with the same covariance $\sigma^2_{v_\Gamma}$. Let us recall the propagation of uncertainties through the $\operatorname{atan}(\cdot)$ function. If we consider a variable X with associated variance σ^2_X, we can assert, referring to INS REF, that the new variable Y defined as:

$$Y = -\frac{1}{2}\operatorname{atan}(X) \tag{4.24}$$

presents the following variance:

$$\sigma^2_Y = \frac{1}{4}\left(\frac{1}{X^2+1}\right)^2 \sigma^2_X. \tag{4.25}$$

Moreover, considering the variable X defined as:

$$X = \frac{B}{A}, \tag{4.26}$$

and considering the variable A and B uncorrelated, we can state that the variance σ^2_X is equal to:

$$\sigma^2_X = \left(\frac{B}{A}\right)^2\left[\left(\frac{\sigma_A}{A}\right)^2 + \left(\frac{\sigma_B}{B}\right)^2\right]. \tag{4.27}$$

Substituting (4.27) in (4.25), we obtain:

$$\sigma^2_Y = \frac{1}{4}\left(\frac{1}{\left(\frac{B}{A}\right)^2+1}\right)^2\left(\frac{B}{A}\right)^2\left[\left(\frac{\sigma_A}{A}\right)^2 + \left(\frac{\sigma_B}{B}\right)^2\right] = \frac{1}{4}\left(\frac{AB}{A^2+B^2}\right)^2\left[\frac{\sigma^2_A B^2 + \sigma^2_B A^2}{A^2B^2}\right] = \\ = \frac{1}{4}\left(\frac{\sigma^2_A B^2 + \sigma^2_B A^2}{\left(A^2+B^2\right)^2}\right). \tag{4.28}$$

Now, if we consider $A = \Gamma_\alpha(k)$, $B = \Gamma_\beta(k)$, $\sigma^2_A = \sigma^2_B = R_\Gamma$, $Y = y_k$ and R_k the covariance of $v_\theta(k)$, we can write:

$$R_k = \frac{1}{4}\frac{\sigma^2_{v_\Gamma}}{\Gamma^2_\alpha(k) + \Gamma^2_\beta(k)}. \tag{4.29}$$

Reminding the definition of the DFC signals in equation (3.6) and that by assumption $b = 0$, we obtain:

$$R_k = \frac{\sigma^2_{v_\Gamma}}{4a^2}. \tag{4.30}$$

Instead, if we consider $b \neq 0$, we obtain:

$$R_k = \frac{\sigma^2_{v_\Gamma}}{4} \frac{1}{a^2 + b^2 + ab\sin(2\theta_e(k))}. \tag{4.31}$$

As shown, the introduction of the term b let the estimation to be affected by a deterministic error whose mathematical description has been already presented in equation (3.13). Thus, we can rewrite the measurement variable y_k as:

$$y_k = \theta_k + \frac{\Delta(k)}{2} + v_\theta(k), \tag{4.32}$$

where the covariance of $v_\theta(k)$ is R_k and:

$$\Delta(k) = \operatorname{atan}\left(\frac{\frac{b}{a}\sin(6\theta_e(k))}{1 - \frac{b}{a}\cos(6\theta_e(k))}\right). \tag{4.33}$$

It is clear from the previous equations that the position measurement obtained using the DFC technique is not only affected by a noise process with a determinable covariance but it is also affected by a systematic error dependent on the parameter b. If $b \neq 0$, the Kalman filter cannot perform the optimal estimation as expected. In order to resolve this issue, we might think of using directly the DFC signals vector $\mathbf{\Gamma}_{\alpha\beta}$ as measurement instead of using the arctangent function:

$$\mathbf{y}_k = \mathbf{\Gamma}_{\alpha\beta}(k). \tag{4.34}$$

However, the nonlinearity relations between the vector $\mathbf{\Gamma}_{\alpha\beta}$ and the angular position θ_e cannot be handled by the proposed linear observer. In the following subsection, the Kalman filter will be extended for the nonlinear case.

4.1.2 Direct application to the DFC measurements: extended Kalman filter

As shown, the Kalman filter represents the best choice among linear observers capable of minimizing the covariance matrix $\mathbf{P}_k$. Nevertheless, there are various modifications that can be done in order to extend its range of applicability to nonlinear systems. The most straightforward one is to linearize the model and apply the same procedure shown before to the linearized system. This approach is called the Extended Kalman Filter (EKF). In our case, only the measurement vector $\mathbf{y}_k$ becomes a nonlinear function of the state, instead, the system model remains linear:

$$\mathbf{y}_k = \begin{bmatrix}\Gamma_\alpha(k)\\ \Gamma_\beta(k)\end{bmatrix} = \begin{bmatrix}-a\cos(2\theta_e(k)) + b\cos(4\theta_e(k))\\ a\sin(2\theta_e(k)) + b\sin(4\theta_e(k))\end{bmatrix}. \tag{4.35}$$

Thus, only the linearization of $\mathbf{y}_k$ is needed. The EKF procedure is similar to the linear case. The prediction part follows the same steps of the previous case since the state dynamic remains linear. The update part can be defined by the following steps:

- The matrix $\mathbf{H}_k$ is obtained by substituting the estimated state $\hat{\mathbf{x}}_k^-$ into the first order partial derivative of the measurement vector $\mathbf{y}_k$ performed with respect to $\mathbf{x}_k$:

$$\mathbf{H}_k = \left.\frac{\partial \mathbf{y}_k}{\partial \mathbf{x}_k}\right|_{\mathbf{x}_k=\hat{\mathbf{x}}_k^-} = \begin{bmatrix} 2a\sin\left(2\hat{\theta}_e^-(k)\right) - 4b\sin\left(4\hat{\theta}_e^-(k)\right) \\ 2a\cos\left(2\hat{\theta}_e^-(k)\right) + 4b\cos\left(4\hat{\theta}_e^-(k)\right) \end{bmatrix}, \tag{4.36}$$

- the Kalman filter gain matrix is calculated:

$$\mathbf{K}_k = \mathbf{P}_k^-\mathbf{H}_k^T\left(\mathbf{H}\mathbf{P}_k^-\mathbf{H}_k^T + \mathbf{R}_k\right)^{-1}, \tag{4.37}$$

  where:

$$\mathbf{R}_k = \begin{bmatrix} \sigma_{v_\Gamma}^2 & 0 \\ 0 & \sigma_{v_\Gamma}^2 \end{bmatrix}, \tag{4.38}$$

- the covariance matrix $\mathbf{P}_k^-$ is updated:

$$\mathbf{P}_k^+ = \left(\mathbf{I} - \mathbf{K}_k\mathbf{H}_k\right)\mathbf{P}_k^-, \tag{4.39}$$

- the estimated state $\hat{\mathbf{x}}_k^-$ is updated:

$$\hat{\mathbf{x}}_k^+ = \hat{\mathbf{x}}_k^- + \mathbf{K}_k\bar{\mathbf{y}}_k, \tag{4.40}$$

  where:

$$\bar{\mathbf{y}}_k = \mathbf{y}_k - \hat{\mathbf{y}}_k = \begin{bmatrix} \Gamma_\alpha(k) \\ \Gamma_\beta(k) \end{bmatrix} - \begin{bmatrix} -a\cos\left(2\hat{\theta}_e(k)\right) + b\cos\left(4\hat{\theta}_e(k)\right) \\ a\sin\left(2\hat{\theta}_e(k)\right) + b\sin\left(4\hat{\theta}_e(k)\right) \end{bmatrix}. \tag{4.41}$$

It has to be remarked that the EKF algorithm could give better estimation results with respect to the linear case only if the DFC signals are correctly modeled and the parameters a and b are exactly known. Moreover, this approach could potentially substitute the IVD-DFC algorithm since the fourth anisotropy harmonics are already included into the model. Nevertheless, the ideal case is almost never satisfied and the *a priori* knowledge of the parameter a and b is not a straightforward request to be fulfilled. In fact, a possibility, in order to estimate the parameters, is to apply the Fast Fourier Transform (FFT) to the DFC signals Γ_α and Γ_β when the motor is rotating. However, this solution requests a great amount of computational effort and requires ideally a constant angular speed. For that reason, within the next section, a combination of the IDV-DFC algorithm with an online parameter estimation method will be presented as alternative to the EKF.

4.1.3 Adaptive observer for sensorless high-speed operation

To this point, the DFC signals are still considered independent to the motor speed. In fact, as described in Chapter 2, the extraction of the DFC measurement vector is performed at

a PWM frequency whose bandwidth can be considered much higher than the mechanical one. Although it is reasonable to avoid the deterioration of the position estimation due to the speed effects for a more simple mathematical derivation of the DFC theory, these effects cannot be avoided if we consider the motor operation at high-speed. Moreover, it is also to be considered that a complete DFC signal vector is available every three PWM periods and within these the motor position could change noticeably. This effect is called the sequentiality effect and it is fully described in INS REF.
Clearly, if we suppose to have a good model of the system dynamics at high-speed, we can apply the Kalman filter or the EKF with a modified value of $\sigma^2_{v_\Gamma}$, for example:

$$\sigma^2_{v_{\Gamma_{lin}}}(k) = \begin{cases} \sigma^2_{v_\Gamma} & \text{for} \quad |\hat{\omega}_e(k)| \leq \omega_f \\ \sigma^2_{v_\Gamma} + m\left(|\hat{\omega}_e(k)| - \omega_f\right) & \text{for} \quad |\hat{\omega}_e(k)| > \omega_f \end{cases}, \tag{4.42}$$

or:

$$\sigma^2_{v_{\Gamma_{quad}}}(k) = \sigma^2_{v_\Gamma} + m_2|\hat{\omega}_e(k)|^2, \tag{4.43}$$

where $\omega_f > 0$, $m > 0$ and $m_2 > 0$. The previous examples are only two of the theoretically infinite possible combinations of polynomial functions with variable $\hat{\omega}_e(k)$. Even more examples can be implemented if we consider nonlinear functions. Obviously, the coefficients used must be tuned accordingly to the desired performance. A greater value of m_2, for example, will increase the covariance term more rapidly as the estimated speed increases. That will result into an estimation that relies more on the model prediction than on the measurements. Thus, at least for high-speed operation, the dynamical behavior of the machine should be accurately modeled.

4.1.4 Load torque estimation

As declared at the beginning of this section, the external load-torque Ξ_l has not been taken into account for the development of the observer. However, its contribution to the system dynamic is fundamental because every external mechanical interaction is accountable for the evolution of the system state. Since the external load torque is mostly unpredictable, it is almost impossible to provide a dynamical description of its behavior. Hence, the best model for its dynamic is to put its derivative to zero:

$$\frac{\mathrm{d}\Xi_l(t)}{\mathrm{d}t} = 0, \quad \Xi_l(0) = 0, \tag{4.44}$$

that for the discretized system is equal to:

$$\Xi_l(k+1) = \Xi_l(k), \quad \Xi_l(0) = 0. \tag{4.45}$$

Obviously, the previous relation does not bring any disposable information but, if embedded into the Kalman filter equations, an estimation of the external load torque can be obtained.

In fact, by means of an extended state definition:

$$\mathbf{x}_k = \begin{bmatrix} \omega_e(k) \\ \theta_e(k) \\ \Xi_l(k) \end{bmatrix}. \tag{4.46}$$

The resulting model used for the state prediction is as before:

$$\hat{\mathbf{x}}_k^- = \mathbf{F}\hat{\mathbf{x}}_{k-1}^- + \mathbf{G}u_{k-1}, \tag{4.47}$$

and the matrices $\mathbf{F}$ and $\mathbf{G}$ are also extended:

$$\mathbf{F} = \begin{bmatrix} 1 - \frac{TB}{J} & 0 & -\frac{T}{J} \\ T & 1 & 0 \\ 0 & 0 & 1 \end{bmatrix}, \quad \mathbf{G} = \begin{bmatrix} \frac{T}{J} \\ 0 \\ 0 \end{bmatrix}. \tag{4.48}$$

Considering equation (4.45), the prediction still does not contribute to a rational estimation of the $\Xi_l(k)$. However, the covariance matrix $\mathbf{P}_k$ will be processed as well as in equation (4.16) and its prediction will be used for the calculation of the observer gain $\mathbf{K}_k$ that, by means of the innovation term $\bar{\mathbf{y}}_k$, will generate a new estimation value of $\Xi_l(k)$. Therefore, the matrix $\mathbf{P}_k$ plays a decisive role on the determination of the new estimated state. Considering equation (4.16), the evolution of the propagated matrix $\mathbf{P}_k$ through $\mathbf{F}$ is determined by the choice of the new covariance matrix $\mathbf{Q}_k$, that for simplicity will be considered independent on time and diagonal:

$$\mathbf{Q}_k = \begin{bmatrix} \sigma_{w_\omega}^2 & 0 & 0 \\ 0 & \sigma_{w_\theta}^2 & 0 \\ 0 & 0 & \sigma_{w_\Xi}^2 \end{bmatrix}. \tag{4.49}$$

Hence, by a balanced choice of the matrix entries, one can determine the dynamic of the estimation process. An ideal definition of the matrix $\mathbf{Q}_k$ might be:

$$\mathbf{Q}_k = \begin{bmatrix} q_\omega & 0 & 0 \\ 0 & 0 & 0 \\ 0 & 0 & +\infty \end{bmatrix}, \tag{4.50}$$

since the position model can be considered perfect and the external load totally unknown. The value q_ω can be chosen depending on the accuracy of the model proposed for the speed evolution.

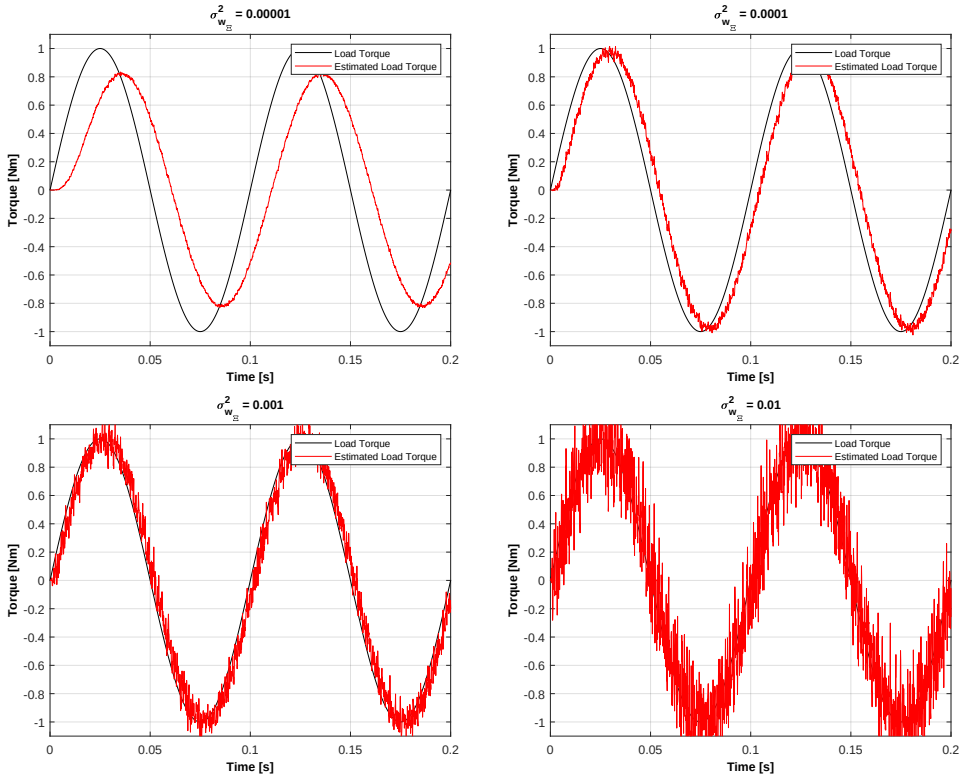

Figure 4.1: Simulations of the load torque estimation using the linear Kalman filter by posing $\sigma^2_{w_\omega} = 1$ and $\sigma^2_{w_\omega} = 0$. A sinusoidal external load torque with frequency 10 Hz and amplitude 1 Nm is generated at the motor shaft. The DFC signals are simulated with $R_\Gamma = 0.0001$, $a = 1$ and $b = 0$.

Obviously, the previous matrix cannot feasibly be implemented on a digital system, therefore, a finite value of $\sigma^2_{w_\Xi}$ has to be chosen. It can be proven experimentally that a greater value of $\sigma^2_{w_\Xi}$ increases the bandwidth of the estimation, thus, a faster and more jittery response is generated. Theoretically, an infinite value as in equation (4.50) let the observer behave like a derivator. Instead, a smaller value of $\sigma^2_{w_\Xi}$ smooths the estimation acting as a low-pass filter but the observer would become unresponsive at high frequencies. In Figure 4.1 the behavior of the load torque estimation is simulated for different values of $\sigma^2_{w_\Xi}$.

4.2 Online parameter estimation for the IVD-DFC algorithm

The introduction of the DFC signals Γ_α and Γ_β as direct measurements within the EKF equations allows theoretically the elimination of the systematic error Δ. Then, as said in the previos section, the use of the EKF could potentially substitute the IVD-DFC algorithm. However, it has to be remarked that the model presented in equation (3.6) is obtained considering ideal assumptions, thus, the estimation might be negatively influenced by potential uncertainties and unmodeled dynamics. Furthermore, the parameter values a and b have to be previously identified and the identification process is not a straightforward task for this specific case. For that reason, this section presents a Recursive Least Square (RLS) estima-

tion algorithm for the parameters a and b. Firstly, the algorithm will be presented considering an ideal disposable angular position, for example, obtained using an encoder. Then, the same identification process will be combined with the IVD-DFC algorithm. A performance comparison of these two approaches will be presented by means of simulation results.

4.2.1 Recursive Least Square estimation for a and b

The RLS algorithm implemented for the estimation of the parameters a and b is basically derived from the update section of the Kalman filter. Let us recall the discrete time model of the DFC signals in (3.6):

$$\mathbf{\Gamma}_{\alpha\beta} = \begin{bmatrix} \Gamma_\alpha \\ \Gamma_\beta \end{bmatrix} = \begin{bmatrix} -a\cos(2\theta_e(k)) + b\cos(4\theta_e(k)) \\ a\sin(2\theta_e(k)) + b\sin(4\theta_e(k)) \end{bmatrix}. \tag{4.51}$$

Starting from them, we can define the estimated DFC signals as follows:

$$\hat{\mathbf{\Gamma}}_{\alpha\beta} = \begin{bmatrix} \hat{\Gamma}_\alpha \\ \hat{\Gamma}_\beta \end{bmatrix} = \begin{bmatrix} -\hat{a}(k)\cos(2\theta_e(k)) + \hat{b}(k)\cos(4\theta_e(k)) \\ \hat{a}(k)\sin(2\theta_e(k)) + \hat{b}(k)\sin(4\theta_e(k)) \end{bmatrix}. \tag{4.52}$$

We assume that the position $\theta_e(k)$ is perfectly known. Then, we define:

$$\mathbf{P}_{rls} = \begin{bmatrix} p_{11} & 0 \\ 0 & p_{22} \end{bmatrix}, \quad \mathbf{R}_{rls} = \begin{bmatrix} R_\Gamma & 0 \\ 0 & R_\Gamma \end{bmatrix}, \quad \mathbf{x}_k = \begin{bmatrix} a \\ b \end{bmatrix}, \quad \hat{\mathbf{x}}_k = \begin{bmatrix} \hat{a}(k) \\ \hat{b}(k) \end{bmatrix}, \tag{4.53}$$

and

$$\mathbf{H}_k = \frac{\partial \mathbf{\Gamma}_{\alpha\beta}}{\partial \mathbf{x}_k} = \begin{bmatrix} -\cos(2\theta_e) & \cos(4\theta_e) \\ \sin(2\theta_e) & \sin(4\theta_e) \end{bmatrix}. \tag{4.54}$$

The RLS takes the following steps:

- determination of the gain matrix:

$$\mathbf{K}_k = \mathbf{P}_{rls}\mathbf{H}_k^T \left(\mathbf{H}_k\mathbf{P}_{rls}\mathbf{H}_k^T + \mathbf{R}_{rls}\right)^{-1}, \tag{4.55}$$

- calculation of the innovation vector:

$$\bar{\mathbf{\Gamma}}_{\alpha\beta} = \mathbf{\Gamma}_{\alpha\beta} - \hat{\mathbf{\Gamma}}_{\alpha\beta}, \tag{4.56}$$

- correction of the estimation vector $\hat{\mathbf{x}}_k^-$:

$$\hat{\mathbf{x}}_k^+ = \hat{\mathbf{x}}_k^- + \mathbf{K}_k\bar{\mathbf{\Gamma}}_{\alpha\beta}. \tag{4.57}$$

The values p_{11} and p_{22} are parameters that can be tuned accordingly to the desired performance of the estimation. In Figure 4.2 the simulation results of the estimation are shown for different value of p_{11} and p_{22}. Clearly, the assumption of a perfect position knowledge is not rational because we are interested in the estimation of a and b in order to get an improved position estimation from the EKF. One possibility is to estimate the parameters using the

position information from an encoder when the motor is not in service. However, that is not a clever solution because it forces the use of a mechanical sensor. Thus, the implementation of the EKF with the direct employment of the DFC signals as measurements could be impracticable for most applications. A possible solution to this issue is presented within the next subsection.

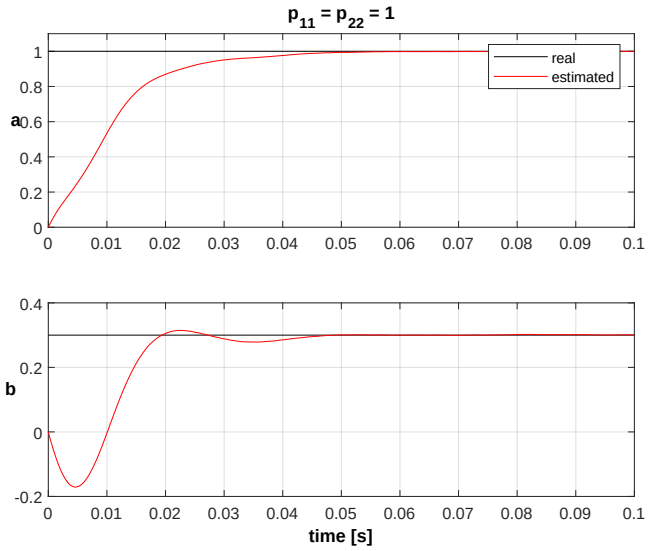

Figure 4.2: Simulation results of the estimation of the parameter a and b using the RLS algorithm. In this case, the simulated DFC signals have $a = 1$ and $b = 0.3$.

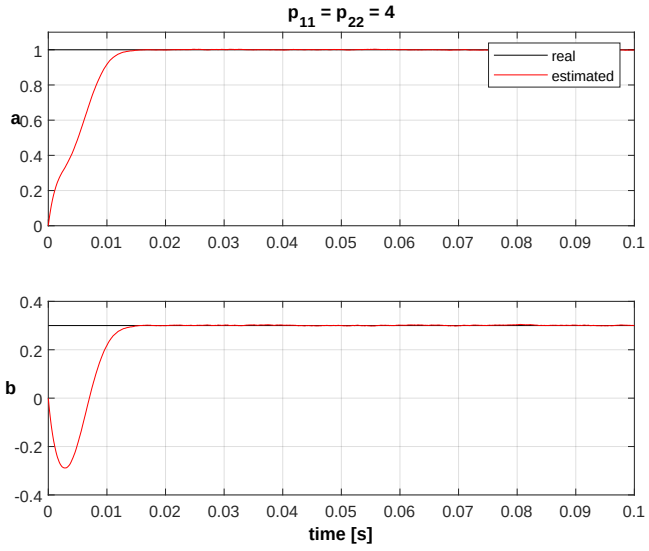

Figure 4.3: Simulation results of the estimation of the parameter a and b using the RLS algorithm. In this case, the simulated DFC signals have $a = 1$ and $b = 0.3$.

4.2.2 RLS / IVD-DFC combination

An idea for the improvement of the estimation process is to use the linear Kalman filter by means of the IVD-DFC position as measurement instead of the standard DFC one. The IVD-DFC needs only the knowledge of the parameter b in order to be properly performed. For that reason, the RLS can be added to the estimation chain as shown in Figure 4.4. This combination forms a closed loop path which could potentially lead the system to instability. Although a complete stability analysis could not be given yet, the functioning principle of this new algorithm can be proven through simulations and experimental results as shown in the next figures.

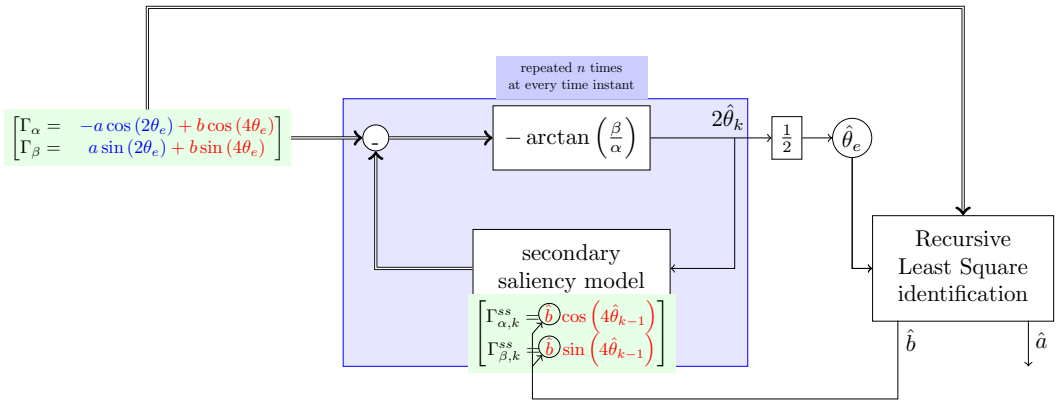

Figure 4.4: Schematic of the IVD-DFC/RLS combination. The estimated position $\hat{\theta}_e$ is passed to the linear Kalman filter as measurement.

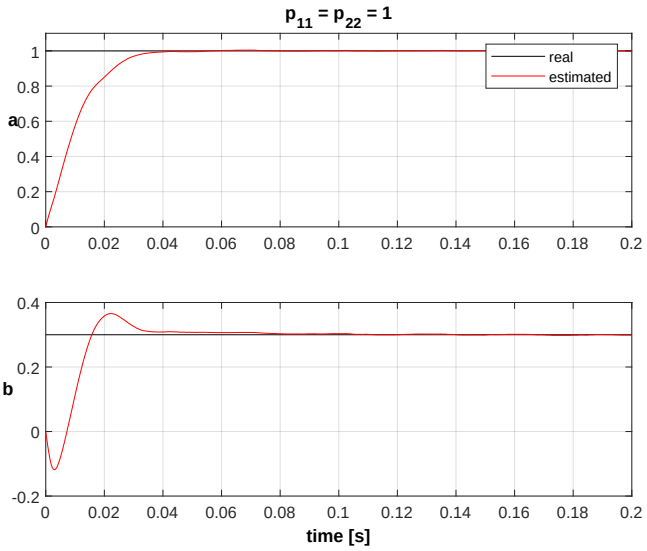

Figure 4.5: Simulation results of the estimation of the parameter a and b using the IVD-DFC/RLS combination. In this case, the simulated DFC signals have $a = 1$ and $b = 0.3$.

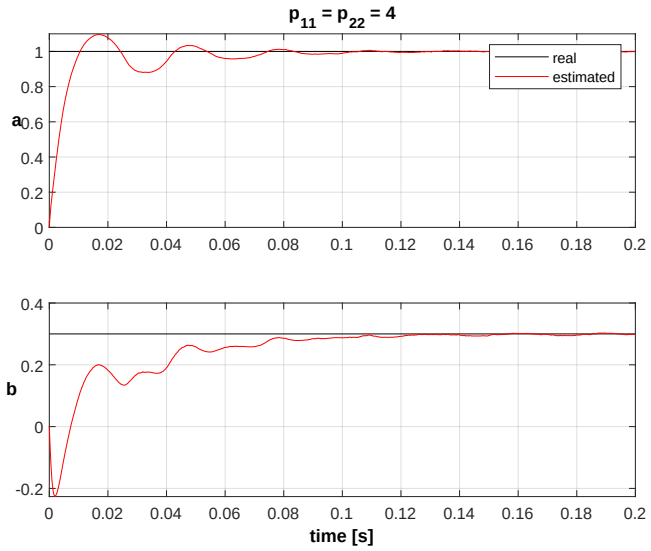

Figure 4.6: Simulation results of the estimation of the parameter a and b using the IVD-DFC/RLS combination. In this case, the simulated DFC signals have $a = 1$ and $b = 0.3$.

In Figures 4.5 and 4.6 the estimation of the parameters a and b are shown when considering the combination of the RLS and IVD-DFC algorithms. For both cases, the rotor is rotating at 50 mechanical RPM. In Figure 4.7 the electrical angular position estimation using the Kalman Filter and the IVD-DFC is shown and compared to the real position. The simulation is performed considering a sinusoidal external load torque and the RLS algorithm for the online parameter estimation.

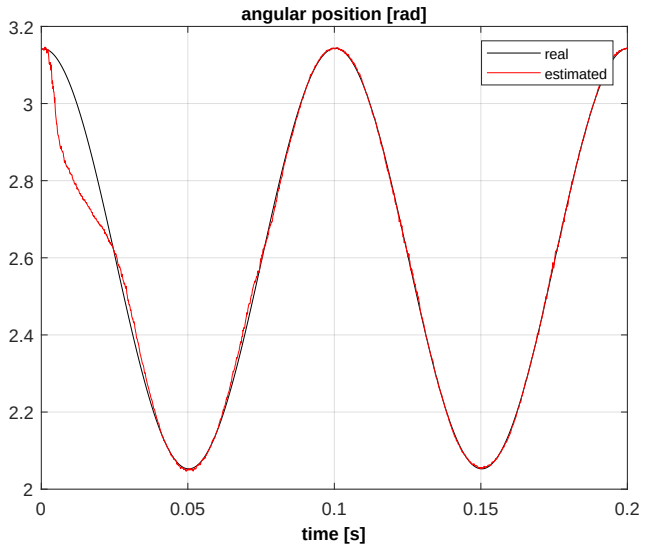

Figure 4.7: Simulation showing the estimated position using the linear Kalman filter and the IVD-DFC/RLS combination.

4.3 Conclusions

A Kalman filter has been applied to the machine equations in order to improve the sensorless estimation process based on the DFC technique. It has been shown that the external load torque applied at the motor shaft can be estimated by increasing the order of the system. Thus, more information about the motor variables is obtained that can be used for control and monitoring purposes. The tuning of the covariance matrices $\mathbf{R}_k$ and $\mathbf{Q}_k$ affects the performance of the filter as depicted in Figure 4.1 through simulation results. The $\mathbf{Q}_k$ must be tuned accordingly to the accuracy of the mathematical model, whereas the value of $\mathbf{R}_k$ must be chosen taking into account the amplitude of the fourth harmonic b as described in equation (4.31). A higher value of b means higher values in the matrix $\mathbf{R}_k$ and this reduces the performance of the observation. Thus, the IVD algorithm can be applied to the position estimation process in order to reduce the effect of the fourth harmonic. Eventually, an RLS type observer has been combined with the Kalman-DFC estimation system to allow the online estimation of the parameter b necessary for the correct functioning of the IVD algorithm. The performance of this innovative observation cluster has been shown through mathematical analysis and simulations, see Figure 4.5 and 4.6 for the estimation of the parameter b and Figure 4.7 for the estimation of the angular position.

5 Experimental Results

Two PMSMs with different specifications have been tested in order to provide experimental results for the verification of the theoretical concepts presented within the previous chapters. The results are divided into four thematic areas that cover the main issues regarding the sensorless control and observation of PMSMs. Firstly, the extracted positions derived from the standard DFC and the IVD-DFC techniques are compared in order to verify the estimation improvement presented in Chapter 3. Secondly, both techniques are coupled to the Kalman filter algorithm and the observation results for the speed and position are compared considering also the EKF technique as possible alternative to the IVD-DFC algorithm. Then, the online estimation of the DFC technique parameters a and b is implemented as presented in Chapter 4, the results are compared for different settings of the estimation algorithm and for different motor conditions. Eventually, the estimated external load torque signals, obtained using both sensorless techniques, are compared considering different settings of the Kalman filter.

5.1 First application: Low-power custom PMSM

For the first experimental set-up, a low-power custom PMSM is considered. The main motor specifications are shown in Table 5.1. Besides the PMSM, the testbench is provided with a servomotor for the application of load torques and for the external drive of the machine, a torque sensor for the measurement of the external load torque applied at the motor shaft and a Baumer GBA2H encoder with 18-bit resolution for the angular position measurement. Every piece is connected to the same shaft as shown in Figure 5.1.

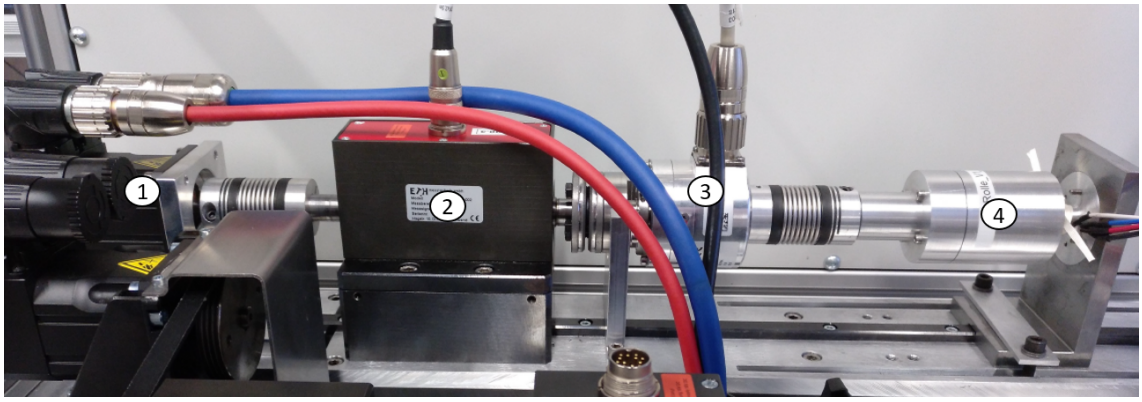

Figure 5.1: The testbench is composed of: the servomotor for the generation of the external load torque (1); the torque sensor (2) and the encoder (3); the PMSM (4).

Parameter	Value
Phase Resistance	2.2 Ω
L_d inductance	394 µH
L_q inductance	475 µH
Back-EMF constant	118.6 mVs
Number of pole pairs	8
Nominal voltage	24 V

Table 5.1: Custom PMSM parameter list

The electronics used for the implementation of the DFC technique as well as the control and the observation algorithms for the PMSM is shown in Figure 5.2. The board features a 32-bit microcontroller, a three-phase inverter bridge, a dedicated electronic for the star-point measurement and a USB communication interface.

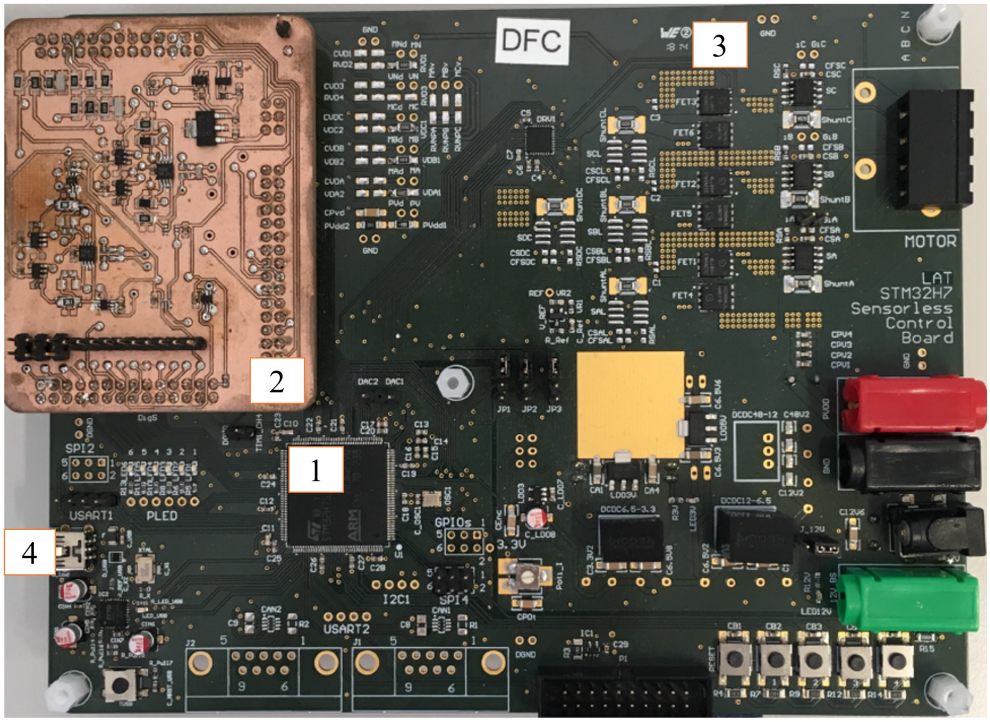

Figure 5.2: The electronic-board used for the tests is provided with a STM-32 microcontroller (1), a board expansion where the DFC electronic is located (2), the power electronic for the supply of the PMSM (3) and a USB connection for the extraction of the data (4).

The performed tests comprehend the current control of the machine under stress conditions and the speed control with external load torque applied.

5.1.1 Driving and control of the machine using standard DFC and IVD-DFC

As shown in Figure 3.1, the DFC signals can be represented into a two axis plane with Γ_α along the $x-$axis and Γ_β along the $y-$axis. In Figure 5.3, the measured DFC signals from the machine are plotted when the motor speed is controlled at 500 mechanical RPM and they are compared to the signals obtained from the IVD-DFC algorithm using one iteration (blue line) and two iterations (red line). The result is shown for multiple electrical rotations of the rotor and the DFC signals are normalized through the parameter a. We suppose that the misalignment of the multiple rotations is due to the not ideal magnetic characteristic of the motor. The reference circle in black represents the ideal signal without anisotropy, hence, the more the signals are close to the reference the more the anisotropy harmonic is reduced. The elimination of the anisotropy effect using one iteration is noticeable and an increment of the iterations does not further improve the performance. Hence, a single iteration is enough for the IVD-DFC in order to eliminate almost completely the anisotropy harmonic.

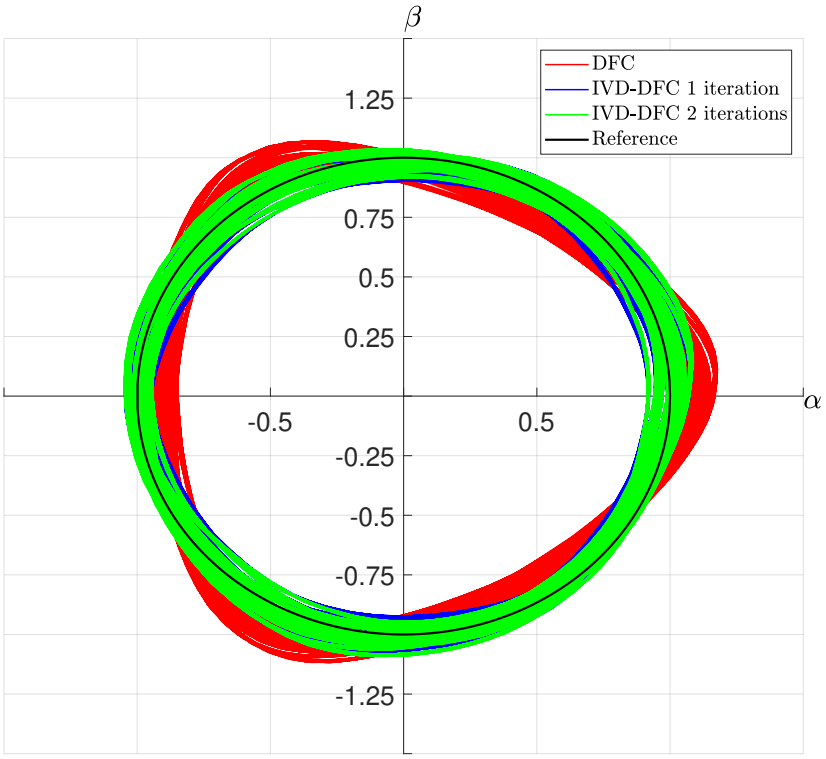

Figure 5.3: $\alpha - \beta$ representation of the normalized DFC and IVD-DFC signals. The black circle represents the ideal behavior of the signals, that is, without any multiple harmonics. The signals are referred to a mechanical rotor angular speed of 500 RPM and are sampled at 5 KHz.

An additional proof of the anisotropy harmonic reduction can be given by means of an FFT analysis of the DFC and IVD-DFC signals. In Figure 5.4, the FFT amplitude response calculated for both DFC signals and IVD-DFC signals with one iteration is presented. As

shown, two amplitude peaks are prevalent among the whole frequency spectrum. They represent respectively the first and the second saliency harmonics. The peak of the second harmonic is reduced using the IVD-DFC about more than 80% of the original value. The FFT shows small amplitude harmonics before the first peaks.

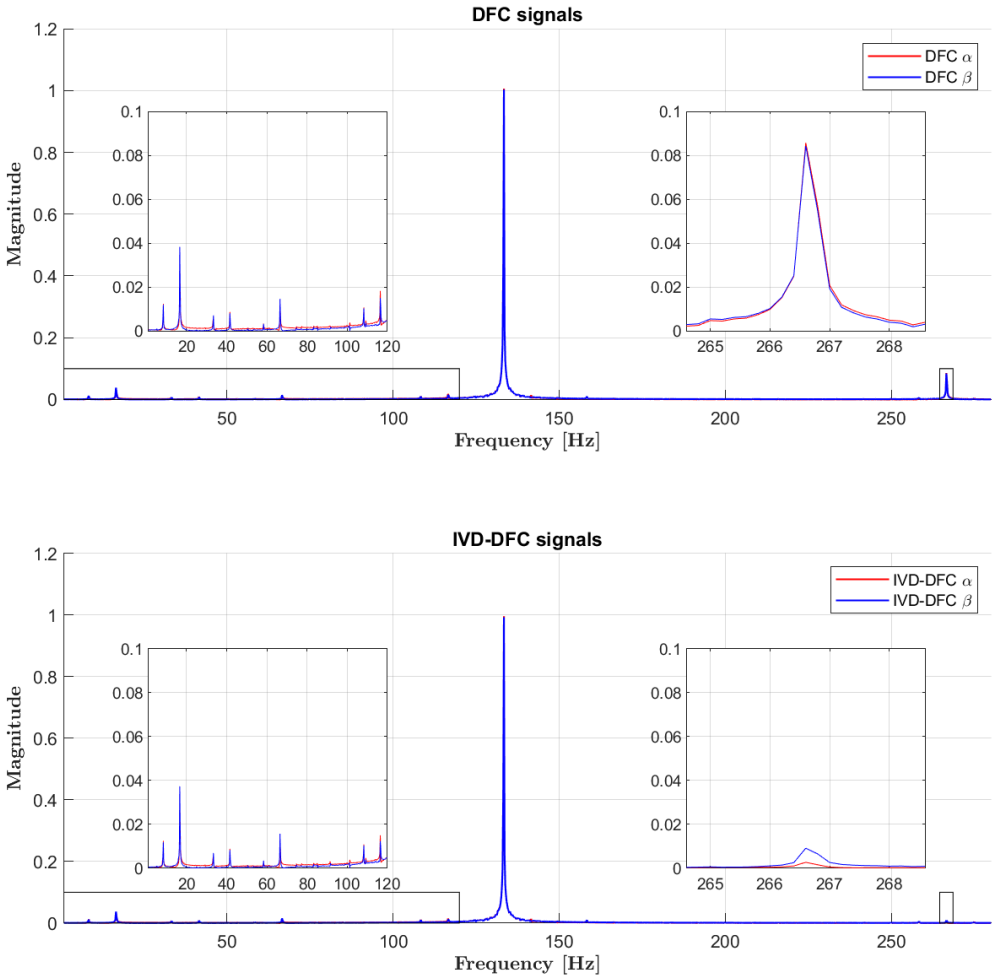

Figure 5.4: Frequency amplitude response comparison between DFC and IVD-DFC signals using one iteration.

The previous results have been obtained without considering the possible phase shift effect over the DFC signals. In order to appreciate this effect, the PMSM has been driven externally by the servomotor at constant speed (300 mechanical RPM) and the PMSM current along the q-axis is controlled using increasing current reference starting from 0 to 1.5 Ampere. As shown in Figure 5.5, the mean value module of the error between the encoder and the DFC position increases accordingly to the current. Then, the relation between the phase shift variables φ_a, φ_b and the current has been fitted offline using the MATLAB Identification Toolbox and the Full IVD-DFC algorithm has been performed. The reduction of phase shifts and harmonics over the position estimation is clearly depicted in Figure 5.5.

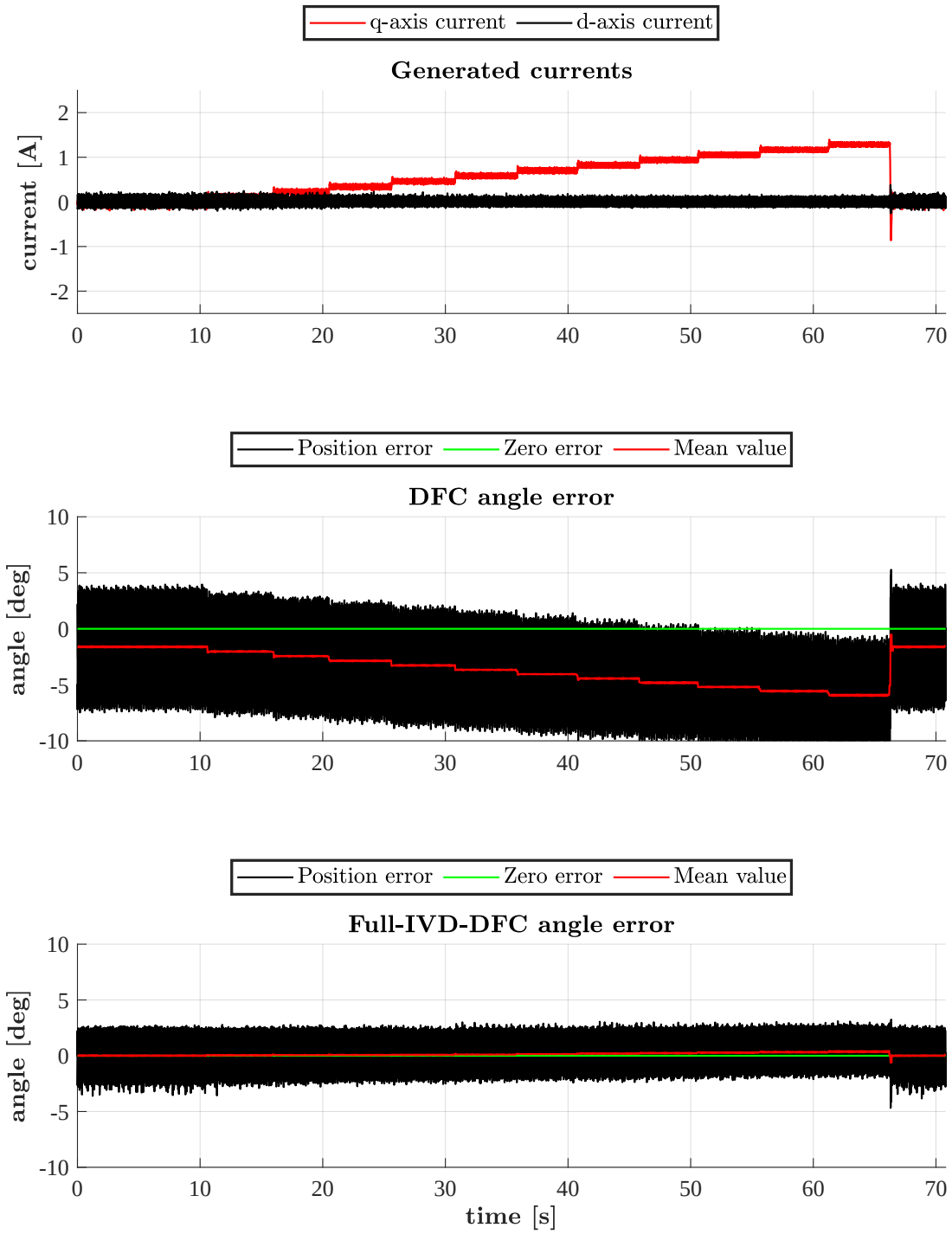

Figure 5.5: Current steps with increasing amplitude are generated on the q-axis of the motor when the external servo-motor drives the PMSM at 300 RPM. The angle error of the DFC algorithm is compared with the IVD-DFC one.

5.1.2 Kalman Filter for the speed and position

The position extracted by means of the standard DFC and IVD-DFC techniques are filtered using a Kalman filter in order to reduce its deterioration due to noise acting on the DFC signals. Reminding equation (4.29), we expect a better observation performance for the IVD-DFC considering the same value of covariance value R_k for both techniques. That has been experimentally proven by means of Kalman filter speed estimation comparison when the motor is controlled at different speeds. Additionally to the Kalman filter, the estimation results obtained by the EKF are presented as possible alternative to the IVD-DFC technique. The estimation results are shown in Figure 5.6, with a speed reference of 100 RPM, and in Figure 5.7 for 500 RPM. According to the matrix tuning argumentations provided within the previous chapter, the covariance matrix $\mathbf{Q}_k$ is defined as:

$$\mathbf{Q}_k = \begin{bmatrix} 1 & 0 & 0 \\ 0 & 0 & 0 \\ 0 & 0 & 10^{-6} \end{bmatrix}. \tag{5.1}$$

The drive and control of the machine is performed using respectively the estimated quantities of each experiment. Thus, for the DFC speed estimation experiment the DFC position is used for the FOC and the DFC estimated speed is filtered using a low-pass filter and fed to the speed control algorithm. The IVD-DFC and EKF experiments are performed using, respectively, the observed speed and position of the Kalman filter for FOC and speed control. As depicted in Figure 5.6, the Kalman filter is not able, given the values of $\mathbf{Q}_k$ and R_k, to reject the anisotropy component of the DFC measurements. This issue could be overcome using a greater value of R_k but, as shown in Figure 5.8, the presence of uncertainties on the mathematical model at low speed cancels the expected improvement. Differently, for high-speed operation an increased value of R_k seems to be a good choice (see Figure 5.9) since the anisotropy component is almost completely filtered. However, a greater value of R_k causes the estimation to be less responsive and, consequently, the speed control should be tuned to a lower bandwidth. However, if we consider the results obtained by the IVD-DFC and the EKF, we can observe a clear improvement of the estimated signals.

			Enc.	DFC	DFC + KF	IVD	IVD + KF	EKF
Speed	R_k	m/sD						
100 RPM	σ_v	m	$6.5e^{-3}$	$5.5e^{-3}$	$-1.32e^{-2}$	$1.02e^{-2}$	$1.69e^{-2}$	$-2.71e^{-2}$
		sD	4.89	24.46	29.54	8.35	10.14	7.1877
	$5{\cdot}\sigma_v$	m			$-2.53e^{-2}$		$-2.91e^{-2}$	$-5.16e^{-2}$
		sD			32.01		13.91	8.33
500 RPM	σ_v	m	$4.3e^{-4}$	$-1.32e^{-2}$	$-8.94e^{-4}$	$-0.48e^{-2}$	$0.23e^{-2}$	-1.81
		sD	7.1	102.11	31.45	35.39	16.25	29.05
	$5{\cdot}\sigma_v$	m			$4.06e{-}4$		$2.9e^{-3}$	-1.26
		sD			19.66		12.9	22.4

Table 5.2: Mean (m) and standard deviation (sD) values of the speed estimation error evaluated for different speed references and R_k values.

Table 5.2 summarizes the performance of every technique by means of standard deviation

and mean values of the error between the reference speed and estimated speed obtained using all the techniques calculated at operating speed.

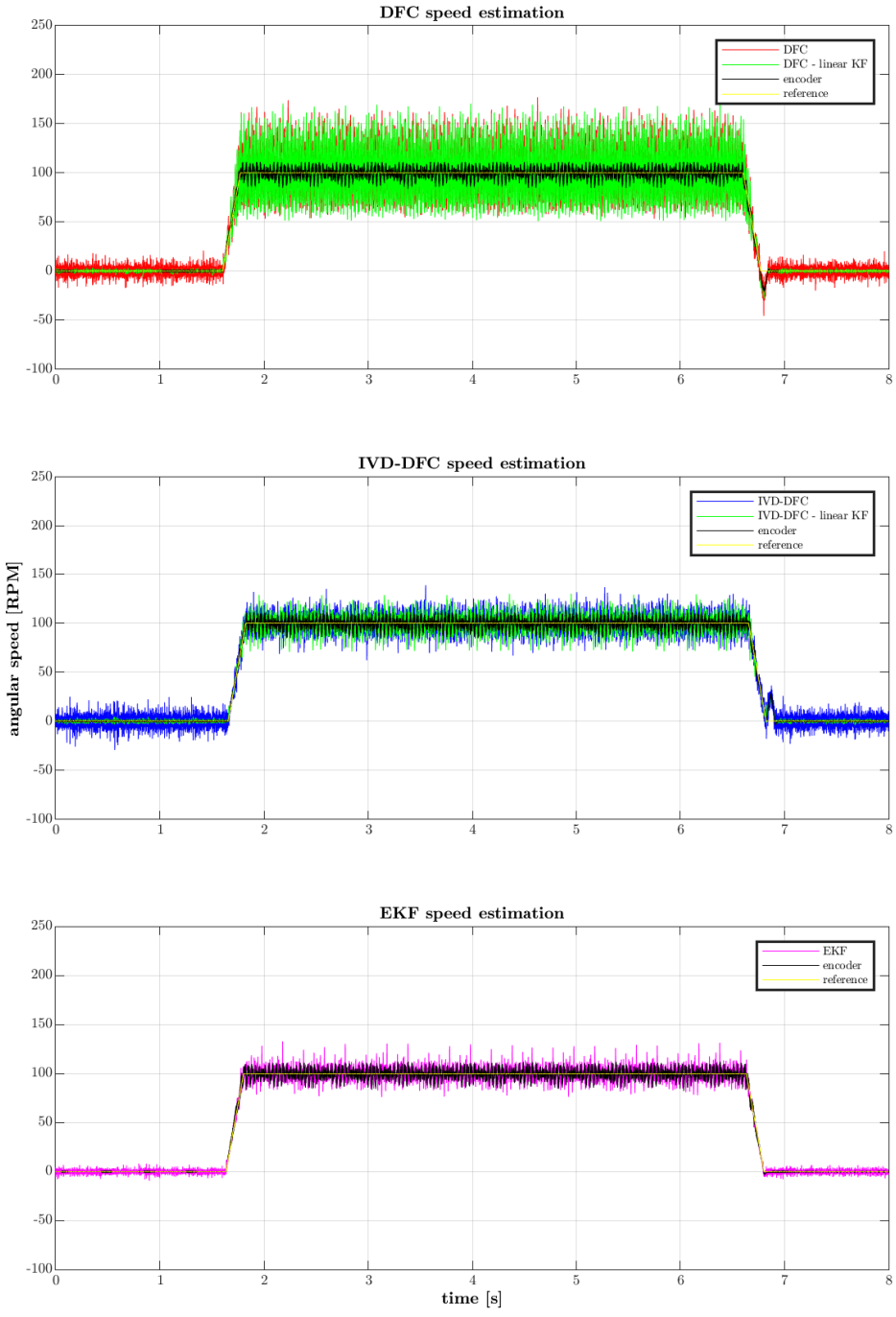

Figure 5.6: Speed estimation comparison for different techniques. The motor is controlled at 100 RPM

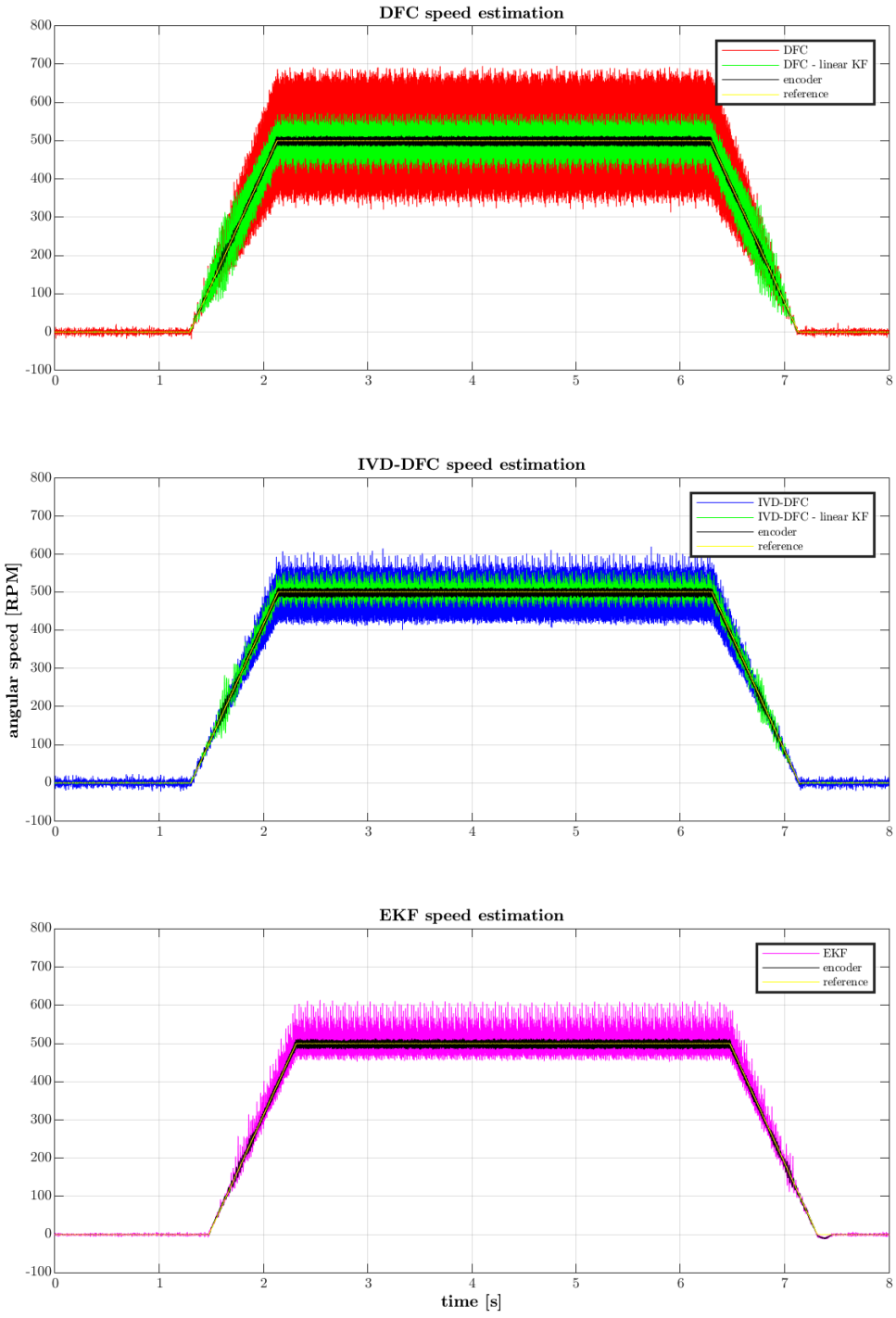

Figure 5.7: Speed estimation comparison for different techniques. The motor is controlled at 500 RPM

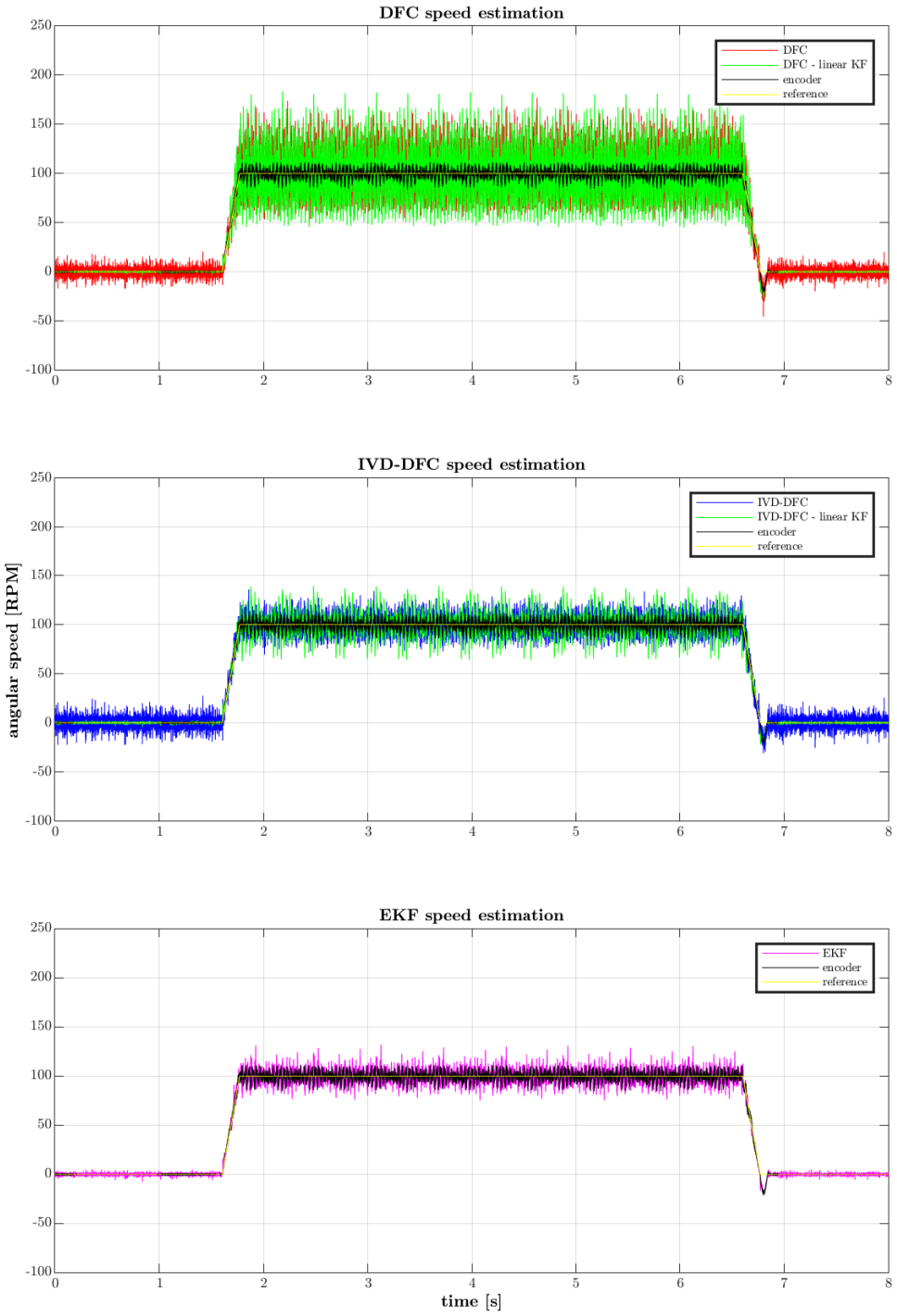

Figure 5.8: Speed estimation comparison for different techniques. The motor is controlled at 100 RPM. The value of R_k is $5 \cdot \sigma_v^2$.

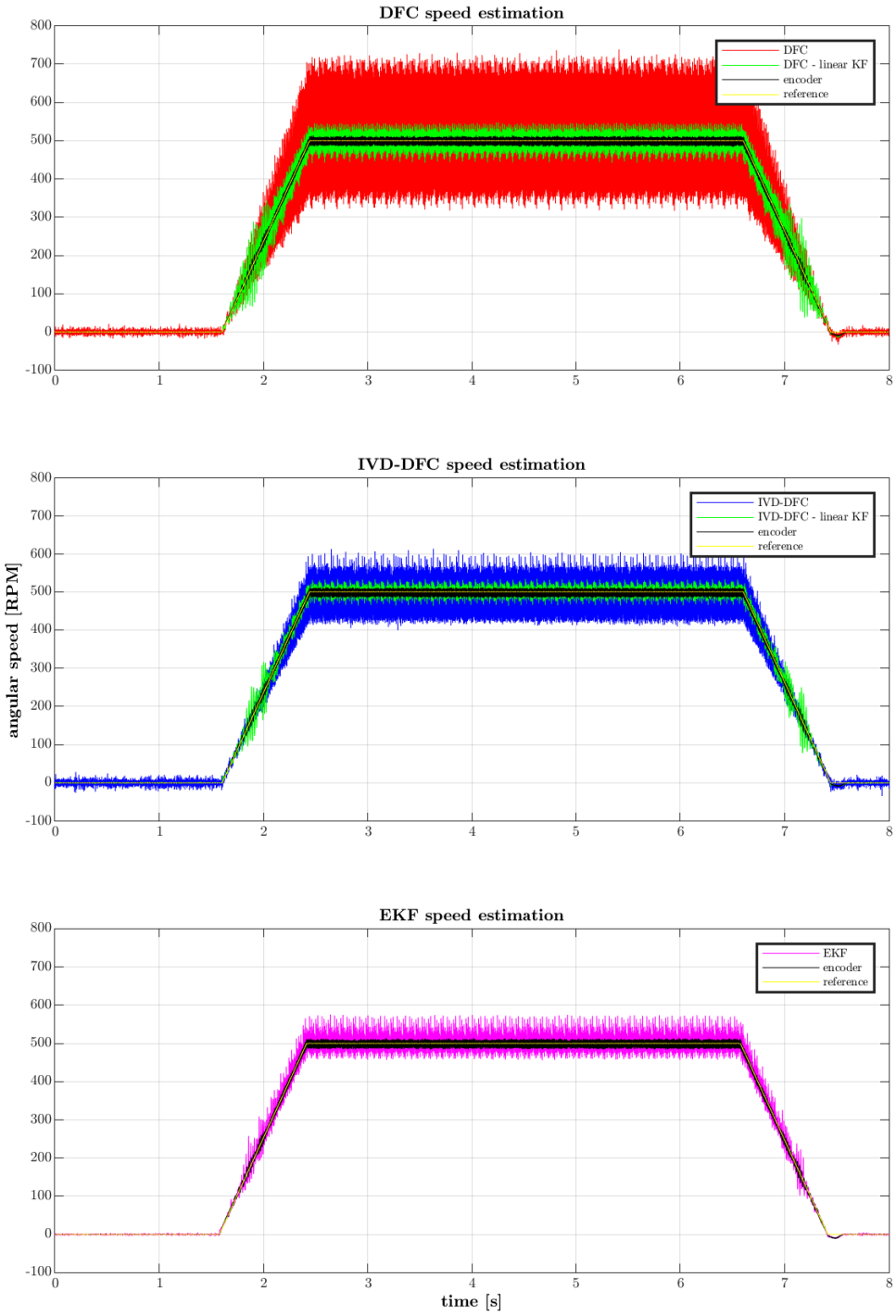

Figure 5.9: Speed estimation comparison for different techniques. The motor is controlled at 500 RPM. The value of R_k is $5 \cdot \sigma_v^2$.

According to the values listed in Table 5.2, the IVD-DFC technique combined to the Kalman filter and the EKF are offering a better estimation in terms of the error standard deviation as compared to the standard DFC technique. In some cases, the IVD-DFC alone could achieve slightly better results compared to the standard DFC combined with the Kalman filter. In Figure 5.10, the estimated position and the position estimation error are compared considering the standard DFC, the IVD-DFC and the EKF methods. Although the mean value of the EKF estimation error converges to zero, the IVD-DFC algorithm provides the position estimation with the smallest standard deviation of the error. Moreover, the use of the EKF is not recommended since an offline estimation of the parameter a and b is required and also because the results are not always better than the IVD-DFC technique. On the contrary, the IVD-DFC shows in some cases improvement on the estimation results. Moreover, the IVD-DFC can be coupled to an online estimation technique for the determination of the parameter b. The results obtained through this method will be presented within the next subsection.

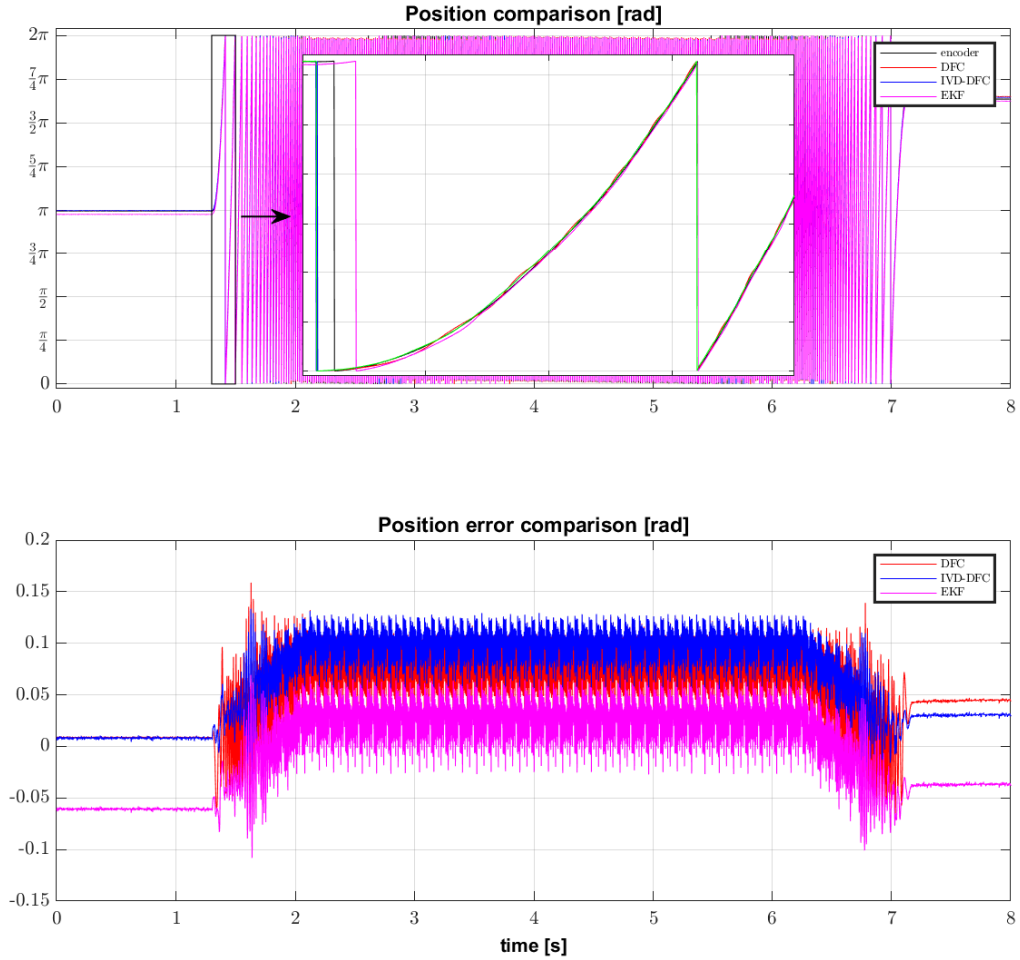

Figure 5.10: Speed estimation comparison for different values of the covariance R_k. The speed control of the motor is performed using the encoder speed.

5.1.3 IVD-DFC with online estimation of the parameter b

The implementation of the IVD-DFC or the EKF methods requires the knowledge of the parameter b or both a and b respectively, the results shown in the previous section have been obtained by means of an offline estimation using the encoder as position measurement. Since it is not possible to extract the position information using the EKF and simultaneously using that for the estimation of the parameter because the system results to be not observable, it is instead possible to use the position extracted using the IVD-DFC algorithm for that purpose. In Figure 5.11 and 5.12, the results obtained using the combination of IVD-DFC and a RLS estimation algorithm as proposed in Chapter 4 are shown. It has to be remarked that the performance of the RLS algorithm is dependent on the angular speed of the machine. For higher speed values the convergence of the parameter estimation is more rapid than for the case of lower speed. The RLS method has been tuned in order to operate satisfactorily for every speed value. From Figure 5.11, it can be noticed that the tracking of the parameter a and b is achieved as the motor speed reaches the reference value. Figure 5.12 presents the same type of experiment but with an increased bandwidth for the RLS algorithm. Thus, the parameters reach their values more rapidly but the estimation is affected by more noise. For both cases the IVD-DFC is able to reduce the effect of the fourth anisotropy harmonic, the standard deviation of the speed with respect to the reference and the standard deviation of the position error are halved compared to the values obtained using the DFC techniques. It is interesting now to present the statistic about the mean value of the computational time for every algorithm used for the experiments. That information will provide an idea of the microcontroller effort in order to perform the algorithms. The values are listed in Table 5.3.

Algorithm	**Time** $[\mu s]$
IVD-DFC with standard C library $\arctan$ function (one iteration)	1.8
IVD-DFC with CORDIC $\arctan$ function (one iteration)	0.55
Kalman Filter	2.15
Extended Kalman Filter	4.65
RLS Parameter Identification	1.3

Table 5.3: Mean values of the computational time taken by each algorithm.

Surely, the major drawback of the IVD algorithm is the iterative execution of the $\arctan$ function. The implementation of this function using the C standard libraries algorithm is usually cumbersome as shown in the previous table. Nevertheless, some microcotroller MCUs provides a CORDIC (COordinate Rotation DIgital Computer) module to accelerate computations. The CORDIC is a simple and efficient algorithm used for the calculation of trigonometric functions, hyperbolic functions, square roots, multiplications, divisions, and exponentials and logarithms. In fact, the only operations it requires are additions, subtractions, bitshift and look-up table. Thanks to its implementation, the time required for the calculation of a single IVD iteration using the CORDIC module is four times smaller than the same operation implemented with the standard C library. The computational time taken by the combination of IVD-DFC (with CORDIC disabled or at the most two iteration with CORDIC), Kalman filter and RLS exceeds the time taken by the EKF. However, no online parameter estimation is possible with the EKF.

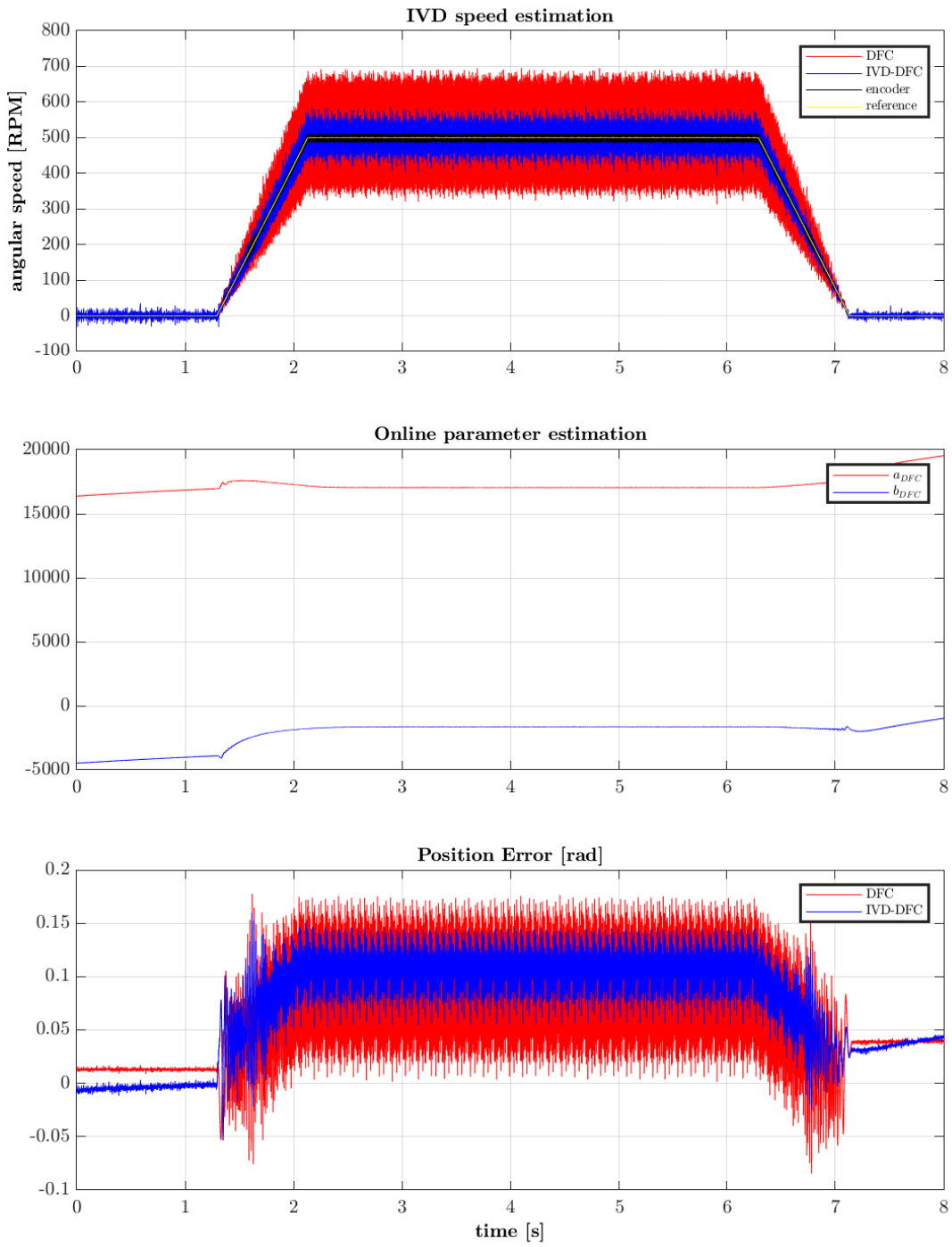

Figure 5.11: This figure presents the speed and position estimation performance of the combined IVD-DFC and RLS algorithms. The estimation is compared to the online parameter identification of a and b.

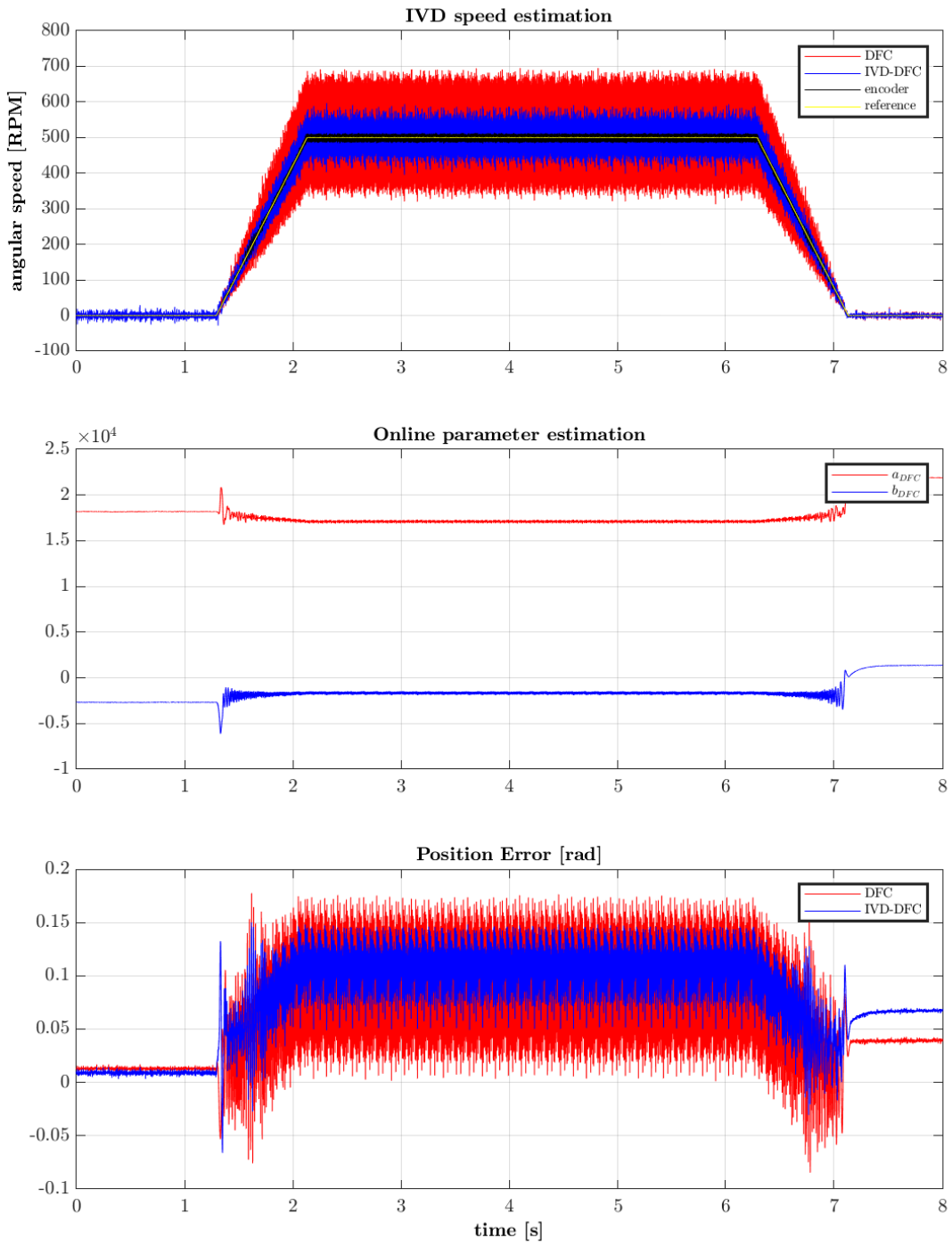

Figure 5.12: This figure presents the speed and position estimation performance of the combined IVD-DFC and RLS algorithms. The estimation is compared to the online parameter identification of a and b. A greater value for the matrix $\mathbf{P}$ is considered.

5.1.4 Estimation of the external load torque

As additional information, the external load torque can be estimated using Kalman filtering. Since the EKF is not considered a practical choice for the sensorless control of the machine, because it needs a previous identification of the parameter and it requires a great computational effort, its results are not considered in this subsection. Figure 5.13 shows the external load torque estimated using respectively the Klaman filter with the DFC and IVD-DFC techniques when an external torque of about 0.1 Nm is applied at the motor shaft using the external servo-motor as brake. The external torque is applied for every time instant whereas the motor speed is controlled at 500 RPM (similar to the previous subsection experiments). During the first and final phase of the control, in conjunction to the speed reference ramps, the estimation is not so accurate as in the central part. This is due to the inaccuracy of the speed model for low speed values. Nevertheless, the IVD-DFC allows to obtain a better estimation results than the DFC in terms of signal smoothness.

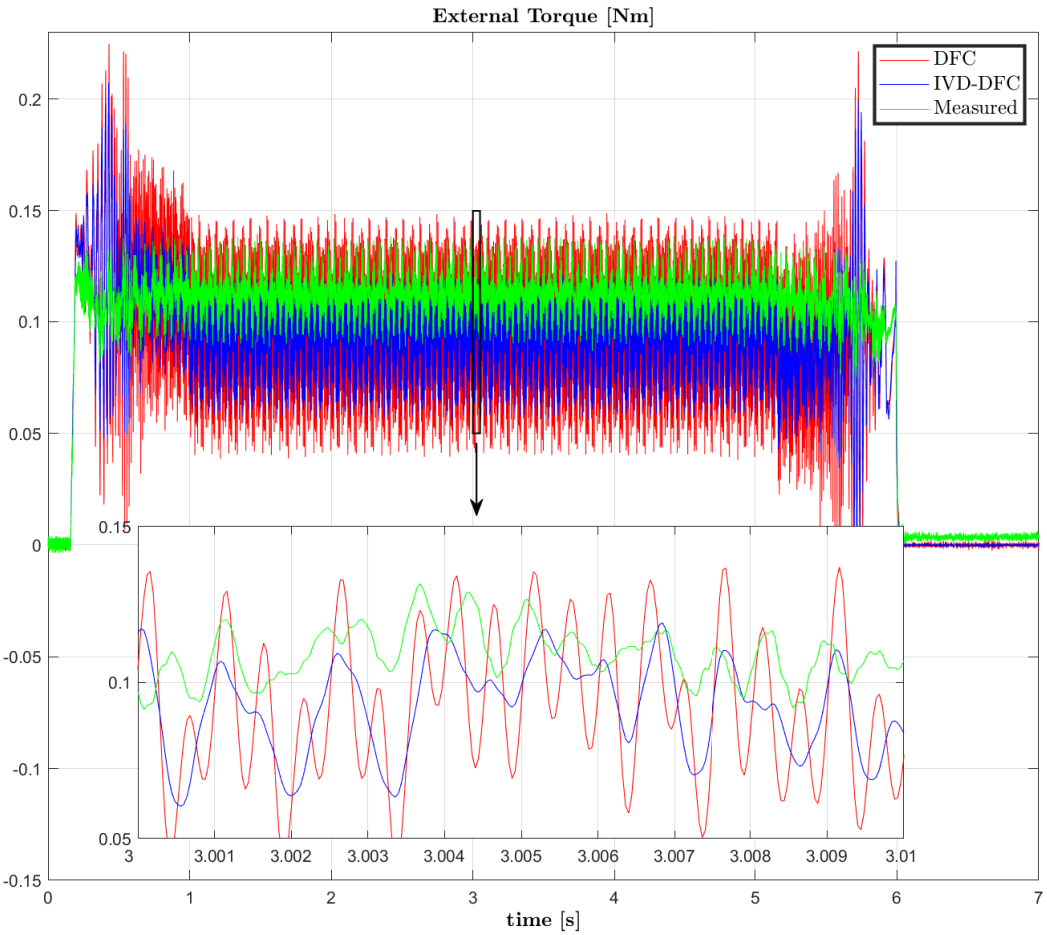

Figure 5.13: External load torque estimation comparison between DFC and IVD-DFC techniques. An external torque of 0.1 Nm is applied at the motor shaft by means of the servo-motor. The signals are compared to the measured torque.

It has to be remarked that the estimated variable Ξ_l contains information about the external load torque as well as the possible uncertainties on the mechanical model of the machine. Thus, theoretically, the two contributions should be divided. Since no valid strategy exists in order to separate them, the mathematical model of the mechanical part of the machine should be well known. In Figure 5.14 the speed convergences of the estimation to the reference value are compared for different $\sigma^2_{w_{\Xi_l}}$. The reduction of its value, as plotted on the right side of the figure, causes the estimation to provide smoother results. However, the estimation speed convergence is also reduced introducing a greater delay and that could possibly affect negatively the estimation of the other variables (speed and position).

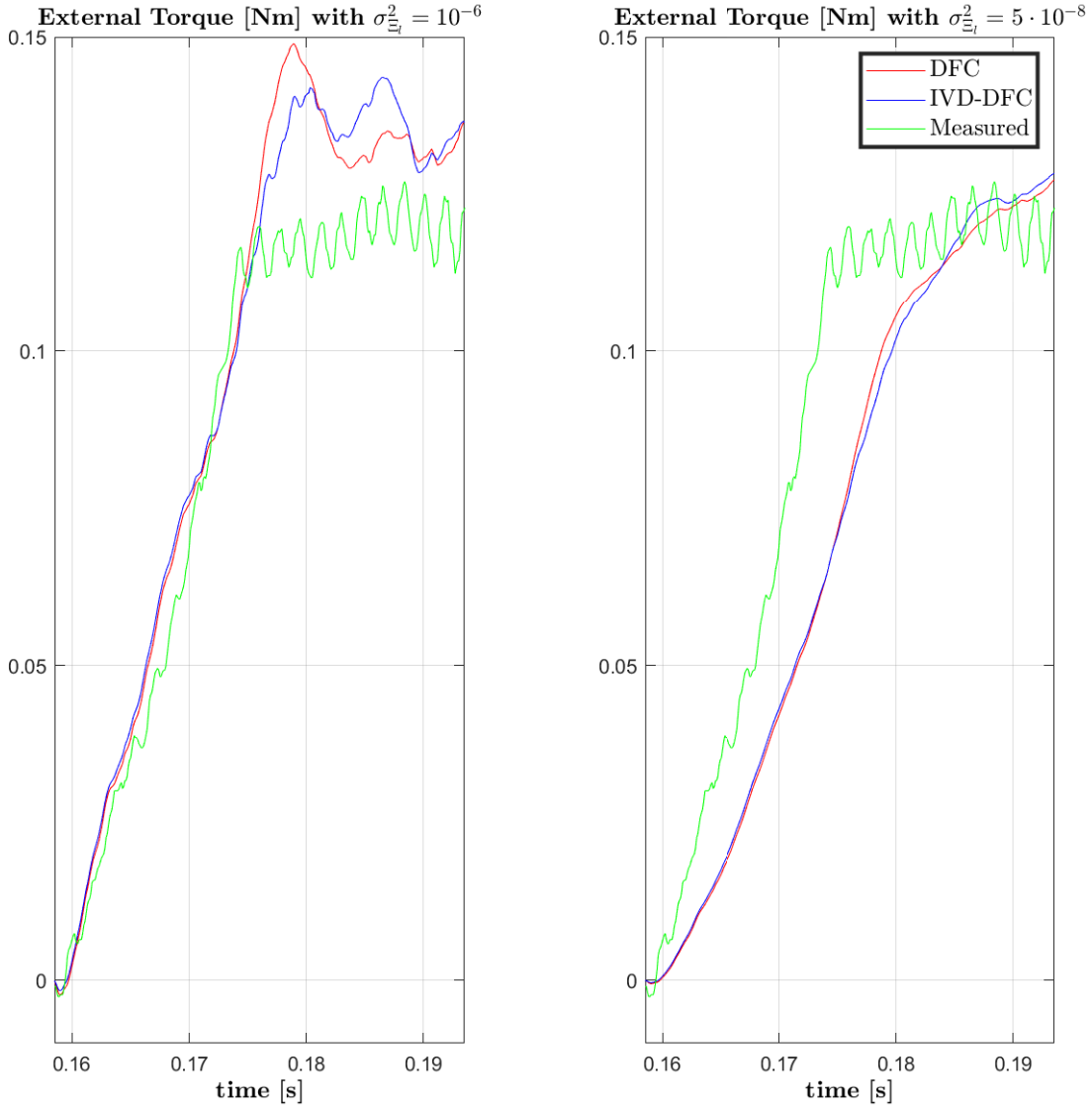

Figure 5.14: Comparison of load torque estimation convergence speed using two different value of $\sigma^2_{w_{\Xi_l}}$. The plot on the right side is obtained using a value of $\sigma^2_{w_{\Xi_l}}$ twenty times smaller than that one used for the plot on the left side.

The statement made previously about the speed convergence of the estimation is confirmed by the experiment shown in Figure 5.15. This time, a sinusoidal current is given as current reference for the motor control. The frequency of the current is chosen high enough in order to maintain the rotor position constant (in this case 4 Hz). Hence, the PMSM is now used as external torque generator. A greater value of σ_{w_Ξ} corresponds to a greater bandwidth of the estimation process. Thus, the observer is able to estimate correctly a wider range of load torque harmonics compared to an observer with lower σ_{w_Ξ}. On the counter part, the estimated signal is more noisy. Nevertheless the Kalman filter combined with the IVD-DFC technique presents better results than the combination with the DFC in terms of noise rejection.

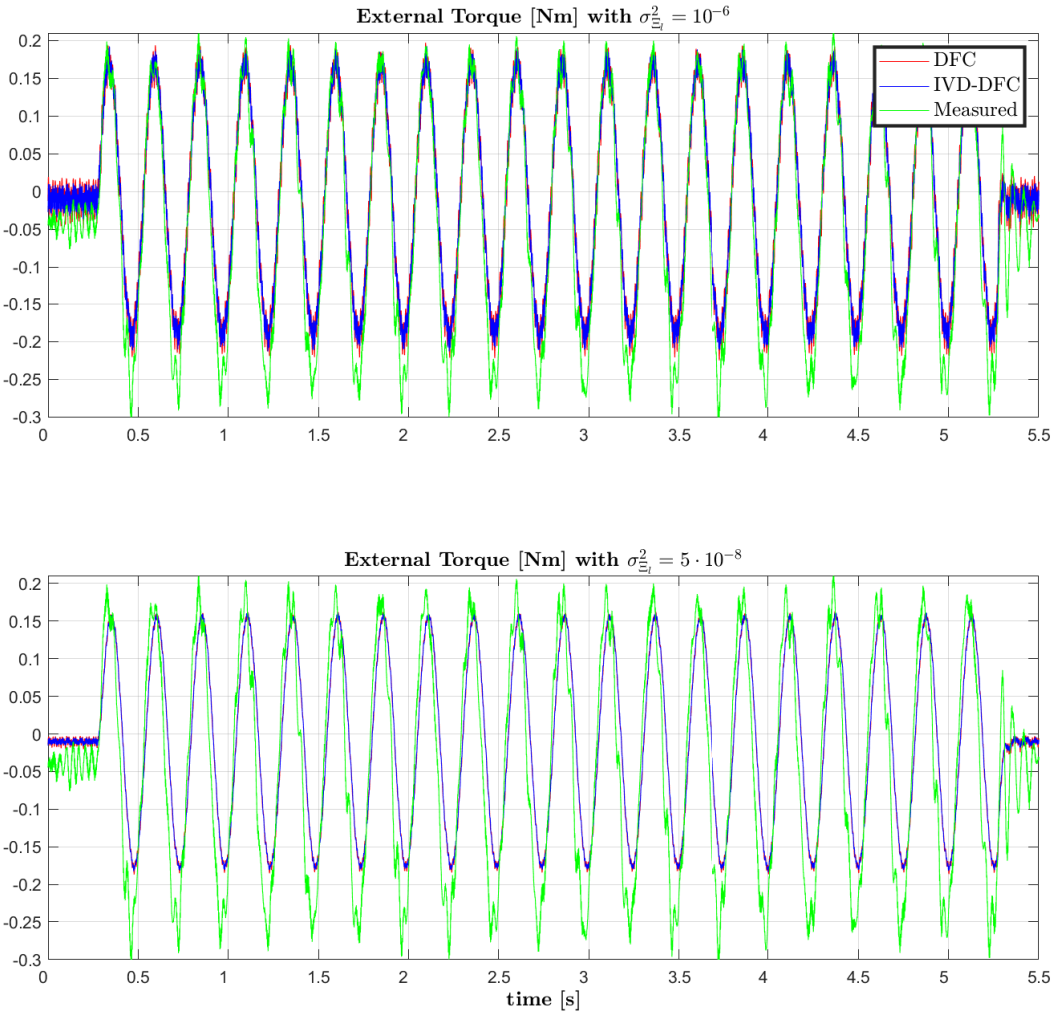

Figure 5.15: Comparison of load torque estimation convergence speed using two different value of $\sigma^2_{w_{\Xi_l}}$ as a sinusoidal load torque is applied. The plot below is obtained using a value of $\sigma^2_{w_{\Xi_l}}$ twenty times smaller than that one used for the plot above.

5.2 Second application: e-bike

As additional application of sensorless control for PMSMs, the results obtained using a PMSM for e-bike are presented. Differently from the previous case, no measurement for the position and external load-torque is available for a comparison. Thus, a thoroughly performance report of the technique is not possible to be provided. Nevertheless, the e-bike motor presents a clearly greater fourth harmonic effect on the DFC signals, as shown in Figure 5.17. Hence, in this section we will focus more on the IVD-DFC technique ability of rejecting the fourth harmonic effect on the position extraction than on the speed and torque estimation through the Kalman filter. The motor parameters are listed in Table 5.4.

Figure 5.16: Set-up used for the experiments with the e-bike motor.

Parameter	Value
Phase Resistance	0.069 Ω
L_d inductance	103 µH
L_q inductance	149 µH
Back-EMF constant	23.6 mVs
Number of pole pairs	23
Nominal voltage	24 V

Table 5.4: E-bike PMSM parameter list

5.2.1 Driving and control of the machine using standard DFC and IVD-DFC

As first result, the comparison between the standard DFC signals and the IVD-DFC signals for different number of iterations is shown in Figure 5.17. As for the previous motor, already by the first iteration (blue line) the graph is closer to the reference circle. Differently from the previous case, it is possible to notice a further improvement of the signals by the second iteration (green line). Eventually, a magenta line is added in order to show the IVD-DFC results after ten iterations. The obtained signals by ten iterations match the reference circle almost perfectly. However, it will be shown that four iterations are enough in order to reject almost completely the fourth harmonic.

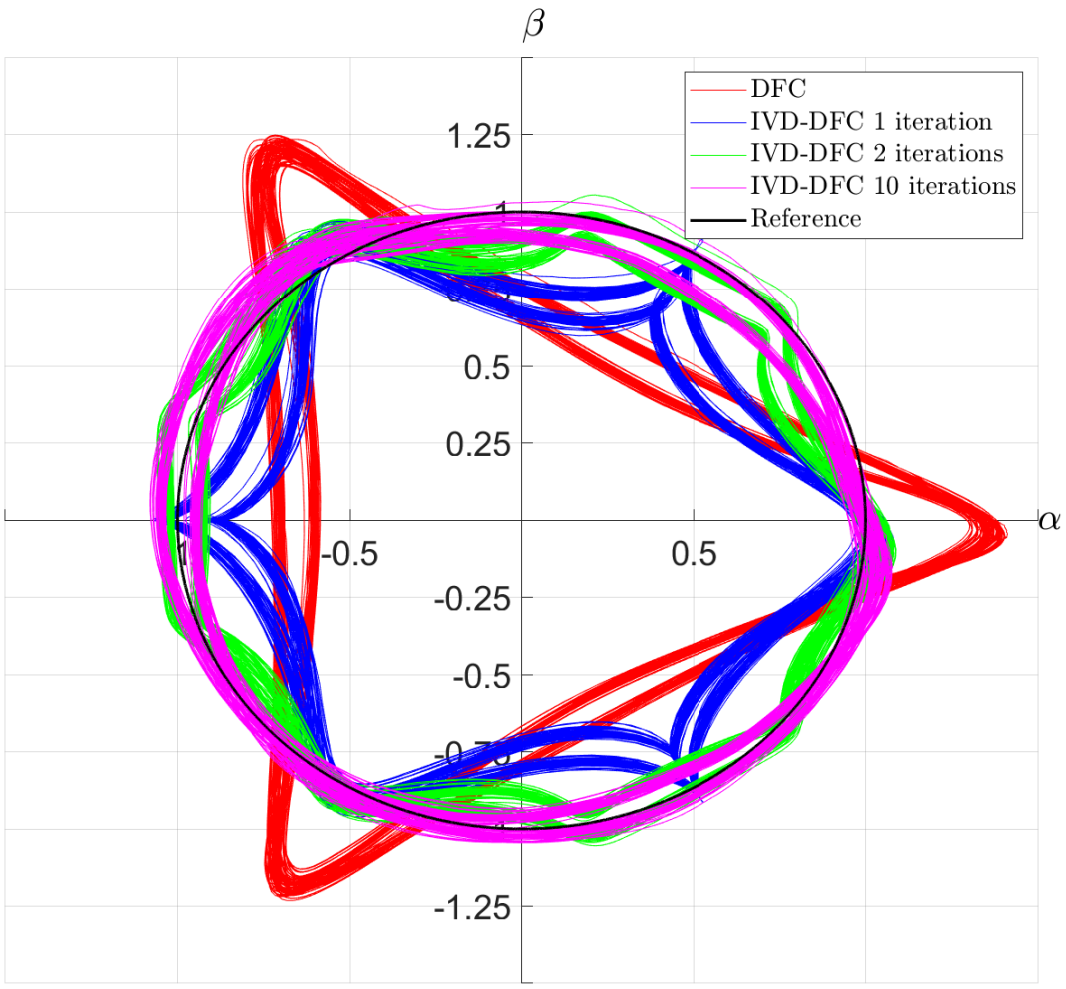

Figure 5.17: $\alpha - \beta$ representation of the normalized DFC and IVD-DFC signals. The black circle represents the ideal behavior of the signals, that is, without any multiple harmonics. The signals are referred to a mechanical rotor angular speed of 50 mechanical RPM and are sampled at 5 KHz.

A FFT analysis of the obtained signals is performed in order to provide an additional proof of the improvement produced by the IVD-DFC algorithm. The FFT results are presented in Figure 5.18. The IVD-DFC signals are referred to a four iteration process. As shown, the peak presents at 76 Hz, namely the fourth harmonic, is reduced using the IVD-DFC by more of the 90 % of the original value.

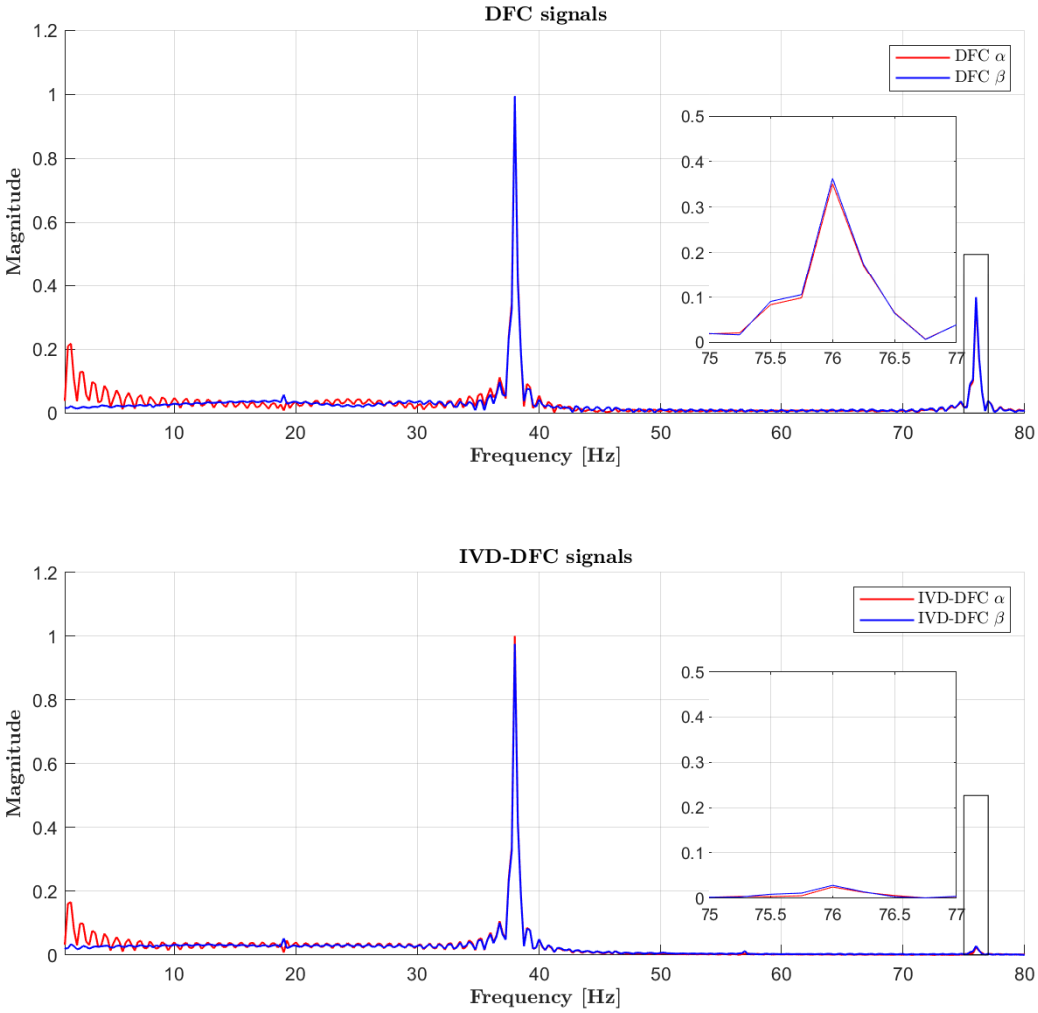

Figure 5.18: Frequency amplitude response comparison between DFC and IVD-DFC signals using four iteration.

5.2.2 Kalman Filter for the speed and position filtering

An interesting result is obtained considering the sensorless speed control of the motor using the DFC and the IVD-DFC technique combined with a Kalman filter. As shown in Figure 5.19, the DFC speed signal is greatly affected by oscillations, clearly larger compared to the previous application. In fact, accordingly to equation (3.73), a greater value of b, and consequently of p, corresponds to a greater error on the speed estimation. That results

also in an error on the mean value of the estimated speed as shown clearly by the IVD-DFC estimation in Figure 5.19. Using the DFC combined with the Kalman filter provides a deteriorated speed estimation whose mean value is 20% lower than the reference speed. Instead, using the IVD-DFC combined with the observer, the speed estimation performance is improved and its mean value is more accurate as depicted in Figure 5.20.

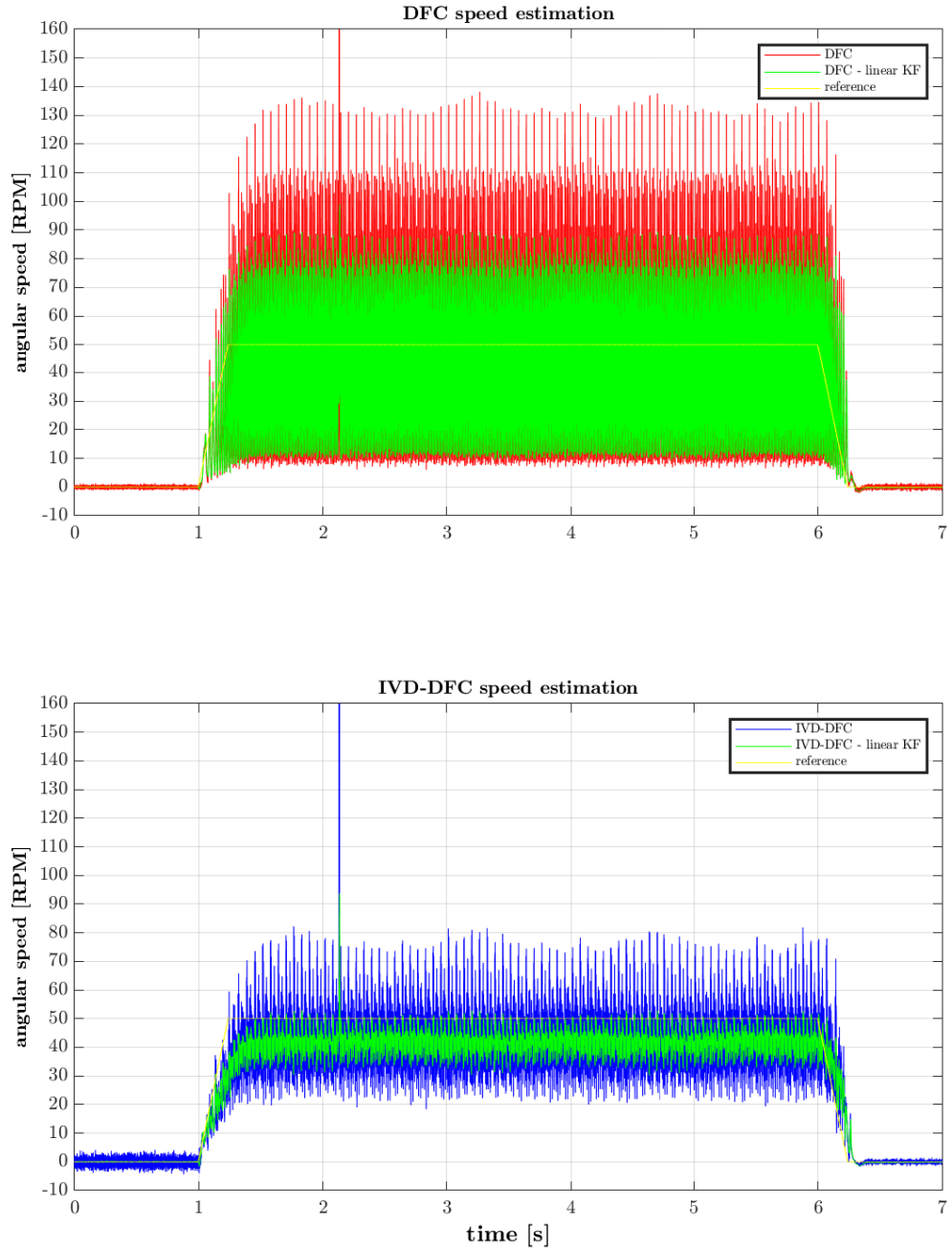

Figure 5.19: Speed estimation comparison using the DFC - Kalman filter estimated position and speed respectively for the FOC speed control of the motor.

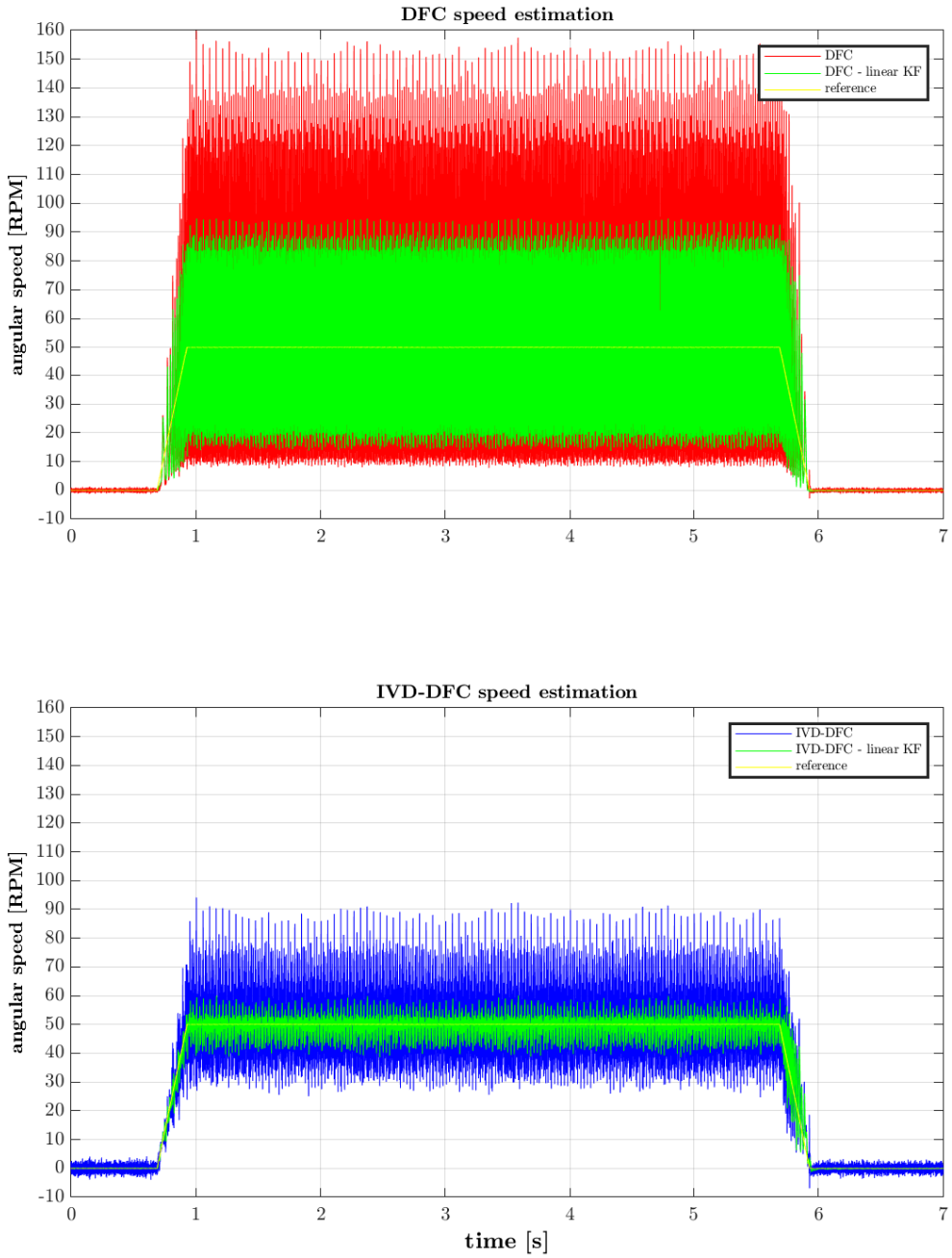

Figure 5.20: Speed estimation comparison using the IVD-DFC - Kalman filter estimated position and speed respectively for the FOC speed control of the motor.

Hence, it is clear from the experiments the importance of the IVD-DFC algorithm in order to obtain generally better results in terms of estimation accuracy and consequently for the machine control.

5.2.3 IVD-DFC with online estimation of the parameter b

As for the previous application, it is interesting to look at the estimation results as the IVD-DFC algorithm is combined with the online estimation of the parameters a and b. In Figure 5.21, the parameter b is estimated performing the IVD-DFC algorithm with one iteration. As for the previous case, the correct estimation of the parameter depends on the angular speed of the rotor. A higher speed corresponds to a more rapid convergence of the estimated variable to the real values. Moreover, the number of iterations plays a role on the performance of the estimation process. It has been proven experimentally that the IVD-DFC with a higher number of iterations needs contemporary a rapid and smooth estimation of b in order to perform properly. In Figure 5.22, the estimation results are shown as four iterations are considered for the IVD-DFC.

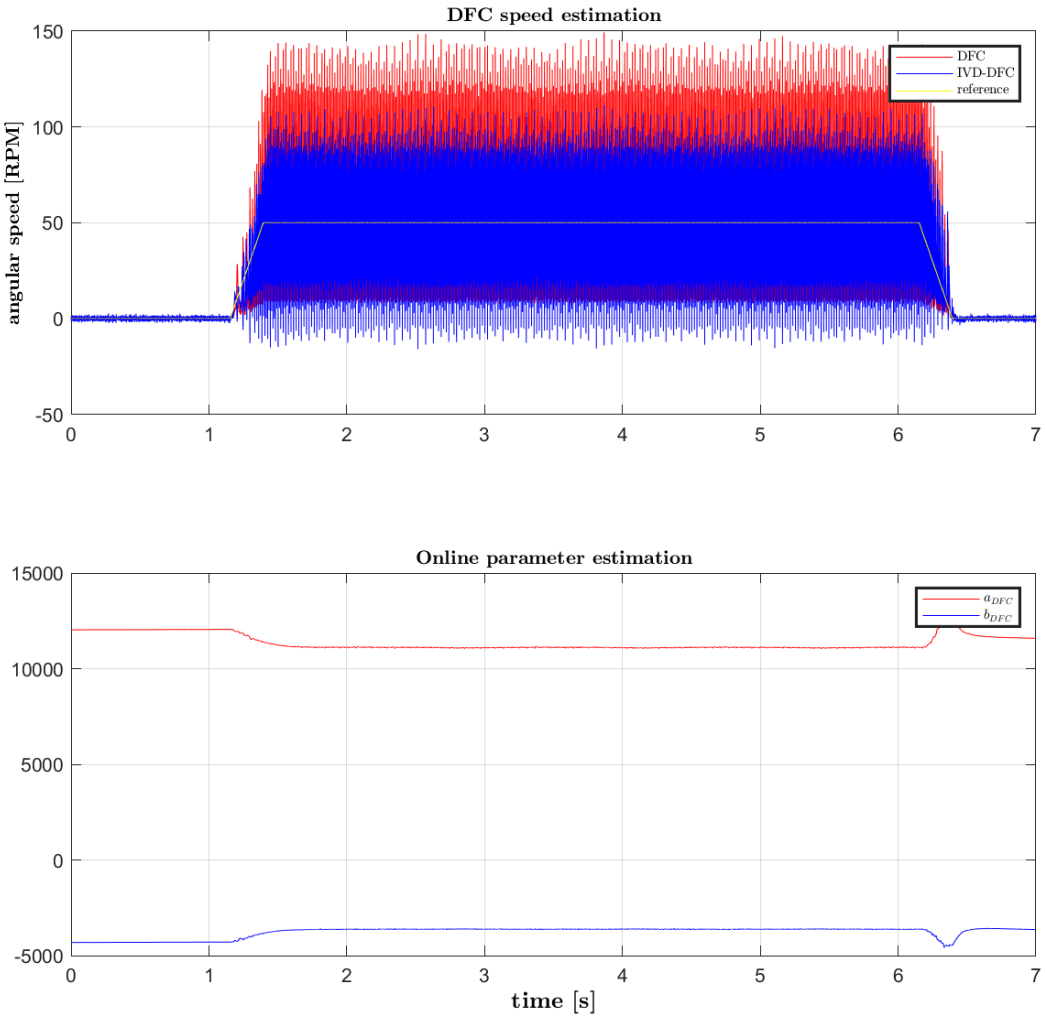

Figure 5.21: This figure presents the speed estimation performance of the combined IVD-DFC and RLS algorithms. The estimation is compared to the online parameter identification of a and b.

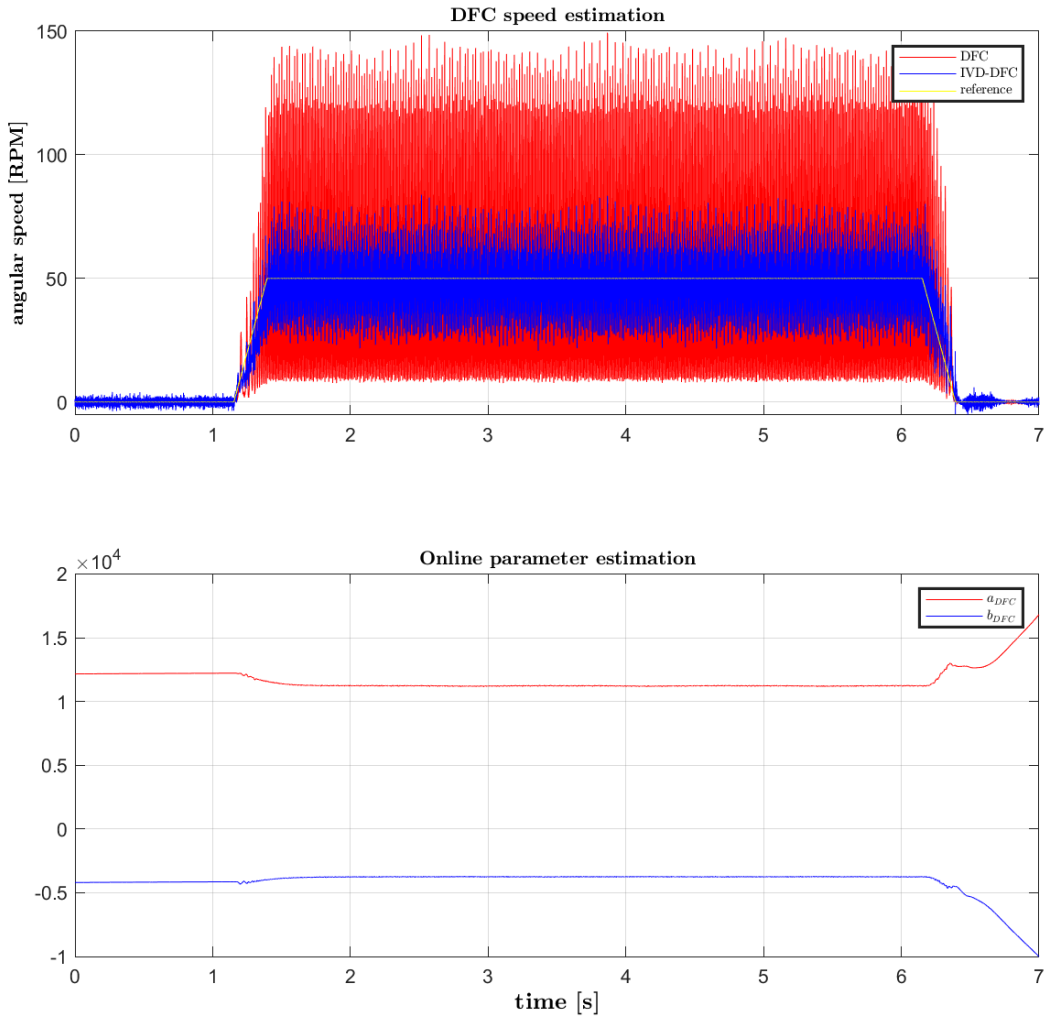

Figure 5.22: This figure presents the speed estimation performance of the combined IVD-DFC and RLS algorithms. The estimation is compared to the online parameter identification of a and b. The value of the matrix $\mathbf{P}$ is increased.

5.2.4 Estimation of the external load torque

Eventually, the result of the external load torque estimation is provided in Figure 5.23 where a constant torque is applied by the bike brake for a short time. Considering the same value for σ_{w_Ξ} for both sensorless technique, the IVD-DFC algorithm is able to filter most of the undesired harmonics. A third estimation is added considering a smaller value of σ_{w_Ξ} for the DFC method (magenta line). The noise of the additional estimation signal is similar to the IVD-DFC one but its response is not rapid as the IVD-DFC method. Hence, in order to decrease the oscillation due to the fourth harmonic anisotropy effect the Kalman filter should be tuned as for the magenta line, but the performance would be low. On the other hand, the use of the IVD algorithm allows to reduce the oscillation by maintaining the desired performance of the filter.

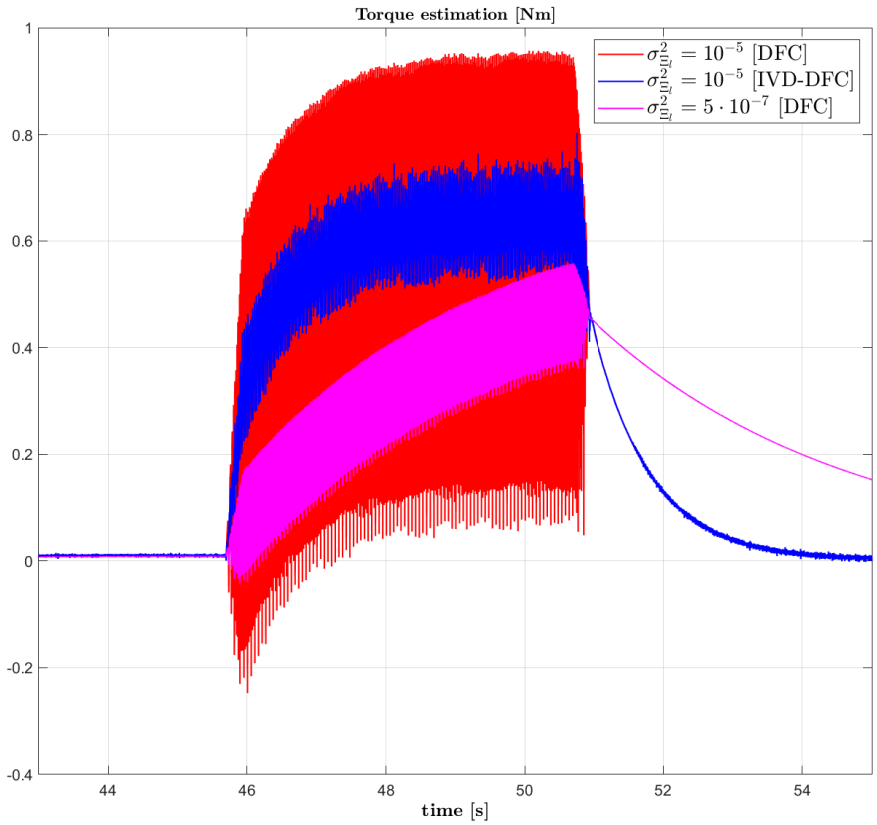

Figure 5.23: Torque estimation comparison between DFC and IVD-DFC technique. An external load torque is applied to the wheel by means of a brake.

5.3 Conclusions

The IVD-DFC algorithm has been tested using two different set-ups in order to analyze its performance. In particular, the iterative algorithm has been used in combination with a Kalman filter to estimate the system state, i.e. position, speed and external load torque of the motor. The results have been compared to the DFC technique and the EKF observation method, which requires the knowledge of both parameters a and b. As shown, the IVD-DFC and the EKF methods can suppress the deterioration due to the fourth harmonic generated by the DFC technique. The EKF incorporates the filtering process of the system state in one structure and the elimination of the fourth harmonic, whereas the IVD-DFC, which fulfills only the fourth harmonic elimination task, has to be combined to a Kalman filter in order to perform the system state estimation. Thus, the EKF seems to be a straightforward solution to those issues. However, the parameters a and b needed for the EKF algorithm cannot be estimated online, whereas the IVD-DFC can be combined with an RLS algorithm for the estimation of the parameter b. The point is that for most applications, the value of the parameters a and b is not given a priori. Hence, the IVD-DFC is the best choice for the purpose.

Conclusion and outlook

The DFC sensorless technique is a valid solution for state observation, drive and control of PMSMs that rely on inaccurate current measurements if any at all. Thanks to the star-point voltage measurements, the DFC signals have a large signal-to-noise ratio that represents an advantage for those systems that require high accuracy measurements, like small actuators. Nevertheless, the DFC signals are characterized by higher harmonics which may deteriorate the estimation process of the angular position and, consequently, the operations performed on the machine. Starting from this consideration, this work focused on analyzing the information deterioration introduced by the hiher order harmonics of the DFC signals and it proposed a novelty solution for the improvement of the angular position estimation, namely the IVD algorithm.

Firstly, the mathematical expression of the DFC signals has been derived considering a generic definition of the machine inductance matrix. From the obtained expression, the presence of two harmonics can be asserted, one with a frequency equal to the double of the electrical angular speed of the machine (second or fundamental harmonic) and one with frequency four times the angular speed (fourth harmonic). These harmonics have amplitudes a and b, respectively. As shown, the deterioration of the position estimation is determined by the parameter b, i.e. the amplitude of the fourth harmonic, which has to be zero in order to allow a perfect extraction of the position information. If the parameters a and b are known, the most straightforward way to estimate the angular position and, at the same time, to avoid the deterioration due to the fourth harmonic is to implement the DFC signal expression using an EKF (Extended Kalman Filter). The EKF is not affected by the deterioration due to the fourth harmonic and, at the same time, it performs the state estimation of the machine. This solution has been considered in the experimental validation as a reference technique. However, the knowledge of the parameters a and b is typically not available or difficult to identify.

Instead, the IVD algorithm can improve the DFC position estimation by means of a static recursive calculation of the angular position, which needs only the knowledge of the parameter b. That adds a practical advantage to the implementation of the IVD algorithm. In fact, the parameter can be easily identified by combining the IVD-DFC technique with an RLS-like estimation algorithm. This solution is an easier solution for implementation than the EKF. Moreover, instead of other classical solutions for eliminating the fourth harmonic, the IVD is a static algorithm. Hence, it is not based on a dynamical system that has to be tuned to some optimum criteria.

Nevertheless, the IVD-DFC method is not able to perform the state estimation of the machine itself. In order to allow the observation of the machine state, a Kalman filter has been combined with the IVD-DFC technique. Thus, the overall system is composed of three parts: the IVD-DFC technique, the RLS algorithm and the Kalman filter. It has been shown that the computational effort taken by this combination can exceed the one taken by the EKF method for a large number of iterations performed by the IVD algorithm. However, if

the iteration number is small enough, the IVD-DFC based observation results to be the most efficient method.

The presented experimental results confirm what was predicted by the theory. Two different set-ups have been considered to provide a solid comparison and confirm the repeatability of the tests. The motors have been chosen with different characteristics, but the application of the IVD algorithm provided an improvement in the estimated state and control for both machines.

Eventually, the methods have been used to estimate the external load torque applied at the motor shaft. That is particularly interesting for the e-bike application since the estimated load torque can be used to estimate the pedalling torque applied by the user. Also in this case, the IVD-DFC provided convincing results.

Undoubtedly, the IVD is a simple and interesting algorithm that can be further analyzed and optimized. The following subsection will cover the possible future development topics of that method.

Outlook

The iterative algorithm has opened new possibilities for further research on the topic of sensorless control. Among them we can identify three main topics to be further researched:

- The convergence of the IVD-DFC and RLS combination to the real position has been experimentally proven but a theoretical analysis has not been provided yet.
- The iterative algorithm should be extended in case the absolute value of the ratio between the parameters b and a, i.e. p, is greater than 0.5.
- The application of the IVD to other sensorless techniques is theoretically possible but must be confirmed by experiments.

Those points represent the future topics for a further improvement and generalization of the IVD method. Moreover, the possible combination of this algorithm to additional observation structure is not limited to the Kalman filters or RLS methods. An interesting aspect to be considered is the combination of the IVD to robust observers based on a sliding mode or invariant manifold approach to test its robustness against the motor parameter variations or even to increase the convergence speed of the estimation. Additionally, it would be possible to implement a unique algorithm comprehensive of IVD, state observation and online parameter estimation if a nonlinear observer approach is considered. Eventually, the advantages given by the estimation of the external load torque by means of a sensorless technique stimulates the research to investigate about high-robustness control to load torque disturbances as well as sensorless pedaling force estimation for e-bike, teeth surface identification for high-speed dental drills and other load torque based applications.

Bibliography

[1] Jacek F. Gieras. *Permanent Magnet Motor Technology: Design and Applications, Third Edition*. CRC Press, August 2009. Google-Books-ID: rFrFLUTri0MC.

[2] Oleg Jefimenko. *Electrostatic Motors: Their History, Types, and Principles of Operation*. Integrity Research Institiute, May 2011. Google-Books-ID: dbIhygAACAAJ.

[3] B. Bowers. Die Frühgeschichte des Elektromotors. *Philips Technische Rundschau*, 4(35. Jahrgang):35–104, 1975.

[4] Jill Jonnes. *Empires Of Light: Edison, Tesla, Westinghouse, And The Race To Electrify The World*. Random House, 2004. Google-Books-ID: BKX5UYWzVyQC.

[5] Dianguo Xu, Bo Wang, Guoqiang Zhang, Gaolin Wang, and Yong Yu. A review of sensorless control methods for AC motor drives. *CES Transactions on Electrical Machines and Systems*, 2(1):104–115, March 2018. Conference Name: CES Transactions on Electrical Machines and Systems.

[6] O. Benjak and D. Gerling. Review of position estimation methods for IPMSM drives without a position sensor part I: Nonadaptive methods. In *The XIX International Conference on Electrical Machines - ICEM 2010*, pages 1–6, September 2010.

[7] O. Benjak and D. Gerling. Review of position estimation methods for IPMSM drives without a position sensor part II: Adaptive methods. In *The XIX International Conference on Electrical Machines - ICEM 2010*, pages 1–6, September 2010.

[8] M. Schrödel. Detection of the rotor position of a permanent magnet synchronous machine at standstill. *ICEM, 1988*, pages 195–197, 1988.

[9] M. Schrödel. Sensorless control of A.C. machines. *VDI-Verlag*, 21, 1992.

[10] A. Zentai and T. Daboczi. Improving INFORM calculation method on permanent magnet synchronous machines. In *2007 IEEE Instrumentation Measurement Technology Conference IMTC 2007*, pages 1–6, May 2007. ISSN: 1091-5281.

[11] Manfred Schrodl, Matthias Hofer, and Wolfgang Staffler. Sensorless Control of PM Synchronous Motors in the Whole Speed Range Including Standstill Using a Combined INFORM/EMF Model. In *2006 12th International Power Electronics and Motion Control Conference*, pages 1943–1949, August 2006.

[12] Manfred Schrodl and Christian Simetzberger. Sensorless control of PM synchronous motors using a predictive current controller with integrated INFORM and EMF evaluation. In *2008 13th International Power Electronics and Motion Control Conference*, pages 2275–2282, September 2008.

[13] P.L. Jansen and R.D. Lorenz. Transducerless position and velocity estimation in induction and salient AC machines. *IEEE Transactions on Industry Applications*, 31(2):240–247, March 1995. Conference Name: IEEE Transactions on Industry Applications.

[14] P.L. Jansen and R.D. Lorenz. Transducerless field orientation concepts employing saturation-induced saliencies in induction machines. *IEEE Transactions on Industry Applications*, 32(6):1380–1393, November 1996. Conference Name: IEEE Transactions on Industry Applications.

[15] M.J. Corley and R.D. Lorenz. Rotor position and velocity estimation for a salient-pole permanent magnet synchronous machine at standstill and high speeds. *IEEE Transactions on Industry Applications*, 34(4):784–789, July 1998. Conference Name: IEEE Transactions on Industry Applications.

[16] M. Linke, R. Kennel, and J. Holtz. Sensorless position control of permanent magnet synchronous machines without limitation at zero speed. In *IEEE 2002 28th Annual Conference of the Industrial Electronics Society. IECON 02*, volume 1, pages 674–679 vol.1, November 2002.

[17] M. Linke, R. Kennel, and J. Holtz. Sensorless speed and position control of synchronous machines using alternating carrier injection. In *IEEE International Electric Machines and Drives Conference, 2003. IEMDC'03.*, volume 2, pages 1211–1217 vol.2, June 2003.

[18] P. Nussbaumer and Th. M. Wolbank. Using oversampling techniques to extract ac machine saliency information. In *IECON 2010 - 36th Annual Conference on IEEE Industrial Electronics Society*, pages 1035–1040, November 2010. ISSN: 1553-572X.

[19] Bastian Weber, Karsten Wiedmann, and Axel Mertens. Increased signal-to-noise ratio of sensorless control using current oversampling. In *2015 9th International Conference on Power Electronics and ECCE Asia (ICPE-ECCE Asia)*, pages 1129–1134, June 2015. ISSN: 2150-6086.

[20] Peter Landsmann. Sensorless Control of Synchronous Machines by Linear Approximation of Oversampled Current. page 185.

[21] Young-Doo Yoon, Seung-Ki Sul, Shinya Morimoto, and Kozo Ide. High-Bandwidth Sensorless Algorithm for AC Machines Based on Square-Wave-Type Voltage Injection. *IEEE Transactions on Industry Applications*, 47(3):1361–1370, May 2011. Conference Name: IEEE Transactions on Industry Applications.

[22] P. L. Xu and Z. Q. Zhu. Novel Carrier Signal Injection Method Using Zero-Sequence Voltage for Sensorless Control of PMSM Drives. *IEEE Transactions on Industrial Electronics*, 63(4):2053–2061, April 2016. Conference Name: IEEE Transactions on Industrial Electronics.

[23] C.S. Staines, C. Caruana, G.M. Asher, and M. Sumner. Sensorless control of induction Machines at zero and low frequency using zero sequence currents. *IEEE Transactions on Industrial Electronics*, 53(1):195–206, February 2006. Conference Name: IEEE Transactions on Industrial Electronics.

[24] Gao Qiang, G M Asher, M Sumner, and P Makys. Position Estimation of AC Machines at all Frequencies using only Space Vector PWM based Excitation. In *2006 3rd IET International Conference on Power Electronics, Machines and Drives - PEMD 2006*, pages 61–70, April 2006.

[25] Reiko Raute, Cedric Caruana, Joseph Cilia, Cyril Spiteri Staines, and Mark Summer. A zero speed operation sensorless PMSM drive without additional test signal injection. In *2007 European Conference on Power Electronics and Applications*, pages 1–10, September 2007.

[26] Dirk Paulus, Peter Landsmann, and Ralph Kennel. Sensorless field- oriented control for permanent magnet synchronous machines with an arbitrary injection scheme and direct angle calculation. In *2011 Symposium on Sensorless Control for Electrical Drives*, pages 41–46, September 2011. ISSN: 2166-6733.

[27] Dirk Paulus, Peter Landsmann, Sascha Kuehl, and Ralph Kennel. Arbitrary injection for permanent magnet synchronous machines with multiple saliencies. In *2013 IEEE Energy Conversion Congress and Exposition*, pages 511–517, September 2013. ISSN: 2329-3748.

[28] A. Consoli, G. Scarcella, and A. Testa. A new zero frequency flux position detection approach for direct field oriented control drives. In *Conference Record of the 1999 IEEE Industry Applications Conference. Thirty-Forth IAS Annual Meeting (Cat. No.99CH36370)*, volume 4, pages 2290–2297 vol.4, October 1999. ISSN: 0197-2618.

[29] J. Holtz and Hangwen Pan. Acquisition of rotor anisotropy signals in sensorless position control systems. In *38th IAS Annual Meeting on Conference Record of the Industry Applications Conference, 2003.*, volume 2, pages 1165–1172 vol.2, October 2003.

[30] J. Holtz and Hangwen Pan. Elimination of saturation effects in sensorless position-controlled induction motors. *IEEE Transactions on Industry Applications*, 40(2):623–631, March 2004. Conference Name: IEEE Transactions on Industry Applications.

[31] J. Holtz. Sensorless Control of Induction Machines—With or Without Signal Injection? *IEEE Transactions on Industrial Electronics*, 53(1):7–30, February 2006. Conference Name: IEEE Transactions on Industrial Electronics.

[32] Yoshitaka Iwaji, Yasuhiko Kokami, and Minoru Kurosawa. Position-sensorless control method at low speed for permanent magnet synchronous motors using induced voltage caused by magnetic saturation. In *The 2010 International Power Electronics Conference - ECCE ASIA -*, pages 2238–2243, June 2010.

[33] A. Consoli, G. Scarcella, G. Tutino, and A. Testa. Zero frequency rotor position detection for synchronous PM motors. In *2000 IEEE 31st Annual Power Electronics Specialists Conference. Conference Proceedings (Cat. No.00CH37018)*, volume 2, pages 879–884 vol.2, June 2000. ISSN: 0275-9306.

[34] R. Strothmann. “fremderregte elektrische maschine”. european pat. 1005716b1. rolf strothmann. nov. 14, 2001.

[35] P. Thiemann, C. Mantala, T. Mueller, R. Strothmann, and E. Zhou. Direct Flux Control (DFC): A New Sensorless Control Method for PMSM. In *2011 46th International Universities' Power Engineering Conference (UPEC)*, pages 1–6, September 2011.

[36] Chawanakorn Mantala. *Sensorless Control of Brushless Permanent Magnet Motors*. PhD thesis, South Westphalia University of Applied Sciences, December 2013.

[37] Gianvito Gallicchio, Marco Palmieri, Emanuele Grasso, Matthias Nienhaus, and Francesco Cupertino. Inductances Computation Using Finite Element Analysis for PMSM Sensorless Control. In *2020 IEEE International Conference on Power Electronics, Drives and Energy Systems (PEDES)*, pages 1–6, December 2020.

[38] Stephan Kleen and Matthias Nienhaus. Simulation and analysis of the winding inductances of small electrical motors for a sensorless control method. In *IKMT 2015; 10. ETG/GMM-Symposium Innovative small Drives and Micro-Motor Systems*, pages 1–5, September 2015.

[39] Stephan Kleen and Matthias Nienhaus. Impact of the embedding of magnets on a sensorless drive method. In *Innovative Small Drives and Micro-Motor Systems; 11th GMM/ETG-Symposium*, pages 1–5, September 2017.

[40] E. Grasso, D. Merl, and M. Nienhaus. A novel online phase inductance measurement technique for sensorless control applications. *Messe Bremen, ACTUATOR*, 2014.

[41] E. Grasso, E. Kanapari, and M. Nienhaus. Analysis of Direct Flux Observation for field oriented control PMSM. In *IKMT 2015; 10. ETG/GMM-Symposium Innovative small Drives and Micro-Motor Systems*, pages 1–6, September 2015.

[42] Riccardo Mandriota, Marco Palmieri, Matthias Nienhaus, Francesco Cupertino, and Emanuele Grasso. Application of Star-Point Voltage Exploiting Sensorless Techniques to Low-Power PMSMs. In *2020 IEEE 29th International Symposium on Industrial Electronics (ISIE)*, pages 1529–1534, June 2020. ISSN: 2163-5145.

[43] Emanuele Grasso, Daniel Merl, and Matthias Nienhaus. Verfahren und vorrichtung zum bestimmen einer läuferlage eines läufers einer elektronisch kommutierten elektrischen maschine, March 2018.

[44] Daniel Merl, Emanuele Grasso, Robert Schwartz, and Matthias Nienhaus. A Direct Flux Observer Based on a Fast Resettable Integrator Circuitry for Sensorless Control of PMSMs. *ACTUATOR 2018 - 16th International Conference on New Actuators*, pages 1–4, June 2018.

[45] Emanuele Grasso and Matthias Nienhaus. A Direct Flux Observer for Robust to Noise Sensorless Control of PMSMs. *Messe Bremen, ACTUATOR*, 2016.

[46] Stefano Fabbri, Sabino Catalano, Marco Palmieri, Francesco Cupertino, Matthias Nienhaus, and Emanuele Grasso. Full speed range sensor less control for PMSM using an adaptive extended Kalman filter. In *2020 AEIT International Annual Conference (AEIT)*, pages 1–6, September 2020.

[47] Niklas König, Emanuele Grasso, Klaus Schuhmacher, and Matthias Nienhaus. Parameter identification of star-connected PMSMs by means of a sensorless technique. In *2018 Thirteenth International Conference on Ecological Vehicles and Renewable Energies (EVER)*, pages 1–7, April 2018.

[48] Stefano Fabbri, Davide D'Amato, Marco Palmieri, Francesco Cupertino, Matthias Nienhaus, and Emanuele Grasso. Performance Comparison of Different Estimation Techniques of the External Load-torque applied on a PMSM using Direct Flux Control. In *2020 International Symposium on Power Electronics, Electrical Drives, Automation and Motion (SPEEDAM)*, pages 688–693, June 2020.

[49] Emanuele Grasso. *Direct Flux Control – A sensorless technique for star-connected synchronous machines: An analytic approach (Berichte aus der Steuerungs- und Regelungstechnik)*. Shaker, December 2021.

[50] J.W. Umland and M. Safiuddin. Magnitude and symmetric optimum criterion for the design of linear control systems: what is it and how does it compare with the others? *IEEE Transactions on Industry Applications*, 26(3):489–497, May 1990. Conference Name: IEEE Transactions on Industry Applications.

[51] B. Zigmund and Angela A. Terlizzi. Experimental Evaluation of PI Tuning Techniques for Field Oriented Control of Permanent Magnet Synchronous Motors. *Advances in Electrical and Electronic Engineering*, 5:114–119, 2011.

[52] Emanuele Grasso, Marco Palmieri, Riccardo Mandriota, Francesco Cupertino, Matthias Nienhaus, and Stephan Kleen. Analysis and Application of the Direct Flux Control Sensorless Technique to Low-Power PMSMs. *Energies*, 13(6):1453, January 2020. Number: 6 Publisher: Multidisciplinary Digital Publishing Institute.

[53] Klaus Schuhmacher, Emanuele Grasso, and Matthias Nienhaus. Improved rotor position determination for a sensorless star-connected PMSM drive using Direct Flux Control. *The Journal of Engineering*, 2019(17):3749–3753, 2019. _eprint: https://ietresearch.onlinelibrary.wiley.com/doi/pdf/10.1049/joe.2018.8055.

[54] Stefano Fabbri, Klaus Schuhmacher, Matthias Nienhaus, and Emanuele Grasso. Improvement of Position Estimation of PMSMs Using an Iterative Vector Decoupling Algorithm. *Energies*, 14(1):245, January 2021. Number: 1 Publisher: Multidisciplinary Digital Publishing Institute.

[55] M.W. Degner and R.D. Lorenz. Using multiple saliencies for the estimation of flux, position, and velocity in AC machines. In *IAS '97. Conference Record of the 1997 IEEE Industry Applications Conference Thirty-Second IAS Annual Meeting*, volume 1, pages 760–767 vol.1, October 1997. ISSN: 0197-2618.

[56] Emanuele Grasso, Marco Palmieri, Riccardo Mandriota, Gianvito Gallicchio, Francesco Cupertino, and Matthias Nienhaus. Influence and compensation of the stator flux on the direct flux control sensorless technique for PMSMs. *The Journal of Engineering*, n/a(n/a). _eprint: https://ietresearch.onlinelibrary.wiley.com/doi/pdf/10.1049/tje2.12039.

[57] Daniel Simon. Optimal State Estimation: Kalman, H, and Nonlinear Approaches. January 2006.

List of Figures

List of Tables